KADIR HAS UNIVERSITY
SCHOOL OF GRADUATE STUDIES
PROGRAM OF COMPUTATIONAL SCIENCES AND ENGINEERING

SCALE AND COMPLEXITY: RENORMALIZATION-GROUP THEORY OF PHASE TRANSITIONS, SPIN-GLASS CHAOS, AND EMERGENT ORDER IN COMPLEX SPIN SYSTEMS

GÜNEŞ ERBİL CAN ARTUN

DOCTOR OF PHILOSOPHY THESIS

ISTANBUL, FEBRUARY, 2026

SCALE AND COMPLEXITY: RENORMALIZATION-GROUP THEORY OF PHASE TRANSITIONS, SPIN-GLASS CHAOS, AND EMERGENT ORDER IN COMPLEX SPIN SYSTEMS

GÜNEŞ ERBİL CAN ARTUN
ADVISOR: PROF. DR. AHMET NİHAT BERKER

A thesis submitted to
the School of Graduate Studies of Kadir Has University
in partial fulfillment of the requirements for the degree of
Doctor of Philosophy in
Computational Sciences and Engineering
(Department of Engineering and Natural Sciences)

Istanbul, February, 2026

APPROVAL

This thesis titled SCALE AND COMPLEXITY: RENORMALIZATION-GROUP THEORY OF PHASE TRANSITIONS, SPIN-GLASS CHAOS, AND EMERGENT ORDER IN COMPLEX SPIN SYSTEMS submitted by GÜNEŞ ERBİL CAN ARTUN, in partial fulfillment of the requirements for the degree of Doctor of Philosophy in Computational Sciences and Engineering is approved by

Prof. Dr. Ahmet Nihat Berker (Advisor)
MEF University _____

Assoc. Prof. Alkan Kabakçıoğlu
Koç University _____

Assoc. Prof. Deniz Eroğlu
Kadir Has University _____

Assoc. Prof. Ozan Sabahattin Sarıyer
Piri Reis University _____

Asst. Prof. Arash Mohammadian Rezaeinazhad
Kadir Has University _____

I confirm that the signatures above belong to the aforementioned faculty members.

_____

Director of the School of Graduate Studies
Date of Approval: 24.02.2026

DECLARATION ON RESEARCH ETHICS AND PUBLISHING METHODS

I, GÜNEŞ ERBİL CAN ARTUN, hereby declare

- that this Ph.D. Thesis that I have submitted is entirely my own work and I have cited and referenced all material and results that are not my own in accordance with the rules;

- that this Ph.D. Thesis does not contain any material from any research submitted or accepted to obtain a degree or diploma at another educational institution;

- and that I commit and undertake to follow the "Kadir Has University Academic Codes of Conduct" prepared in accordance with the "Higher Education Council Codes of Conduct".

In addition, I acknowledge that any claim of irregularity that may arise in relation to this work will result in a disciplinary action in accordance with the university legislation.

Güneş Erbil Can Artun

24.02.2026

To the many we may never know by name — whether they toiled in silence or fell in battle — who devoted their lives to their homeland and the ideals they believed in.

ACKNOWLEDGMENT

The encounter with my advisor Nihat Berker constitutes a turning point in my life — one that continues to shape it. What I have learned from him extends far beyond science; he has taught me, as a human being, an extraordinary range of lessons on an extraordinary range of subjects. Since no word of adequate strength has yet been coined for what I feel, I will meet my gratitude with the only vessel available and simply say: thank you.

I would like to thank Deniz Eroğlu, from whom I took courses and learned things that directly contributed to my doctoral work, but who also opened the doors of both his heart and his research group to me well beyond the scope of that work. He stood by me at all times and never hesitated to support me on the most diverse of matters. I thank him for being, at once, a mentor, an elder brother, and a friend.

I am grateful to Alkan Kabakçıoğlu, a wonderful person who, as a member of my thesis monitoring committee, continued to teach me something new at every meeting, at my defense, and in every conversation in between, through the depth of his insight, feedback, and questions.

I thank Ozan Sarıyer, a valued member of my jury, who gave selflessly of his time and expertise, catching critical details that no one else had noticed and significantly improving the thesis I put my name to. Whatever imperfections remain are mine alone.

I would like to thank Arash Rezaeinazhad — both my teacher and my friend — whose originality was such that even in the very first lecture of his teaching career he offered solutions I resolved to adapt to my own. With his kind heart and gracious manner, he will always hold a special place in my life.

I send my love and my thanks to my talented and brilliant friends and colleagues Alpar Türkoğlu, Deniz Sarman, İbrahim Keçoğlu, and Yiğit Pektaş, with whom I had the opportunity to collaborate and co-author papers during my doctoral studies.

I am grateful to Çağlar Aslan, a distinguished scientist at the TÜBİTAK National Metrology Institute and a dear friend of mine, for his sincere friendship under all circumstances and for drawing on his strong experimntal expertise to discuss and devise ways of testing my theoretical predictions.

I owe a debt of gratitude to my parents — my mother, Gönül Artun, and my father, Abdi Artun — who, behind the scenes, thought of me more than I thought of myself, who never withheld their tangible support before or during my doctorate, and whose very existence has been the greatest support of all. In truth, it is my entire life for which I should be thanking them. I also thank my brother, Cüneyt Artun, who, when I was still young, channeled my appetite for research, learning, and discovery into concrete life plans. That I went to Harvard years ago to carry out my first research, and that I have now completed a doctorate, are both direct consequences of his influence. I look forward, with curiosity, to seeing at which future crossroads of my life his mark will appear next.

I would like to thank my uncle Attila Artun — Minkör, as we knew him — who was by my side from the day I was born and was like a second elder brother to me. Though he departed this world not long ago, while I was still pursuing my doctorate, I write these words in the hope that he may still read them from wherever he may be. I thank him for his presence, which shaped my thoughts and who I am; for perhaps being the person in my life who understood me best; for his deep devotion to knowledge and faith; and for the counsel with which he guided and emboldened me in the struggles of life.

Last but by no means least, I wish to thank the woman of my life, Ecem Sezen. Throughout my doctoral journey she stood by me with an unwavering resolve that did not change in my most stressful moments any more than in my happiest. She supported me, under every condition, with the kind of unconditional devotion that only a mother could show a child. Despite the nights and days, the months and years in which I neglected her, she never showed the faintest sign of giving up on bearing with me. For all of this, I thank her.

SCALE AND COMPLEXITY: RENORMALIZATION-GROUP THEORY OF PHASE TRANSITIONS, SPIN-GLASS CHAOS, AND EMERGENT ORDER IN COMPLEX SPIN SYSTEMS

ABSTRACT

Simple local interactions among discrete degrees of freedom can, upon coarse-graining, give rise to rich collective phenomena including phase transitions, spontaneous symmetry breaking, and chaos. This thesis explores how such macroscopic complexity emerges from microscopic simplicity through systematic renormalization-group analysis of statistical mechanical spin systems. Position-space renormalization-group theory, implemented via the Migdal–Kadanoff approximation—exact on hierarchical lattices—is applied to a broad class of models in spatial dimensions $d = 1$, 2, and 3. Complete density calculations of q-state Potts and clock models reveal interface-density reentrance under symmetry breaking. Universal spin-glass chaos is established for the spin-s Ising model, where the Lyapunov exponent $\lambda = 1.93$ and runaway exponent $y_R = 0.24$ are shown to be independent of spin magnitude from $s = 1/2$ to $s \to \infty$. A nematic phase—liquid-crystal order in a dirty magnet—emerges in n-component cubic-spin spin glasses for $n \geq 3$, and the application of magnetic fields yields 17 distinct phases with novel spin-glass topologies. Spin-glass sponges with fractal surfaces are found to support independent surface chaos characterized by distinct Lyapunov exponents. Merging Potts and clock interactions produces five ordered phases with rich multicritical structure, where even-q and odd-q systems exhibit qualitatively different topologies including algebraic order arising from ground-state degeneracy. The XY Ashkin–Teller model in $d = 2$ reveals four algebraically ordered phases, each subtended by fixed lines of potential surfaces with continuously varying critical exponents. Long-range power-law interactions Jr^{-a} are shown to enable ferromagnetic order in $d = 1$, generate piecewise chaotic spin-glass interactions, and produce giant reentrance in the Blume–Capel model through competition between magnetic ordering and vacancy proliferation. The methodology is further extended to metastable Potts droplets and hysteresis loops across first-order transitions. Throughout, the topology of renormalization-group flows—fixed points, fixed lines, and chaotic attractors—provides a quantitative and mechanistic account of how scale transformation generates complexity.

Keywords: Renormalization Group, Phase Transitions, Spin Glasses, Chaos, Hierarchical Lattices, Universality, Critical Phenomena, Complexity, Frustration, Emergence

ÖLÇEK VE KARMAŞIKLIK: KARMAŞIK SPİN SİSTEMLERİNDE FAZ GEÇİŞLERİ, SPİN-CAMI KAOSU VE BELİREN DÜZENİN RENORMALİZASYON GRUBU KURAMI

ÖZET

Ayrık serbestlik dereceleri arasındaki basit yerel etkileşimler, ölçek dönüşümü altında faz geçişleri, kendiliğinden simetri kırılması ve kaos gibi zengin kolektif olgulara yol açabilir. Bu tez, bu tür makroskobik karmaşıklığın mikroskobik basitlikten nasıl ortaya çıktığını, istatistiksel mekanik spin sistemlerinin sistematik renormalizasyon grubu analizi aracılığıyla incelemektedir. Hiyerarşik örgülerde tam olan Migdal–Kadanoff yaklaşımıyla uygulanan konum-uzayı renormalizasyon grubu teorisi, $d = 1$, 2 ve 3 uzaysal boyutlarında geniş bir model sınıfına uygulanmıştır. q-durumlu Potts ve saat modellerinin tam yoğunluk hesaplamaları, simetri kırılması altında arayüzey yoğunluğu yeniden girişini ortaya koymaktadır. Spin-s Ising modeli için evrensel spin-camı kaosu kurulmuş olup Lyapunov üsteli $\lambda = 1{,}93$ ve kaçış üsteli $y_R = 0{,}24$'ün $s = 1/2$'den $s \to \infty$'a kadar spin büyüklüğünden bağımsız olduğu gösterilmiştir. n-bileşenli kübik-spin spin camlarında $n \geq 3$ için bir nematik faz—kirli bir mıknatısta sıvı kristal düzeni—ortaya çıkmakta ve manyetik alan uygulaması 17 farklı faz ile yeni spin-camı topolojileri vermektedir. Fraktal yüzeylere sahip spin-camı süngerlerin, farklı Lyapunov üstelleriyle karakterize edilen bağımsız yüzey kaosunu desteklediği bulunmuştur. Potts ve saat etkileşimlerinin birleştirilmesi, zengin çokkritik yapıya sahip beş düzenli faz üretmekte; çift-q ve tek-q sistemleri, taban durumu dejenerasyonundan kaynaklanan cebirsel düzen dahil niteliksel olarak farklı topolojiler sergilemektedir. $d = 2$'de XY Ashkin–Teller modeli, sürekli değişen kritik üstellere sahip potansiyel yüzeylerinin sabit çizgileriyle tanımlanan dört cebirsel düzenli faz ortaya çıkarmaktadır. Uzun menzilli kuvvet-yasası etkileşimleri Jr^{-a}, $d = 1$'de ferromanyetik düzeni mümkün kılmakta, parçalı kaotik spin-camı etkileşimleri üretmekte ve Blume–Capel modelinde manyetik düzenlenme ile boşluk çoğalması arasındaki rekabet yoluyla dev yeniden giriş oluşturmaktadır. Yöntem ayrıca kararsız Potts damlacıklarına ve birinci derece geçişlerdeki histerezis döngülerine genişletilmiştir. Çalışma boyunca, renormalizasyon grubu akışlarının topolojisi—sabit noktalar, sabit çizgiler ve kaotik çekiciler—ölçek dönüşümünün karmaşıklığı nasıl ürettiğine dair nicel ve mekanistik bir açıklama sunmaktadır.

Anahtar Sözcükler: Renormalizasyon Grubu, Faz Geçişleri, Spin Camları, Kaos, Hiyerarşik Örgüler, Evrensellik, Kritik Olaylar, Karmaşıklık, Bunalım, Ortaya Çıkış

TABLE OF CONTENTS

ACKNOWLEDGMENT ..... **v**
ABSTRACT ..... **vii**
ÖZET ..... **viii**
LIST OF FIGURES ..... **xvi**
LIST OF TABLES ..... **xviii**
LIST OF SYMBOLS ..... **xix**
LIST OF ACRONYMS AND ABBREVIATIONS ..... **xxi**
1 INTRODUCTION: THE ANATOMY OF COMPLEXITY **1**
1.1 The Fundamental Mystery **1**
1.2 Complexity as Scale-Dependent Emergence **1**
1.3 Historical Development **3**
1.3.1 From Boltzmann to Onsager **3**
1.3.2 The renormalization group revolution **4**
1.3.3 Beyond critical exponents: phase structure and chaos **5**
1.4 The Renormalization Group as Mechanism **6**
1.4.1 What coarse-graining preserves and destroys **6**
1.4.2 Position-space methods and hierarchical lattices **7**
1.4.3 Transfer matrices and partition function conservation **7**
1.5 Organizing Principles: Generators and Modulators of Complexity **9**
1.5.1 Three complexity generators **9**
1.5.2 Three complexity modulators **10**
1.5.3 Scope and limitations of the framework **10**
1.6 Thesis Overview and Principal Contributions **11**
2 THERMODYNAMIC FOUNDATIONS **13**
2.1 Introduction **13**
2.2 Model Definitions **14**
2.2.1 The q-state Potts model **14**
2.2.2 The q-state clock model **14**
2.2.3 Symmetry distinctions **14**
2.3 Renormalization-Group Formulation **15**
2.3.1 Transfer matrix construction **15**

2.3.2 Bond moving and decimation 16
2.3.3 Density recursion relations 16
2.4 Results for Potts Models 17
2.4.1 Recursion relations 17
2.4.2 Densities and interface density reentrance 20
2.5 Results for Clock Models 22
2.5.1 Renormalization-group calculation and six-energy flows for $q = 4$ 23
2.5.2 Renormalization-group flows of 8, 12, 15, and 20 energies for $q = 5, 6, 7, 8$ 24
2.5.3 Comparison with Potts results 25
2.6 Magnetizations and Infinite-q Limit 25
2.7 Conclusion 29
3 UNIVERSAL SPIN-GLASS CHAOS 31
3.1 Introduction 31
3.1.1 Generalized Ising system and frustration 31
3.1.2 Chaos under scale transformation 31
3.1.3 The question of universality 32
3.2 Model 33
3.3 Renormalization-Group Method 33
3.3.1 Transfer matrix for general spin 33
3.3.2 Quenched disorder and distribution flows 34
3.3.3 Phase identification from asymptotic flows 35
3.4 Phase Diagrams and Critical Temperatures 36
3.4.1 Global phase structure 36
3.4.2 Critical temperatures as functions of spin magnitude 37
3.4.3 Percolative nature of phase boundaries 38
3.5 Spin-Glass Chaos 38
3.5.1 Lyapunov exponents 38
3.5.2 Runaway exponents and unsaturated order 40
3.6 Conclusion 41
4 EMERGENT NEMATIC PHASE 42
4.1 Introduction 42
4.1.1 Vector spins and frustration 42
4.1.2 Cubic spins as discretized Heisenberg spins 42
4.2 Model and Method 43
4.3 Phase Diagrams 45

4.3.1 Results for $n = 1, 2, 3$ components 45
4.3.2 The emergence of the nematic phase 45
4.3.3 Persistence for $n \geq 3$ 46
4.4 Renormalization-Group Sinks of the Phases 47
4.4.1 Ordered phase sinks 47
4.4.2 The nematic sink structure 48
4.4.3 Spin-glass fixed distribution 48
4.5 Spin-Glass Chaos 49
4.5.1 Lyapunov exponents and odd-even oscillations 49
4.5.2 Comparison with Ising spin glasses 51
4.6 Physical Interpretation: Liquid Crystal Order in Dirty Magnets 51
4.7 Conclusion 52
5 PHASE PROLIFERATION UNDER MAGNETIC FIELDS 53
5.1 Introduction 53
5.1.1 Fields as symmetry probes 53
5.1.2 Types of magnetic fields for n-component spins 53
5.2 Model and Method 53
5.2.1 Hamiltonian with magnetic field 53
5.2.2 Transfer matrix formulation 54
5.2.3 Renormalization-group procedure 55
5.3 Zero-Field Baseline 56
5.4 Fields on Ferromagnetic Systems 56
5.5 Fields on Antiferromagnetic Systems 58
5.6 Spin-Glass Systems Under Field 60
5.6.1 Phase diagrams and novel topologies 60
5.6.2 Field-induced spin-glass phase 60
5.6.3 Asymmetric competition and chaotic variables 61
5.7 Spin-Glass Chaos Characterization 62
5.8 Classification of All Seventeen Phases 63
5.9 Discussion and Conclusion 63
6 SURFACE CHAOS IN SPIN-GLASS SPONGES 67
6.1 Introduction 67
6.1.1 Surfaces and boundaries in statistical mechanics 67
6.1.2 Dimensional thresholds for spin-glass order 67
6.2 Model: The Spin-Glass Sponge 68
6.2.1 Bulk and surface interactions 68
6.2.2 Surface dimensionality and sponge geometry 68

6.3 Renormalization-Group Method for Surfaced Systems 69
6.3.1 Double-graph hierarchical construction 69
6.3.2 Coupled distribution flows 70
6.4 Phase Diagrams 71
6.4.1 Surface-only spin-glass phase 71
6.4.2 The special multicritical point 73
6.5 Three Types of Chaos 73
6.6 Physical Interpretation: Intrinsic Versus Driven Complexity 76
6.7 Conclusion 77
7 SYMMETRY COMPETITION IN MERGED POTTS-CLOCK MODELS .. 79
7.1 Introduction 79
7.1.1 Potts Symmetry Versus Clock Symmetry 79
7.1.2 Incompatible ordering tendencies 80
7.2 Model 80
7.3 Method 81
7.3.1 Hierarchical lattice equivalence 81
7.3.2 Calibration to exact results 82
7.3.3 Transfer matrix formulation 82
7.3.4 Inclusion of effective vacancies 84
7.4 Results: Global Phase Diagrams 84
7.4.1 Overview of phase diagram structure 84
7.4.2 Renormalization-group sinks of the ordered phases 85
7.4.3 Even-q systems: conventional order 88
7.4.4 Odd-q systems: algebraic order from ground-state degeneracy 88
7.4.5 Multicritical points and phase boundary structure 89
7.4.6 Nature of the algebraically ordered phases 89
7.4.7 Limiting Cases: pure Potts and pure clock 89
7.5 Discussion: Symmetry Competition Generates Phase Complexity 90
7.5.1 Comparison with frustrated systems 90
7.5.2 The role of ground-state degeneracy 91
7.6 Conclusion 91
8 ALGEBRAIC PHASES IN THE XY-ASHKIN-TELLER MODEL 93
8.1 Introduction 93
8.1.1 Algebraic order and the absence of length scale 93
8.1.2 The Ashkin-Teller construction with continuous spins 94
8.2 Quasi-Disorder Lines 94
8.3 Renormalization-Group Method 95

8.3.1 Double Fourier representation 95
8.3.2 Numerical implementation 97
8.4 Phase Diagram and Fixed Lines 97
8.5 Fixed Lines of Potential Surfaces 99
8.5.1 Factorization at the fixed lines 99
8.5.2 Physical interpretation of the fixed-line sinks 101
8.5.3 Entropy and degeneracy structure 101
8.5.4 The disordered phase sink 103
8.6 Continuously Varying Critical Exponents 103
8.6.1 Single XY model fixed line 103
8.6.2 XY-Ashkin-Teller fixed surfaces 104
8.6.3 Variation along the fixed line 104
8.7 Discussion: The Richest Form of Scale Invariance 104
8.7.1 Generators and modulators in the XY-Ashkin-Teller model 105
8.7.2 Comparison with discrete-spin systems 105
8.7.3 The factorization phenomenon 106
8.7.4 Quasi-disorder lines and zero-temperature disorder 106
8.8 Conclusion 106
9 LONG-RANGE ISING MODEL 108
9.1 Introduction 108
9.1.1 Order in low dimensions 108
9.1.2 Power-law interactions and effective dimensionality 108
9.2 Renormalization-Group Method for Long-Range Interactions 109
9.2.1 Cell-spin construction 109
9.2.2 Partition function conservation 110
9.2.3 Two-cell cluster approximation 110
9.2.4 Tracking interactions at multiple distances 110
9.3 Ferromagnetic Results 111
9.3.1 Phase diagram 111
9.3.2 Critical exponents as functions of range 112
9.4 Antiferromagnetic Results: Pervasive Frustration 113
9.4.1 Absence of antiferromagnetic order 113
9.4.2 Contrast with short-range antiferromagnet 113
9.5 Spin-Glass Results 113
9.5.1 Phase diagram without antiferromagnetic order 113
9.5.2 Piecewise chaotic interaction functions 113
9.6 Discussion: Interaction Range as Control Parameter 115

9.7 Conclusion 115
10 LONG-RANGE BLUME–CAPEL MODEL 116
10.1 Introduction 116
10.1.1 The Blume-Capel model and tricritical behavior 116
10.1.2 Motivation for long-range extension 117
10.2 Renormalization-Group Method 117
10.2.1 Cell-spin assignment with vacancies 117
10.2.2 Recursion relations 118
10.2.3 Computational implementation 119
10.3 Results: Phase Diagrams 120
10.3.1 Range dependence of phase structure 120
10.3.2 Giant reentrance phenomenon 122
10.3.3 Physical mechanism 122
10.4 Results: Critical and Tricritical Temperatures 123
10.5 Discussion: Competition Between Ordering and Dilution 125
10.6 Conclusion 126
11 METASTABLE POTTS DROPLETS 127
11.1 Introduction: Nonequilibrium Properties from an Equilibrium Calculation 127
11.1.1 Metastability in physical systems 127
11.1.2 Finite-system renormalization group with fixed boundaries 128
11.2 Model and Method 129
11.2.1 The q-state Potts model in magnetic field 129
11.2.2 Renormalization-group formulation 129
11.2.3 Transfer-matrix implementation 130
11.2.4 Density recursion with fixed boundary conditions 130
11.2.5 Criterion for droplet existence 130
11.3 Results: Metastable Droplets 131
11.3.1 Magnetization versus droplet size 131
11.3.2 Critical droplet size versus number of states 133
11.3.3 Power-law scaling 133
11.4 Results: Hysteresis Loops 135
11.4.1 Method 135
11.4.2 Temperature dependence 135
11.4.3 Size dependence 136
11.4.4 Dependence on number of states 136
11.4.5 Asymmetry in hysteresis branches 138

11.5 Discussion: Extension to Metastable Criticality 138
11.5.1 Potential applications 138
11.5.2 Comparison with equilibrium results 139
11.5.3 Limitations and future directions 139
11.6 Conclusion 139
12 CONCLUSION: SYNTHESIS AND PERSPECTIVE 140
12.1 Summary of Methods and Results 140
12.1.1 The renormalization group as unifying method 140
12.1.2 Principal results by chapter 141
12.1.3 Quantitative achievements 142
12.2 Physical Interpretation of Key Findings 143
12.2.1 The meaning of universal chaos 143
12.2.2 Why nematic order requires $n \geq 3$ 143
12.2.3 Giant reentrance as competing instabilities 144
12.2.4 Fixed lines and the nature of algebraic order 144
12.3 Complexity and Scale: What Has Been Learned 145
12.3.1 Emergence through coarse-graining 145
12.3.2 The topology of flows as organizing principle 146
12.3.3 Limitations and open questions 146
12.4 The Future of Renormalization-Group Studies 147
12.4.1 Methodological frontiers 147
12.4.2 Connections to quantum many-body physics 147
12.4.3 Complex systems beyond spin models 148
12.4.4 Computational and machine learning approaches 148
12.5 Concluding Remarks 149
BIBLIOGRAPHY 151
CURRICULUM VITAE 163

LIST OF FIGURES

2.1 Migdal-Kadanoff transformation and hierarchical lattice for $d = 3$, $b = 2$ .. 15
2.2 Critical temperatures of Potts and clock models vs q 18
2.3 Nearest-neighbor densities of q-state Potts models in $d = 3$..... 21
2.4 Nearest-neighbor densities of q-state clock models in $d = 3$ 26
2.5 Nearest-neighbor densities of Potts models in $d = 3$..... 27
2.6 Nearest-neighbor densities of clock models 27
2.7 Magnetizations of Potts and clock models in $d = 3$..... 28

3.1 Migdal-Kadanoff transformation for $d = 3$ cubic lattice..... 34
3.2 Phase diagrams of spin-s Ising spin glasses in $d = 3$ 36
3.3 Transition temperatures as a function of spin s..... 37
3.4 Chaotic RG trajectories for various spin s values 39

4.1 Phase diagrams for cubic-spin spin-glass systems 45
4.2 Nematic and spin-glass transition temperatures vs n..... 46
4.3 RG sinks of the phases for $n = 3$..... 47
4.4 Fixed distribution of the spin-glass phase sink 48
4.5 Chaotic RG trajectories and Lyapunov exponents..... 50

5.1 Phase diagrams for $n = 2$ and $n = 3$ cubic-spin systems..... 57
5.2 Phase diagrams under diagonal magnetic fields ($p = 0$) 57
5.3 Phase diagrams under magnetic fields ($p = 1$) 59
5.4 Phase diagrams under magnetic fields ($p = 0.5$) 60
5.5 Fixed distributions of spin-glass phase sinks 64

6.1 RG transformation for surfaced hierarchical model..... 70
6.2 Phase diagrams for spin-glass sponges 72
6.3 Chaotic RG trajectories for spin-glass sponges..... 74

7.1 Migdal-Kadanoff transformation and hierarchical lattices..... 83
7.2 Phase diagrams of $q = 4, 5$ Potts-clock models..... 86
7.3 Strong-coupling behaviors in $d = 2$ and $d = 3$ 87

8.1 Exact solution of $d = 2$ hierarchical model..... 96
8.2 Phase diagram of XY Ashkin-Teller model in $d = 2$..... 98
8.3 RG trajectory terminal energy functions in XY model..... 100
8.4 Fixed-line potential functions in XY Ashkin-Teller model 102

8.5 Examples of fixed-line potential functions in F phase 103

9.1 RG cells for $d = 1$ 109
9.2 Phase diagram of $d = 1$ long-range Ising model 111
9.3 Critical exponents vs interaction range a 112
9.4 Phase diagram and chaos in $d = 1$ spin-glass system 114

10.1 Phase diagrams of $d = 1$ Blume-Capel model 120
10.2 Critical and tricritical temperatures vs a 124

11.1 Metastable droplet magnetizations vs droplet size 132
11.2 Maximal droplet sizes vs number of Potts states 134
11.3 Maximal droplet sizes vs magnetic field 135
11.4 Hysteresis loops for different temperatures 136
11.5 Hysteresis loops for different system sizes 137
11.6 Hysteresis loops for different q values 137

LIST OF TABLES

2.1 Critical temperatures of Potts and clock models 29

4.1 Lyapunov exponents for cubic-spin spin-glass systems..... 50

5.1 RG sinks of finite-field thermodynamic phases 64
5.2 Phase proliferation under magnetic field..... 64

6.1 Lyapunov exponents for chaos in spin-glass sponges 75
6.2 Runaway exponents for chaos in spin-glass sponges..... 76

7.1 Sinks of ordered phases..... 85
7.2 Frustration-driven vs symmetry-competition-driven complexity 90

8.1 Attractor structures across the thesis 105
8.2 Discrete vs continuous Ashkin-Teller constructions 106

10.1 Cell-spin assignment rules..... 118

12.1 Chaos characteristics in spin-glass systems 142
12.2 Phase counts across representative systems 142
12.3 Critical-temperature behaviors and asymptotic trends 143

LIST OF SYMBOLS

Greek Symbols

α	Specific heat critical exponent
β	Inverse temperature, $1/k_BT$; also magnetization critical exponent
γ	Susceptibility critical exponent
δ	Magnetization critical exponent at T_c
$\delta(s_i, s_j)$	Kronecker delta function: 1 if $s_i = s_j$, 0 otherwise
Δ	Chemical potential (Blume-Capel model)
η	Correlation function critical exponent
θ, ϕ	Spin angles for continuous spin orientations
λ	Lyapunov exponent
ν	Correlation length critical exponent
ξ	Correlation length
σ	Internal degrees of freedom in cell-spin construction

Latin Symbols

a	Power-law decay exponent for long-range interactions
b	Length rescaling factor
$\mathscr{B}_\alpha(\{J\})$	RG flow function for coupling J_α (Wilson's beta function)
d	Spatial dimensionality
d_S	Surface dimensionality
$E(s_i, s_j)$	Interaction energy between spins at sites i and j
$f(k,l)$	Double Fourier coefficients
G	Additive constant in Hamiltonian
H	Magnetic field
$\mathscr{H}$	Hamiltonian
J	Exchange interaction strength
J_r	Interaction at separation distance r

K	Dimensionless coupling, βJ; also biquadratic coupling
k_B	Boltzmann constant
L	System linear size
L_C	Critical (maximal) droplet size
M	Magnetization
n	Number of spin components
N	Number of nearest-neighbor pairs
N_b	Number of bonds produced per substitution
p	Probability of antiferromagnetic bond
q	Number of states in Potts/clock models
$Q_{\alpha\beta}$	Nematic order parameter tensor
r	Separation distance
$\mathbf{R}$	Recursion matrix, $\partial \mathbf{E}'/\partial \mathbf{E}$
s	Spin magnitude
s_i, $\vec{s}_i$	Spin variable (scalar or vector) at site i
$\vec{t}_i$	Second vector spin at site i (Ashkin-Teller model)
T	Temperature
T_c	Critical temperature
$\mathbf{T}(s_i, s_j)$	Transfer matrix
$U(n_i, n_j)$	Bond-state densities
y_H	Magnetic field scaling exponent
y_R	Runaway exponent
y_T	Temperature scaling exponent
Z	Partition function

Notation Conventions

$'$ (prime)	Denotes renormalized quantities
$\tilde{}$(tilde)	Denotes bond-moved quantities
$*$ (star)	Denotes fixed-point values
$\langle \cdot \rangle$	Thermal average
$\langle ij \rangle$	Sum over nearest-neighbor pairs

LIST OF ACRONYMS AND ABBREVIATIONS

A, AF	Antiferromagnetic (phase)
A_σ	Locked antiferromagnetic phase (Ashkin-Teller model)
BKT	Berezinskii-Kosterlitz-Thouless
D	Disordered (phase)
F	Ferromagnetic (phase)
F_σ	Locked ferromagnetic phase (Ashkin-Teller model)
FRG	Functional renormalization group
MBL	Many-body localization
MK	Migdal-Kadanoff
Q	Quadrupolar (phase)
RG	Renormalization group
SG	Spin glass (phase)
XY	XY model (planar rotator model)

1. INTRODUCTION: THE ANATOMY OF COMPLEXITY

1.1 The Fundamental Mystery

Physics confronts emergence in its most precise form through phase transitions. Consider a piece of iron: at the atomic scale, 10^{23} quantum spins follow simple rules, yet heating through 1043 K produces a sharp transition from ferromagnet to paramagnet. The transition is nonanalytic in the thermodynamic limit, involving the cooperative rearrangement of Avogadro's number of degrees of freedom at a single critical temperature.

More puzzling still: many microscopically distinct uniaxial ferromagnets undergo transitions at different temperatures and with different nonuniversal amplitudes, yet share the same set of critical exponents within a universality class. Microscopic details—atomic mass, lattice structure, and interaction strengths—largely wash out near criticality, leaving a small set of universal numbers. Meanwhile, other Hamiltonians generate far richer behavior: phase-diagram proliferation under fields, reentrant transitions where order gives way to disorder gives way to order again, and glass phases whose defining signature is chaotic scale evolution rather than symmetry breaking.

This poses three profound questions that motivate this thesis. First, the emergence question: how do simple microscopic rules generate complex macroscopic behavior? Second, the universality question: why do microscopically different systems exhibit identical macroscopic properties? Third, the complexity question: what determines whether a system is simpler (three phases like water) or more complex (dozens of phases like magnetic materials)? A unifying route into all three questions runs through scale transformation—how descriptions change as degrees of freedom are systematically eliminated.

1.2 Complexity as Scale-Dependent Emergence

Before proceeding, we must define "complexity" with precision. The term has accumulated dozens of meanings across disciplines—computational complexity, algorithmic

information content, network centrality, thermodynamic entropy. For this thesis, none of these suffices. High entropy does not imply complexity; an ideal gas has high entropy yet remains structurally simple, with thermodynamics determined by a small set of state variables. Large system size does not imply complexity; 10^{23} identical Ising spins are conceptually simpler than ten competing symmetries. Computational difficulty does not imply physical complexity; many NP-hard problems involve no phase transitions at all.

In this thesis, "complexity" is used in an operational, model-based sense: it is diagnosed by the geometry of renormalization-group flows generated by a Hamiltonian under a specified coarse-graining scheme—implemented here in a setting where the transformation is exact on the hierarchical lattices under study. This choice does not claim exclusivity over other complexity measures; rather, it provides a disciplined language for comparing phase-structure richness, extended attractors, and chaotic rescaling across a unified portfolio of spin models.

In comparatively simple settings, repeated coarse-graining drives the effective Hamiltonian toward low-dimensional attractors—stable fixed points representing conventional ordered or disordered phases. For example, in the ferromagnetic Ising model at fixed spatial dimension and symmetry content, RG flows approach either an ordered sink or a disordered sink, with the critical manifold separating their basins of attraction.

In "complex" systems, the RG flow exhibits richer topology. Phase complexity refers to multiple distinct thermodynamic phases emerging from a single microscopic Hamiltonian, connected by a network of first-order boundaries, continuous transitions, and multicritical points. Flow complexity refers to RG trajectories that do not converge to fixed points but exhibit extended or chaotic dynamics—fixed lines in algebraically ordered phases where the attractor is a continuous manifold of scale-invariant states, or chaotic attractors in spin-glass phases where coupling constants wander sensitively under iteration. Order complexity refers to phases lacking conventional local order parameters yet possessing long-range structure, such as algebraic order with power-law correlations or nematic order emerging from frustrated vector spins. Critical complexity refers to structure in the phase boundaries themselves—multicritical points where three or more phases meet, reentrant transitions, and phase boundaries whose order changes with coupling ratios.

Importantly, these four types of complexity are not properties of the microscopic Hamil-

tonian per se, but properties of the RG flow topology it generates. The same microscopic ingredients—spins, bonds, symmetries—produce vastly different macroscopic behavior depending on how competing interactions organize under scale change. This perspective transforms the study of complexity from cataloging phenomenology to understanding flow structure.

Defining complexity through RG topology provides three advantages. First, it is quantifiable: we can count phases, measure Lyapunov exponents, determine fixed-line dimensionality, and classify multicritical points. Second, it is mechanistic: because the mechanisms that generate distinct flow topologies can often be identified directly from symmetry content, frustration structure, and dimensional constraints, one can frequently anticipate which qualitative forms of complexity are plausible before computing the full phase diagram. Third, it connects to robust features of phase behavior, and it is universal in that sense. Within specific model families on the hierarchical lattices studied here, the qualitative structure of RG flows—whether trajectories converge to fixed points, wander on fixed lines, or exhibit chaotic dynamics—proves stable across variations in microscopic parameters. For instance, in the spin-s Ising spin-glass family, the Lyapunov exponent characterizing chaos takes a stable value of approximately 1.93 independent of spin magnitude s, from $s = 1/2$ to $s \to \infty$. This independence from microscopic Hilbert space dimension suggests that chaotic flow topology, once established by frustration, is insensitive to certain microscopic details within a model family—though different model families, lattice structures, or symmetry classes yield different quantitative values.

This thesis treats RG not merely as a computational tool for extracting exponents, but as a disciplined account of how macroscopic descriptions emerge from microscopic ones under loss of resolution. In that sense, RG provides a concrete mechanism—within statistical mechanics—for linking microscopic structure to macroscopic phases and their organizing flow topology.

1.3 Historical Development

1.3.1 From Boltzmann to Onsager

The dream of statistical mechanics, since Boltzmann and Gibbs in the 1870s, was reduction: derive all macroscopic thermodynamics from microscopic mechanics through the

partition function

$$Z = \sum_{\text{microstates}} e^{-\beta E}. \tag{1.1}$$

For ideal gases and weakly interacting systems, this program succeeded spectacularly. Thermodynamic quantities follow from $F = -k_B T \ln Z$, and the partition function factorizes for independent particles, making everything calculable.

But strongly interacting systems resisted. The Ising model—introduced by Wilhelm Lenz in 1920 and solved by his student Ernst Ising in one dimension in 1925—became the paradigmatic challenge. Ising found no finite-temperature phase transition in $d = 1$ and concluded the model was "of no further interest" for understanding ferromagnetism. This was spectacularly wrong; the same model in $d \geq 2$ exhibits exactly the cooperative phenomena Ising sought. The problem was that strongly correlated systems require fundamentally different tools.

Lars Onsager's 1944 exact solution of the two-dimensional Ising model on the square lattice was a watershed (Onsager, 1944). He proved that strong correlations could produce singular behavior—a logarithmic specific heat divergence—and spontaneous symmetry breaking at finite temperature. But the solution was a mathematical tour de force providing little physical intuition and offering no systematic path to other models. Each new model required a new heroic calculation.

1.3.2 The renormalization group revolution

Meanwhile, mean-field theory offered a systematic but approximate approach. The Weiss molecular field approximation, generalized by Landau, predicted phase transitions with universal critical exponents: $\beta = 1/2$, $\gamma = 1$, $\nu = 1/2$. But experiments contradicted these predictions. In $d = 3$, measurements found $\beta \approx 0.32$, not 0.5. In $d = 2$, mean field incorrectly predicted no transition (contradicting Onsager) or wrong exponents (depending on how it was applied).

By the 1960s, statistical mechanics faced a conceptual crisis. Exact solutions were unattainable except in special cases. Mean-field theory gave systematically wrong answers. The connection between microscopic rules and macroscopic behavior remained opaque.

The breakthrough came from Leo Kadanoff (1966) and Kenneth Wilson (1971a). Kadanoff observed that at a critical point, where the correlation length ξ diverges, the system ex-

hibits scale invariance—it looks the same at all length scales. Therefore, he argued, physical properties should remain invariant under simultaneous rescaling of length, interactions and fields. He introduced "block spins": coarse-grain the lattice by replacing blocks of spins with effective block spins, generating a renormalized Hamiltonian at the new scale.

Wilson transformed this insight into a complete framework. He treated the RG as a flow in the space of all possible Hamiltonians. Start with some microscopic Hamiltonian H. Integrate out short-distance degrees of freedom, rescale, and obtain H'. Repeat to generate a trajectory in coupling space:

$$\frac{dJ_\alpha}{dl} = \mathscr{B}_\alpha(\{J\}), \tag{1.2}$$

where $l = \ln(b)$ is "RG time." Fixed points $\mathscr{B}_\alpha = 0$ represent scale-invariant theories. Critical points are unstable fixed points; systems flow toward close proximity of criticality, become almost scale-invariant, then flow away. Universality emerges naturally: different microscopic Hamiltonians in the same basin of attraction flow to the same fixed point, hence exhibit identical critical behavior characterized by eigenvalues y_α at that fixed point.

1.3.3 Beyond critical exponents: phase structure and chaos

Wilson's framework explained universality and critical phenomena—behavior at continuous phase transitions, predicted critical exponents from flow eigenvalues, derived scaling laws from RG structure, and revealed why mean-field theory fails (it neglects fluctuations, valid only as $d \to \infty$). But it opened deeper questions that motivate this thesis: The q-state Potts model revealed that RG explains not just criticality but phase structure itself. Nienhuis et al. (1979) showed first-to-second-order transition changeovers, multiple ordered phases, and multicritical points emerging from RG analysis. What microscopic features generate multiple phases? Berezinskii (1970), Kosterlitz and Thouless (1973) discovered that systems with continuous symmetry in $d = 2$ exhibit algebraic order—power-law correlations without conventional symmetry breaking—at finite temperature. The RG flow approaches not a fixed point but a fixed line, yielding continuously varying critical exponents. When does RG produce extended attractors rather than points? Edwards and Anderson (1975) introduced quenched disorder creating frustration—the impossibility of simultaneously satisfying all interactions. Berker and McKay (1984) found that hierarchical-lattice RG for spin glasses produces chaotic flows: coupling constants don't converge but oscillate chaotically under iteration. The glass phase is characterized by

chaos under scale transformation. How does frustration generate chaotic attractors? The Ashkin-Teller model (Ashkin and Teller, 1943)—two coupled Ising models—exhibits multiple ordered phases and rich multicriticality. When generalized to continuous spins (XY-Ashkin-Teller), it produces multiple algebraic phases. How does symmetry structure determine complexity? Thouless (1969) and Dyson (1969) showed that power-law interactions $J(r) \sim r^{-a}$ fundamentally alter universality, with mean-field theory becoming exact for sufficiently long range. How does interaction range modulate the basic complexity generators?

These developments, spanning 1970–2000, established that RG can address far more than critical exponents. The topology of RG flows—their attractors, dimensionality, stability, and chaotic properties—encodes the full richness of macroscopic phases.

The mechanisms we term "generators" were identified in foundational work: frustration's role in spin-glass chaos was established by McKay et al. (1982a); symmetry competition producing multiple phases was demonstrated in Ashkin-Teller and Potts models by Ditzian et al. (1980) and Nienhuis et al. (1979); and scale invariance in 2D XY systems was understood through the work of Berezinskii (1970), Kosterlitz and Thouless (1973), and Nelson and Halperin (1979). Our contribution is not the discovery of these mechanisms but their systematic comparison within a unified hierarchical-lattice setting.

1.4 The Renormalization Group as Mechanism

1.4.1 What coarse-graining preserves and destroys

This thesis treats the RG transformation not as a calculational trick but as the actual physical process connecting microscopic and macroscopic scales. When we observe a material at macroscopic length scales—say, millimeters—we are inherently performing coarse-graining. Short-wavelength fluctuations average out; only long-wavelength modes remain visible. The RG transformation formalizes this averaging.

Coarse-graining removes fast modes (high-frequency fluctuations), short-distance details (atomic positions, lattice spacing), and unprotected microscopic asymmetries. It preserves slow modes (long-wavelength correlations), protected symmetries (which cannot be broken by smooth averaging), and topological features (which survive continuous deformations). Most importantly, it reveals which interactions dominate at different scales,

whether competing interactions can be simultaneously satisfied (or generate frustration), and whether any hidden symmetries emerge at long distances. Crucially, coarse-graining is not always simplifying. In a ferromagnet, successive coarse-graining drives the system toward perfect alignment—a simple final state. But in systems with competing symmetries, no single configuration satisfies all constraints simultaneously. The competition persists across scales, manifesting as multiple phases. In frustrated systems, the impossibility of satisfying all interactions generates complex, scale-dependent patterns—the signature of chaotic flows.

1.4.2 Position-space methods and hierarchical lattices

While Wilson's momentum-space RG is conceptually transparent, position-space RG is computationally tractable. This thesis employs the Migdal-Kadanoff approximation and its exact realization on hierarchical lattices (Migdal, 1975; Kadanoff, 1976). The Migdal-Kadanoff procedure for a d-dimensional lattice with rescaling factor b consists of bond-moving (removing certain bonds, redistributing their interaction strength to remaining bonds) followed by decimation (summing over intermediate spins along remaining bonds). This transforms a d-dimensional problem into a sequence of effectively one-dimensional decimations, which are exactly solvable. For the Ising model, this yields a recursion relation $J' = J'(J,b,d)$, connecting the dimensionless coupling J at successive RG scales.

A hierarchical lattice is constructed by recursive self-similar substitution. Each bond is replaced by a small graph; iterating this procedure generates a lattice with well-defined dimensionality $d = \ln N_b / \ln b$, where N_b is the number of bonds produced per substitution. For hierarchical lattices, the RG transformation is exact: decimation over internal spins in each substitution graph yields exact recursion relations with no approximation in the thermodynamic limit (Berker and Ostlund, 1979; Griffiths and Kaufman, 1982; Kaufman and Griffiths, 1984).

1.4.3 Transfer matrices and partition function conservation

These structures are not merely mathematical conveniences. Hierarchical lattices provide idealized, exactly renormalizable proxies for systems with scale-recursive connectivity (including certain fractal or porous structures and hierarchical network motifs). However, quantitative predictions (critical temperatures, exponent values) from hierarchical lattices

should not be directly compared to experiments on cubic or other Euclidean lattices. The transfer is at the level of qualitative mechanisms: whether phases exist, whether chaos occurs, and how flow topology changes with parameters. Monte Carlo studies on Euclidean lattices provide the quantitative benchmarks. Hierarchical lattices' main value here is methodological: they let RG flow topology be computed globally and unambiguously.

The primary technical implementation for most chapters uses transfer matrices. For nearest-neighbor interactions on hierarchical lattices, the partition function can be written in terms of local Boltzmann weights as

$$Z = \sum_{\{s\}} \prod_{\langle ij \rangle} e^{-\beta H_{ij}(s_i, s_j)} \equiv \sum_{\{s\}} \prod_{\langle ij \rangle} T_{ij}(s_i, s_j), \tag{1.3}$$

where $T_{ij}(s_i, s_j) := e^{-\beta H_{ij}(s_i, s_j)}$ is the transfer matrix (local weight) encoding the Boltzmann factor for spin configurations at sites i and j. Under an RG decimation step that sums over an internal spin s_k, these weights compose by contraction:

$$T'_{ij}(s_i, s_j) = \sum_{s_k} T_{ik}(s_i, s_k)\, T_{kj}(s_k, s_j), \tag{1.4}$$

yielding an induced recursion $T \mapsto T' = \mathscr{F}[T]$ in the space of effective interactions. This formalism is employed in Chapters 2–8 and 11.

In Chapters 9–10, for systems with power-law interactions in $d = 1$, the standard transfer-matrix approach is not directly applicable because interactions couple spins at all separations. Transfer matrices work naturally for nearest-neighbor interactions where the partition function factorizes along bonds, while the cell-spin method is required for long-range interactions where every pair of spins interacts and a single transfer matrix is insufficient. Instead, Chapters 9 and 10 employ the Niemeyer–van Leeuwen cell-spin method (Niemeyer and van Leeuwen, 1974; van Leeuwen, 1975), which constructs renormalization-group recursion relations through partition function conservation:

$$Z = \sum_{\{s\}} e^{-\beta \mathscr{H}(\{s\})} = \sum_{\{s'\}} \sum_{\{\sigma\}} e^{-\beta \mathscr{H}(\{s'\}, \{\sigma\})} = \sum_{\{s'\}} e^{-\beta' \mathscr{H}'(\{s'\})}, \tag{1.5}$$

where cell-spins s' are defined as the sign of the sum of site-spins within each cell, and σ represents the internal degrees of freedom. This approach tracks renormalized interactions J'_r for multiple separation distances r, rather than manipulating a single transfer matrix.

Both approaches—transfer-matrix composition and partition-function conservation—generate recursion relations that define a flow in coupling-constant space. The topology of this flow determines the phase structure of the system.

Thermodynamic phases correspond to attractors of this map: ferromagnetic sinks with aligned spins, disordered sinks with independent spins, antiferromagnetic sinks with alternating spins, glass attractors with chaotic orbits, and algebraic attractors with fixed lines. Phase boundaries are separatrices between basins of attraction, flowing to unstable fixed points. We employ several quantitative measures: phase counting, multicritical structure classification, Lyapunov exponents for chaotic flows, runaway exponents for strong-coupling flows, and fixed-line dimensionality for algebraic phases. These quantities convert the qualitative notion of 'complexity' into measurable characterizations, providing systematic criteria that go beyond phenomenological phase classification.

1.5 Organizing Principles: Generators and Modulators of Complexity

1.5.1 Three complexity generators

The generators-modulators framework presented here is not claimed as a fundamental theory but rather as an organizational taxonomy that helps systematize how different microscopic features manifest as macroscopic complexity within the RG paradigm. The individual mechanisms—frustration, symmetry competition, scale invariance—are well-established in the literature; our contribution is their systematic comparison within a unified computational setting.

The three generators are frustration, symmetry competition, and scale invariance. When interactions compete such that no configuration simultaneously minimizes all local energies, the system is frustrated. Under RG, frustration prevents flow to simple attractors; instead, as interactions combine under coarse-graining, they can reinforce frustration at longer scales, generating chaotic RG flows where coupling constants wander bounded regions of parameter space in a sensitively dependent manner. In systems with high-dimensional spin spaces, frustration can generate new symmetries: the nematic phase—tensor order from vector disorder—emerges between low-temperature glass and high-temperature disorder. External fields break degeneracies in frustrated systems, revealing hidden structure and producing phase-diagram proliferation.

When a Hamiltonian contains multiple symmetry groups with incompatible ordering tendencies, scale transformation amplifies their competition. Neither symmetry can be fully satisfied; the system responds by generating multiple distinct phases, each representing a different compromise between symmetries. Merging permutation-symmetric (Potts) and rotation-symmetric (clock) interactions produces multiple ordered phases with rich multicritical structure. In continuous-spin systems, symmetry competition produces not just multiple phases but multiple algebraic phases, each subtended by fixed lines.

When continuous symmetries exist in low dimensions, the Mermin-Wagner theorem forbids conventional long-range order at finite temperature. Yet the system need not be disordered; it can exhibit algebraic order with power-law correlations and no characteristic length scale. RG flows converge to fixed lines—continuous families of scale-invariant states with continuously varying critical exponents. Systems on a fixed line are critical everywhere, lacking a length scale throughout the entire phase.

1.5.2 Three complexity modulators

The three modulators are interaction range, external fields, and spatial topology. Power-law interactions $J(r) \sim r^{-a}$ change effective dimensionality: long-range systems behave more mean-field-like, short-range systems are fluctuation-dominated. In long-range spin glasses, frustration becomes pervasive with chaotic couplings at every separation distance. Uniform magnetic fields explicitly break spin-rotation symmetry; in complex systems with internal degeneracy, fields act as symmetry probes revealing latent structure. The boundary conditions and geometric structure of the system can create additional degrees of freedom with independent RG dynamics; in spin-glass sponges with fractal surfaces, surface chaos can decouple from bulk chaos.

1.5.3 Scope and limitations of the framework

This framework is intended as an organizational taxonomy for the systems studied in this thesis, not as a complete predictive theory. The three generators and three modulators provide convenient language for discussing how different microscopic features produce different forms of macroscopic complexity. However, the framework does not claim exhaustiveness—other mechanisms may be relevant in systems not studied here—nor does it provide a way to predict, without calculation, the precise phase structure a given Hamiltonian will exhibit. The value of the framework lies in organizing and com-

paring results across model families, not in replacing detailed RG analysis.

1.6 Thesis Overview and Principal Contributions

The remainder of this thesis develops and demonstrates the generators-modulators framework through exact solutions of hierarchical-lattice models. Chapter 2 establishes the technical and thermodynamic baseline with complete density calculations for q-state Potts and clock models. It introduces the transfer-matrix methodology and density recursion techniques, demonstrates that even simple ferromagnets exhibit non-trivial emergent behavior through interface density reentrance, and provides reference phase diagrams against which subsequent complexity can be measured.

Chapters 3 through 6 develop frustration as a complexity generator. Chapter 3 establishes that spin-glass chaos is universal across spin magnitudes in spin-s Ising models, with Lyapunov exponent $\lambda \approx 1.93$ independent of spin magnitude. Chapter 4 reveals that frustration can generate new forms of order: a nematic phase emerges in n-component cubic-spin spin glasses for $n \geq 3$. Chapter 5 investigates how external fields interact with frustration, producing 17 distinct ordered phases with novel phase-diagram topologies. Chapter 6 examines how spatial topology modulates frustrated systems, finding both bulk-driven and intrinsic surface chaos in spin-glass sponges.

Chapters 7 and 8 develop symmetry competition. Chapter 7 merges Potts and clock interactions, producing five ordered phases with rich multicritical structure. Chapter 8 extends to continuous spins, where symmetry competition meets scale invariance, in the XY-Ashkin-Teller model, producing four algebraically ordered phases each subtended by fixed lines of potential surfaces with continuously varying critical exponents.

Chapters 9 and 10 investigate interaction range as a modulator. Chapter 9 studies the $d = 1$ Ising model with long-range interactions across ferromagnetic, antiferromagnetic, and spin-glass cases, finding piecewise chaotic interaction functions in the spin-glass phase. Chapter 10 applies long-range interactions to the Blume-Capel model, where range and vacancy chemical potential produce giant reentrance.

Chapter 11 extends the RG methodology to metastable states, determining existence limits of metastable Potts droplets and calculating hysteresis loops across first-order transitions. Chapter 12 synthesizes the thesis, evaluating the scope and limitations of the framework and identifying directions for future research.

This thesis makes contributions at three levels. Conceptually, it proposes a constrained, operational taxonomy that organizes how RG flow topology becomes elaborate in the model families treated here. Methodologically, it demonstrates that exact hierarchical-lattice solutions provide physically meaningful insights into complex systems. Phenomenologically, it establishes specific quantitative results: universal spin-glass chaos with $\lambda = 1.93$ for all spin-s in Ising model family, emergent nematic phase for $n \geq 3$ cubic-spin components, field-induced phase proliferation to 17 phases, distinct surface and bulk Lyapunov exponents, five-phase Potts-clock diagrams, four algebraic XY-Ashkin-Teller phases with fixed lines, piecewise chaotic interactions in long-range spin glasses, and giant reentrance in the long-range Blume-Capel model.

2. THERMODYNAMIC FOUNDATIONS

2.1 Introduction

Although originally introduced for critical phenomena, renormalization-group calculation gives the total thermodynamics of a system at and away from phase transitions (Berker and Ostlund, 1979). To effect this, the recursion relations of the local densities are needed, causing the calculation to be more complicated than that for phase boundaries and critical exponents. This calculation is carried out here for two families of models, namely the Potts (Berker et al., 1978; Nienhuis et al., 1979; Andelman and Berker, 1981) and clock models (Berker and Nelson, 1979), each with q states on a hierarchical lattice (Berker and Ostlund, 1979; Griffiths and Kaufman, 1982; Kaufman and Griffiths, 1984) in three spatial dimensions, $d = 3$. The calculation is exact for the hierarchical lattice and is considered approximate for a cubic lattice (Migdal, 1975; Kadanoff, 1976). The temperature functions and symmetry-breaking behaviors of dozens of local densities are derived, and interesting behaviors are found and explained, such as a reentrance behavior in the interface densities. The models are similarly defined but they exhibit different behaviors, such as the q saturation of the magnetization and the phase transitions as q goes to infinity, which is also explained.

This chapter serves three purposes within the broader thesis framework. It establishes the transfer-matrix formalism, density recursion relations, and RG flow analysis that form the technical backbone for all subsequent chapters. The Potts and clock models studied here are "simple" in the sense of Chapter 1: they possess single ordered phases, simple phase sinks, and conventional symmetry breaking. By establishing the complete thermodynamics of these baseline models, we create a reference against which the complexity of subsequent models can be measured. Finally, even these simple models exhibit non-trivial emergent behavior—the reentrance of interface densities discovered here demonstrates that coarse-graining reveals subtleties invisible to mean-field intuition.

2.2 Model Definitions

2.2.1 The *q*-state Potts model

These general q-state models are simply defined by the following Hamiltonians. For the Potts models,

$$-\beta\mathscr{H} = \sum_{\langle ij \rangle} J\delta(s_i, s_j), \tag{2.1}$$

where $\beta = 1/k_B T$. At site i, the spin $s_i = a, b, \ldots$ can be in q different states, the delta function $\delta(s_i, s_j) = 1$ for $s_i = s_j$ and 0 otherwise, and $\langle ij \rangle$ denotes summation over all nearest-neighbor pairs of sites.

2.2.2 The *q*-state clock model

For the clock models,

$$-\beta\mathscr{H} = \sum_{\langle ij \rangle} J\cos(\vec{s}_i \cdot \vec{s}_j), \tag{2.2}$$

where at site i the spin $\vec{s}_i$ can point in q different directions $\theta_i = 2\pi n_i/q$ in the xy plane, with $n_i = 0, 1, \ldots, q-1$ providing the q different possible states. The limit $q \to \infty$ of the clock model gives the XY model, which we also explore here, with results (physically explainably) quite different from the $q \to \infty$ limit of the Potts model (Fig. 2.2).

2.2.3 Symmetry distinctions

The key symmetry distinction is that the Potts model possesses full permutational symmetry with no notion of "neighboring" states—every state is equidistant from every other. The clock model possesses rotational symmetry with states having a natural geometric relationship through their angles.

2.3 Renormalization-Group Formulation

2.3.1 Transfer matrix construction

Our aim is to calculate all of the bond-state densities [there are $q(q+1)/2$ of them],

$$U(n_i,n_j) = \langle \delta(s_i,n_i)\delta(s_j,n_j)\rangle, \tag{2.3}$$

where (i,j) are the sites on each end of the bond, and n_i designates one of q possible states of the spin s_i. These bond-state densities are obtained from the partition function Z,

$$U(n_i,n_j) = \frac{1}{N}\frac{\partial \ln Z}{\partial E(n_i,n_j)}, \tag{2.4}$$

where N is the number of nearest-neighbor pairs in the system, and $E(n_i,n_j)$ is the dimensionless (reduced) energy assigned to the bond when its sites are in states (n_i,n_j). Before any renormalization, these bond energies are given by Eqs. (2.1) and (2.2),

$$E(n_i,n_j) = J\delta(n_i,n_j) \quad \text{and} \quad J\cos(2\pi(n_i-n_j)/q), \tag{2.5}$$

for the Potts and clock models, respectively. The $E(n_i,n_j)$ are the (large number of; see below) renormalization-group flow variables, and Eqs. (2.5) give the initial conditions, parametrized by temperature J^{-1}, of the renormalization-group flows. The forms in Eqs. (2.5) are of course not conserved during the flows.

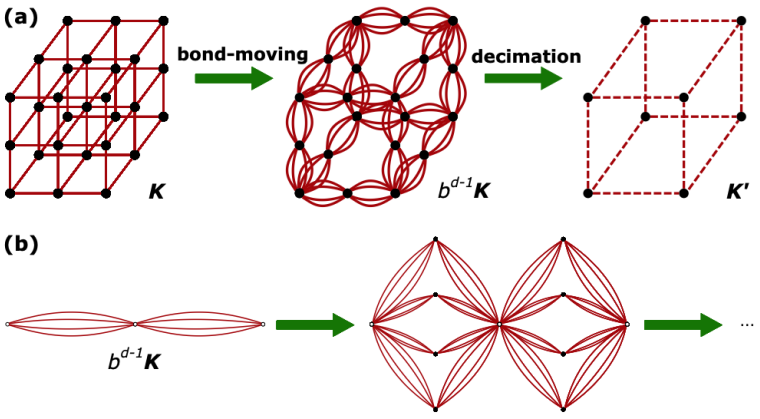


Figure 2.1: (a) Migdal-Kadanoff approximate renormalization-group transformation for the $d = 3$ cubic lattice with the length-rescaling factor of $b = 2$. (b) Construction of the $d = 3$, $b = 2$ hierarchical lattice for which the Migdal-Kadanoff recursion relations are exact. The renormalization-group solution of a hierarchical lattice proceeds in the opposite direction of its construction.

2.3.2 Bond moving and decimation

For our RG calculation, we use the Migdal-Kadanoff approximation, which, as shown in Figure 2.1(a), consists in bond-moving followed by decimation (Migdal, 1975; Kadanoff, 1976). This operation is equivalent to constructing the $q \times q$ transfer matrix $T(n_i, n_j) = \exp(E(n_i, n_j))$, taking the b^{d-1}th power of each element of the matrix (this is bond-moving) and multiplying the resulting matrix with itself (this is decimation).

2.3.3 Density recursion relations

For numerical convenience at the low-temperature sink of the flows, after every decimation (and before first starting the first renormalization), we subtract $E(aa)$ (for the Potts model) or $E(00)$ (for the clock model) from all $E(n_i, n_j)$, thus setting $E(aa) = 0$ or $E(00) = 0$ and introducing the additive constant NG in the Hamiltonian, which has the renormalization-group recursion relation

$$G' = b^d G + \tilde{G}, \tag{2.6}$$

where, here and everywhere, a prime refers to the renormalized system, the first term is the additive constants that the renormalized bond inherits from the b^d bonds it replaces, and the second term comes from compensating for the subtraction of $E(aa)$ or $E(00)$.

These recursion relations are then in terms of the elements [or equivalently their logarithms $E(n_i, n_j) = \ln(T(n_i, n_j))$] of the diagonal and upper left triangle of the transfer matrix (since this matrix is symmetrical). The number of these elements can be somewhat reduced by noting those identically equal by symmetry and not to be distinguished by possible spontaneous symmetry breaking, as is illustrated for the clock models below, but it will be seen that the number of the flow variables for the clock models increases rapidly with q. A large q calculation, such as the one we perform here for $q = 360$ to probe the $q \to \infty$ XY model limit, is best carried out by directly performing numerically the matrix operations described above on the 360×360 transfer matrix.

By contrast, for any q, by using the (partially broken under ordering) permutation symmetry of the Potts variables, we can reduce the number of renormalization-group flow variables to four, which makes it possible to treat any q, including $q = \infty$, as seen below.

The recursion relations obtained by the Migdal-Kadanoff approximation are exactly applicable to the exact solution of the hierarchical lattice shown in Fig. 2.1(b) (Berker and Ostlund, 1979; Griffiths and Kaufman, 1982; Kaufman and Griffiths, 1984). Thus, a "physically realizable" and therefore robust approximation is used. Physically realizable approximations have been used in polymers (Flory, 1986; Kaufman, 2018), disordered alloys (Lloyd and Oglesby, 1976), and turbulence (Kraichnan, 1961). Recent works using exactly soluble hierarchical lattices are in Refs. (Monthus, 2020; Sarıyer, 2019; Rocha-Neto et al., 2018; Ma et al., 2018; Boettcher and Li, 2018).

In each renormalization-group transformation, the densities obey the recursion relation

$$\mathbf{U} = b^{-d}\mathbf{U}' \cdot \mathbf{R}, \tag{2.7}$$

where the densities $\mathbf{U} \equiv [1, U(n_i, n_j)]$ are conjugate to the fields $\mathbf{E} \equiv [G, E(n_i, n_j)]$, and the recursion matrix is $\mathbf{R} = \partial \mathbf{E}'/\partial \mathbf{E}$. The exact Eq. (2.7) is obtained by using the derivative chain rule on $U = (1/N)\partial \ln Z/\partial E$, where Z is the partition function and N is the number of nearest-neighbor pairs of spins, and it is used to calculate densities from renormalization-group theory (Berker and Ostlund, 1979; Ilker and Berker, 2014a; Atalay and Berker, 2018).

In these defined vectors, the $E(aa)$ or $E(00)$ and $U(aa)$ or $U(00)$ are missing, since these energies are set to zero by the additive constant and therefore do not recur. $U(aa)$ and $U(00)$ are found from the sum rule $\sum_{n_i,n_j} U(n_i, n_j) = 1$. The other densities are calculated by iterating Eq. (2.7) until a stable fixed point (the sink of the thermodynamic phase) is reached. The densities $\mathbf{U}^*$ at the sink are the left eigenvectors of $\mathbf{R}$ with eigenvalue b^d and conclude the calculation by insertion to the right-hand side of Eq. (2.7). These will be discussed below specifically for each model. The unstable fixed point dividing the renormalization-group flows to the phase sinks, parametrized by J, yields the phase transition temperatures given in Fig. 2.2 and Table 2.1.

2.4 Results for Potts Models

2.4.1 Recursion relations

Because of the permutation symmetry of the model, namely that given the δ function, with respect to a given state, all other states are equivalent (unlike the clock model involving the product of slightly or more aligned vectors), the $q \times q$ transfer matrix manipulations

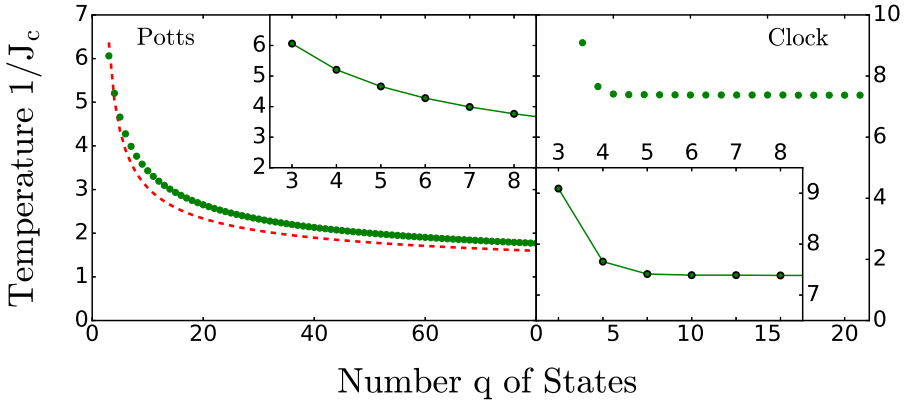


Figure 2.2: Calculated critical temperatures J_c^{-1} of the Potts and clock models as a function of the number of states q in $d = 3$. From this figure and from Table 2.1, it is seen that the clock model quickly (at as low as $q = 5$) settles to its $q = \infty$ (which is the XY model) value of $J_c^{-1} = 7.4$. The dashed line for the Potts critical temperatures is $J_c^{-1} = 7/\ln(q)$, derived here for strong coupling.

of the recursion relations given above can be reduced to four simple equations,

$$\begin{aligned} e^{E'(a\bar{b})+\tilde{G}} &= x(a\bar{b}) + x(a\bar{b})x(\bar{b}\bar{b}) + (q-2)x(a\bar{b})x(\bar{b}\bar{c}), \\ e^{E'(\bar{b}\bar{b})+\tilde{G}} &= x(a\bar{b})^2 + x(\bar{b}\bar{b})^2 + (q-2)x(\bar{b}\bar{c})^2, \\ e^{E'(\bar{b}\bar{c})+\tilde{G}} &= x(a\bar{b})^2 + 2x(\bar{b}\bar{b})x(\bar{b}\bar{c}) + (q-3)x(\bar{b}\bar{c})^2, \\ e^{\tilde{G}} &= 1 + (q-1)x(a\bar{b})^2, \end{aligned} \tag{2.8}$$

where the Potts state a has been singled out for possible spontaneous symmetry breaking, $\bar{b}$ represents any Potts state that is not a, and $\bar{c}$ represents any Potts state that is not a or the state in $\bar{b}$, and $x(a\bar{b}) \equiv e^{b^{d-1}E(a\bar{b})}$, etc. In the latter equation, the factor b^{d-1} represents bond-moving, and Eqs. (2.8) bring about the decimation with the bond-moved energies. The recursion matrix $\mathbf{R}$ is the 4×4 derivative matrix of Eqs. (2.8), and the density calculations can be done for any number of states q, including infinity. By a derivative matrix, we mean the derivatives of the renormalized quantities with respect to the unrenormalized quantities.

The recursion relations of Eqs. (2.8) flow to one of two phase sinks. On the high-temperature side, the sink of the disordered phase is

$$E(aa)^* = E(a\bar{b})^* = E(\bar{b}\bar{b})^* = E(\bar{b}\bar{c})^* = 0, \tag{2.9}$$

where $*$ denotes the fixed point value. The left eigenvector, with eigenvalue b^d, of the

recursion matrix $\mathbf{R}$ at this sink is

$$\begin{aligned}\mathbf{U}^* &= [1, U(a\overline{b})^*, U(\overline{bb})^*, U(\overline{bc})^*] \\ &= [1, \langle\delta(s_i,a)\delta(s_j,\overline{b}) + \delta(s_i,\overline{b})\delta(s_j,a)\rangle, \langle\delta(s_i,\overline{b})\delta(s_j,\overline{b})\rangle, \langle\delta(s_i,\overline{b})\delta(s_j,\overline{c})\rangle] \\ &= [1, 2(q-1)/q^2, (q-1)/q^2, (q-1)(q-2)/q^2]. \end{aligned} \tag{2.10}$$

Capping with Eq. (2.10) from left the repeated applications of Eq. (2.7), the densities $U(a\overline{b}), U(\overline{bb}), U(\overline{bc})$ are obtained over the entire temperature range of the high-temperature disordered phase. Finally,

$$U(ab) = U(a\overline{b})/U^*(a\overline{b}), \tag{2.11}$$

etc. gives the density for a specific pair of states (a,b).

On the low-temperature side, the sink of the ordered phase is

$$E(aa)^* = E(\overline{bb})^* = 0, \quad E(a\overline{b})^* = E(\overline{bc})^* \to -\infty. \tag{2.12}$$

A left eigenvector, with eigenvalue b^d, of the recursion matrix $\mathbf{R}$ at this sink is

$$\mathbf{U}^* = [1, 0, 0, 0]. \tag{2.13}$$

Calculation, as described after Eq. (2.10) above, gives the densities over the entire temperature range of the low-temperature ordered phase, showing spontaneous symmetry-breaking in favor of state a. This result is described in detail in the next subsection.

Another left eigenvector, with eigenvalue b^d, of the recursion matrix $\mathbf{R}$ at this sink is $[1,1,0,0]$. This eigenvector gives symmetry breaking in favor of one of the states b, namely one of the states that is not a. With the permutation mapping of the Potts model, this leads to results that are identical to the results involving symmetry breaking in favor of a. A linear combination of these two degenerate eigenvectors is of course also an eigenvector with the eigenvalue b^d, physically corresponding to the macroscopic coexistence of differently symmetry-broken phases.

It is noteworthy that throughout the renormalization-group flows,

$$E(aa) = E(\overline{bb}), \quad E(a\overline{b}) = E(\overline{bc}). \tag{2.14}$$

However, these interactions have to be distinguished in the recursion relations, enabling construction of the 4×4 recursion matrix $\mathbf{R}$, to calculate distinctly $U(aa), U(\overline{bb})$, and to see the symmetry breaking. This calculation is also going to lead to the full determination of the magnetization, as seen below.

2.4.2 Densities and interface density reentrance

The calculated nearest-neighbor densities of the q-state Potts models in $d = 3$ are given, for $q = 3, 4, 5, 6, 7, 10, 15, 20$, in Fig. 2.3. (For easy comparison, the densities for the clock models are given in the adjoining Fig. 2.4.) The upper curve is $U(aa)$ and $U(bb)$, which coincide in the disordered high-temperature phase and split in the low-temperature phase where symmetry is spontaneously broken in favor of state a. The lower curve is $U(ab)$ and $U(bc)$, which also coincide in the disordered high-temperature phase and split in the symmetry-broken low-temperature phase.

It is seen that the interface density $U(ab)$, between the symmetry-breaking and non-symmetry-breaking states, exhibits reentrance as temperature is lowered in the ordered phase, first increasing in value and then receding to zero at zero temperature. In Fig. 2.5, for comparison, the densities are plotted together for the different q values (and similarly for the clock models in the adjoining Fig. 2.6). The interface density reentrance is pronounced in the low q states, but continues for high q.

As temperature is lowered through the phase transition, the reentrance relies on the following mechanism: (i) Due to the increase in the sizes of the domains of the favored state $s_i = a$, the numbers increase for the $(s_i = a, s_j \neq a)$ pairs at the boundaries of these domains. (ii) As the sizes of the domains of the favored state $s_i = a$ increase further, upon further lowering the temperature these domains merge, eliminating the boundaries.

This reentrance is less pronounced for higher q, since the phase transition is at lower temperature and (ii) sets in before (i) develops.

Reentrance is the reversal of a thermodynamic trend as the system proceeds along one given thermodynamic direction. Since its observation in liquid crystals by Cladis (1975), this at-first-glance strange phenomenon has attracted attention due to the need for a physical mechanistic explanation, which has been disparate in disparate systems. Thus, in liquid crystals the explanation has been the relief of close-packed dipolar frustration by positional fluctuations (librations) (Netz and Berker, 1992; Indekeu et al., 1987), in

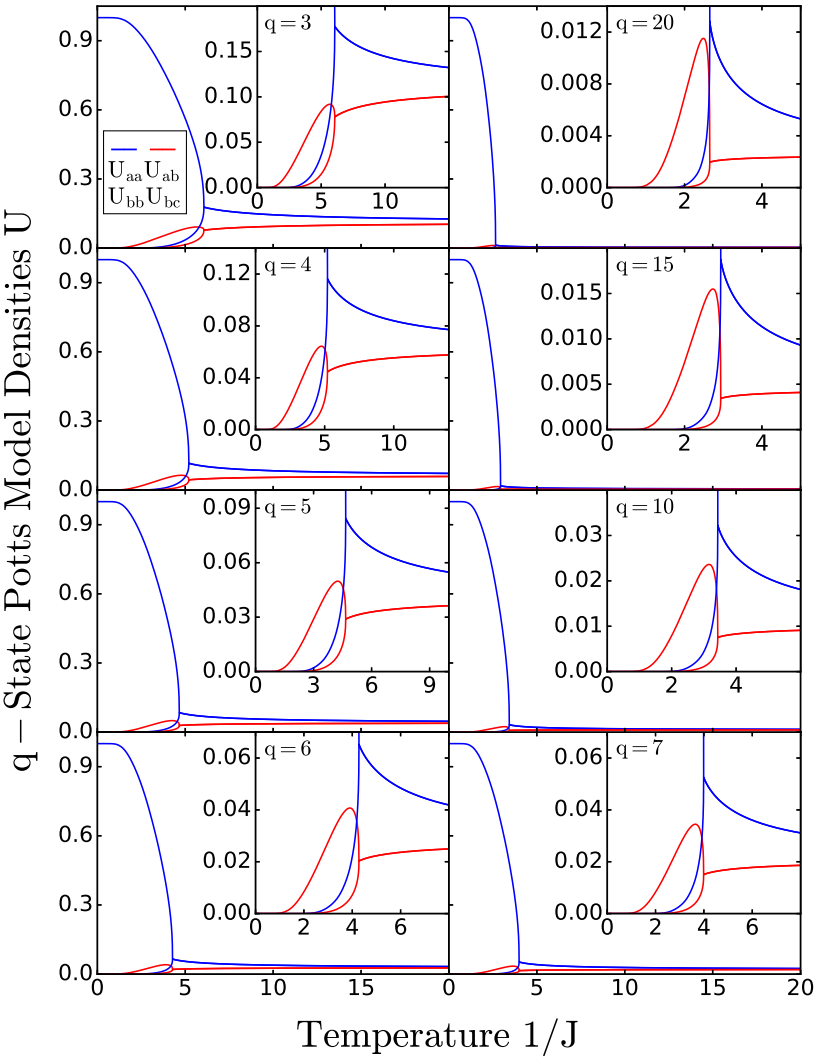


Figure 2.3: The calculated nearest-neighbor densities of the q-state Potts models in $d = 3$. The upper curve on the right is U_{aa} and U_{bb}, which coincide in the disordered high-temperature phase and split in the low-temperature phase where symmetry is spontaneously broken in favor of state a. The lower curve on the right is U_{ab} and U_{bc}, which also coincide in the disordered high-temperature phase and split in the symmetry-broken low-temperature phase. The interface density U_{ab} exhibits reentrance as temperature is lowered in the ordered phase, first increasing in value and then receding to zero at zero temperature.

closed-loop binary liquid mixtures the explanation has been the asymmetric orientational degrees of freedom of the components (Vause and Walker, 1982), and in surface adsorption the explanation has been the buffer effect of the second layer (Caflisch et al., 1985). In spin-glasses, where there is orthogonally bidirectional reentrance, the effect of frustration in both disordering and changing the nature of ordering (to spin-glass order) is the cause (Ilker and Berker, 2013). In cosmology, reentrance is due to high-curvature (black hole) gravity (Frassino et al., 2014; Dehghani et al., 2020).

In the current case of Potts (and clock; see below) interfacial density, in lowering the temperature, when the system orders in favor of state a, the preponderance of the latter also increases its interface with the other states. However, as this preponderance increases further and in fact takes over the system, the other states are eliminated and their interface with a is thus also eliminated. This happens for all q-state Potts and clock models.

The reentrance discovered here in interface densities is a relatively subtle effect, visible only in local observables rather than global order parameters. In later chapters, we will encounter more dramatic reentrance phenomena: the reentrance in the long-range Blume-Capel model (Chapter 10), where the system passes through disorder→order→disorder as temperature decreases, and the bidirectional reentrance in spin-glass systems (Chapters 3–6), where frustration drives qualitative changes in the nature of order itself.

The calculated bond-state densities also readily yield magnetizations, which will be discussed in Sec. 2.6, as well as the different behaviors of the two models in the $q \to \infty$ limit.

2.5 Results for Clock Models

Clock models do not have permutational symmetry, so the recursion relations for the diagonal and the top triangle of the $q \times q$ energies cannot be reduced to four equations [as in Eqs. (2.8) above]. Using the different symmetries for each q, the number of these energies that under renormalization group recur separately can be reduced, but still increase with q, eventually numerically burdening the algebra.

2.5.1 Renormalization-group calculation and six-energy flows for $q = 4$

In the three-state clock model, since with respect to any one state the other two states are equivalent, for $q = 3$ the clock and Potts models are identical, up to a factor of $1 - \cos(2\pi/3) = 3/2$ in the coupling constant J.

In the four-state clock model, the six energies that need to recur separately under renormalization group are

$$E(11) = E(33), \quad E(22), \quad E(12) = E(23), \quad E(01) = E(03), \quad E(02), \quad E(13), \tag{2.15}$$

where $E(mn)$ is the energy of neighboring spins with angles $2\pi m/q$ and $2\pi n/q$. The equalities result from the symmetries of the $q = 4$ state clock model, as the state with $m = 0$ is singled out for possible symmetry breaking. When, as we do here, the same energy label is assigned to different states that should have the same energy by symmetry, the derivative in Eq. (2.4) gives the sum of the densities of these states, as seen below.

The recursion relations are, similarly to Eqs. (2.8),

$$\begin{aligned} e^{E'(mn)+\tilde{G}} &= \sum_{k=0}^{q-1} e^{b^{d-1}E(mk)+b^{d-1}E(kn)}, \\ e^{\tilde{G}} &= \sum_{k=0}^{q-1} e^{b^{d-1}E(0k)+b^{d-1}E(k0)}. \end{aligned} \tag{2.16}$$

The renormalization-group flows and the calculation of the thermodynamic densities proceed as for the Potts models above. The recursion matrix is the 7×7 derivative matrix of $[G, E(mn)]$, where $E(mn)$ are the six energies of Eq. (2.15) and G is the additive constant as in Eq. (2.6), a captive variable of the renormalization-group flows of the $E(mn)$. By a derivative matrix, we again mean the derivatives of the renormalized quantities with respect to the unrenormalized quantities.

The left eigenvector with eigenvalue b^d of the recursion matrix at the phase sinks has the form $[1, \overline{U}(mn)]$, where $\overline{U}(mn)$ are the density sums conjugate to the recurring $E(mn)$. At the high-temperature disordered phase sink, all energies equal $E(00)$, namely zero, and $\overline{U}(mn) = z(mn)/q^2$, where $z(mn)$ is the degeneracy of $E(mn)$, namely $z = 2, 1, 4, 4, 2, 2$ for the energies in Eq. (2.15), also taking into account the degeneracy for label interchange when $m \neq n$. Repeated application of Eq. (2.7) then yields the six density sums $\overline{U}(mn)$ in

the entire temperature range of the disordered phase. The densities for individual states are obtained from the sums by $\langle \delta(mn) \rangle = U(mn) = \overline{U}(mn)/z(mn)$. For example,

$$\overline{U}(01)/z(01) = \langle [\delta(01) + \delta(10) + \delta(03) + \delta(30)] \rangle / 4 = \langle \delta(01) \rangle = U(01). \qquad (2.17)$$

Thus, when we reduce the number of the recurring energies using symmetries as in Eq. (2.15) and label interchange symmetry, the renormalization-group calculation yields the density sum $\overline{U}(01)$, which is then subjected to Eq. (2.17). At the low-temperature sink, in the left eigenvector with eigenvalue b^d, all $\overline{U}(mn) = 0$, and therefore $U(00) = 1 - \sum_{mn} U(mn) = 1$, symmetry is broken in favor of state 0. Repeated application of Eq. (2.7) then yields the six density sums $\overline{U}(mn)$ in the entire temperature range of the ordered phase. [The other left eigenvector with eigenvalue b^d is $\overline{U}(\overline{00}) = 1$, where $\overline{0}$ is a state other than 0, and all other recurring $\overline{U}(mn) = 0$, giving an equivalent phase and completing the picture of phase coexistence, as for the Potts models above.]

The calculated nearest-neighbor densities of the four-state clock model in $d = 3$ are shown in Fig. 2.4. The densities $U(00), U(11), U(33)$ coincide in the disordered high-temperature phase, and in the low-temperature phase $U(00)$ splits from $U(11), U(33)$ under the symmetry breaking favoring the state 0. Similarly, $U(01), U(03), U(12), U(23)$ coincide in the disordered high-temperature phase, and in the low-temperature phase $U(01), U(03)$ splits from $U(12), U(23)$ under the symmetry breaking. Similarly, $U(02), U(13)$ coincide in the disordered high-temperature phase, and in the low-temperature phase $U(02)$ splits from $U(13)$ under the symmetry breaking. The densities involving the 0 state split from their symmetric counterparts in the low-temperature phase, increasing their values. This is spontaneous symmetry breaking. Furthermore, the interface densities involving the 0 state exhibit reentrance as temperature is lowered in the ordered phase, first increasing in value and then receding to zero at zero temperature.

2.5.2 Renormalization-group flows of 8, 12, 15, and 20 energies for $q = 5, 6, 7, 8$

The calculations for $q = 5, 6, 7, 8$ are more extensive. Using symmetries grouping the same values of $|n - m|$, but grouping separately for positioning with respect to state 0, for the possibility of spontaneous symmetry breaking, $q = 5, 6, 7, 8$ have renormalization-group flows in 8, 12, 15, and 20 energies, respectively. These constitute very extensive

renormalization-group calculations.

The results are shown in Fig. 2.4. Direct comparison between different q is shown in Fig. 2.6, showing a striking evolution with respect to q.

2.5.3 Comparison with Potts results

The characteristic behavior is seen here as well. The curves are for $U_{k,k-m}$ for $k = 0,1,\ldots,q-1$ and $m = 0,1,\ldots$. Thus, m measures the angular difference $\theta_i - \theta_j = 2\pi m/q$ between the states of neighboring spins. For each m, the curves for different k coincide in the disordered high-temperature phase. In the low-temperature phase, for each m, the densities involving $k = 0$ and the densities involving $k > 0$ split under the spontaneous symmetry breaking favoring the state 0. The interface densities involving $k = 0$ exhibit reentrance as temperature is lowered in the ordered phase, first increasing in value and then receding to zero at zero temperature.

2.6 Magnetizations and Infinite-q Limit

The magnetizations M are directly obtained from the nearest-neighbor densities. For the Potts models,

$$M = \langle \delta(s_i, a) \rangle = \sum_{m=0,n=0}^{q-1,q-1} U(mn)\delta(m,a). \tag{2.18}$$

For the clock models,

$$M = \langle \cos(\theta_i) \rangle = \sum_{m=0,n=0}^{q-1,q-1} U(mn)\cos(2\pi m/q). \tag{2.19}$$

These equations are obtained by including a magnetic field term, H, (to be taken to zero after differentiating) in the $E(mn)$, differentiating $\ln(Z)$ with respect to the magnetic field, and using the chain rule with $E(mn)$ as intermediary.

The results for the magnetizations and the critical temperatures are given in Figs. 2.2 and 2.7 and Table 2.1. It should be noted that these results are exact for the $d = 3$ hierarchical lattice. They are approximate for the cubic lattice. Specifically, by allowing effective vacancies to be generated by the renormalization-group transformation, the Potts model

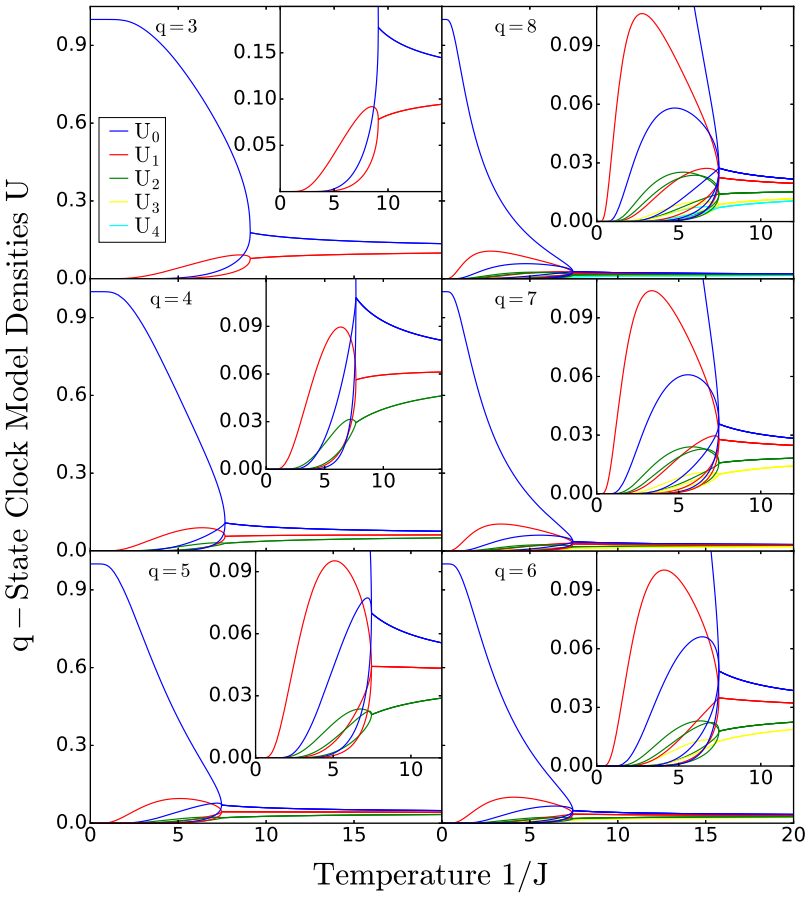


Figure 2.4: The calculated nearest-neighbor densities of the q-state clock models in $d = 3$. The curves are for $U_m \equiv U_{k,k-m}$, for $k = 0, 1, \ldots, q-1$ and $m = 0, 1, \ldots$, from the top down in each figure panel. Thus, m measures the angular difference $\theta_i - \theta_j = 2\pi m/q$ between the states of neighboring spins. For each m, the curves for different k coincide in the disordered high-temperature phase. In the low-temperature phase, for each m, the densities involving $k = 0$ and the densities involving $k > 0$ split under the symmetry breaking favoring the state 0. The interface densities involving $k = 0$ exhibit reentrance as temperature is lowered in the ordered phase, first increasing in value and then receding to zero at zero temperature.

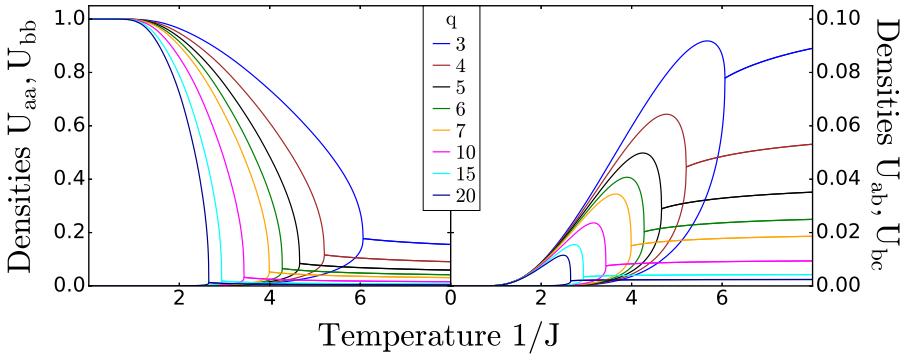


Figure 2.5: Comparison with respect to the number of states $q = 3,4,5,6,7,10,15,20$, from the top down in each panel, of the nearest-neighbor densities of the Potts models in $d = 3$. The right panel shows the curves for neighboring unlike states U_{ab} and U_{bc}, which coincide in the disordered high-temperature phase and split in the symmetry-broken low-temperature phase. The interface density U_{ab} exhibits reentrance as temperature is lowered in the ordered phase, first increasing in value and then receding to zero at zero temperature. This reentrance is pronounced in the low-q states and decreases for high q. The left panel shows the curves for the like-state neighbors U_{aa} and U_{bb}, which also coincide in the disordered high-temperature phase and split in the low-temperature phase where symmetry is spontaneously broken in favor of state a.

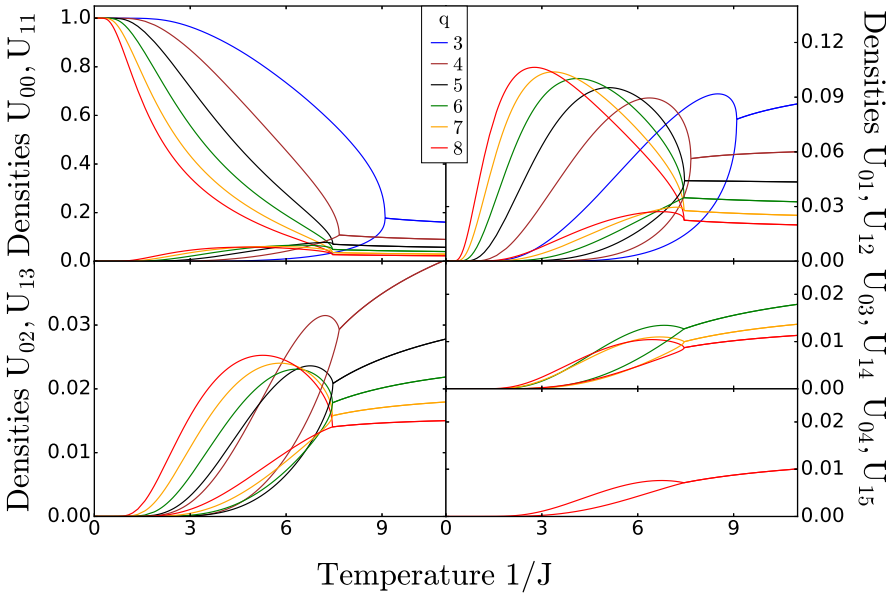


Figure 2.6: Comparison with respect to the number of states $q = 3,4,5,6,7,8$ of the nearest-neighbor densities of the clock models, $U_m \equiv U_{k,k-m}$ for $k = 0,1$ and $m = 0,1,\ldots$, shown in decreasing q on the high-temperature side in each panel. m measures the angular difference $\theta_i - \theta_j = 2\pi m/q$ between neighboring spins.

transition correctly becomes first order for $q > 2$ (Berker et al., 1978; Nienhuis et al., 1979; Andelman and Berker, 1981).

It is of interest to see the magnetization curves for the clock models in Fig. 2.7 settle to their $q \to \infty$ value for as low as $q = 5$. This is of course reflected in the essentially constant value of the clock critical temperatures as q is increased.

Such is not the case for the Potts models. Directly writing down the recursion relation for J in Eq. (2.1),

$$J' = \ln\left[e^{2b^{d-1}J} + (q-1)\right] - \ln\left[2e^{b^{d-1}J} + (q-2)\right], \tag{2.20}$$

setting the fixed point condition $J' = J = J_c$, and expanding for large J and q, we find the critical temperatures

$$J_c^{-1} = 7/\ln(q). \tag{2.21}$$

This curve is plotted as a dashed curve in Fig. 2.2 and gives a good fit even for finite q. As $q \to \infty$, the critical temperature goes to zero.

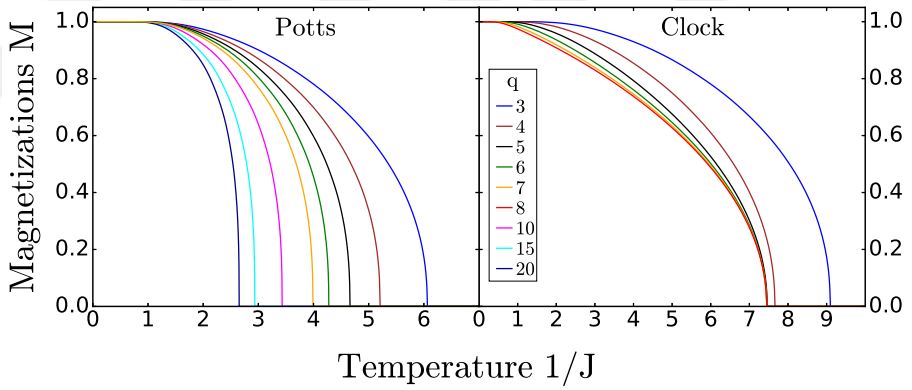


Figure 2.7: Calculated magnetizations of the Potts and clock models as a function of temperature J^{-1} in $d = 3$ for different values of the number of states q. It is noteworthy that, in the clock models, the magnetization quickly (at as low as $q = 5$) settles to its $q = \infty$ (which is the XY model) value along the entire temperature range of the low-temperature ordered phase, not only at the value of J_c^{-1} as was seen above in Fig. 2.2 and Table 2.1.

There is a physical explanation for the contrast between the Potts and clock models. In the Potts models, the states neighboring $s_i = a$ do not contribute to the magnetization and they are entropically favored as q is increased. (In fact, in the permutationally symmetric Potts models, the concept of "neighboring" state has no meaning: every state is equally positioned with respect to a chosen state.) By contrast, in the clock models, the states neighboring $\theta_i = 0$ give almost a full contribution, namely $\cos(2\pi n_i/q)$ to the magnetiza-

tion, where $n_i \ll q$ for large q. Thus, in all spatial dimensions d, the critical temperature for Potts models should go to zero inverse logarithmically as $q \to \infty$.

Table 2.1: Calculated critical temperatures of the q-state Potts and clock models. The clock-model results have been found numerically by doing the sums in the renormalization-group decimation over a very large number of states, up to $q = 360$.

q	Potts J_c^{-1}	Clock J_c^{-1}
3	6.062	9.093
4	5.206	7.661
5	4.660	7.416
6	4.277	7.395
7	3.990	7.391
8	3.764	7.388
10	3.431	7.384
15	2.936	7.381
20	2.652	7.379
360	1.278	7.377
∞	$7/\ln(q)$	7.377

2.7 Conclusion

In this chapter, we have calculated all of the bond-state densities of the q-state Potts and clock models in $d = 3$. This was done for all q for the Potts models by reducing the recursion relations to four, using symmetries, modulo singling out one state for possible spontaneous symmetry breaking, which happens for both models. Although the number of recursion relations in clock models can be reduced by symmetry, their number grows, for example to 20 different energies for our treated eight-state clock model. However, we have presented a robust method that would make the calculation for any number of states q feasible.

A reentrant behavior of all of the symmetry-broken interface densities was found for both models, and was physically explained. A surprising saturation with increasing q was found in the clock models, but not in the Potts models. We also found qualitatively different phase transition behaviors in the $q \to \infty$ limit, which was physically explained by entropy and alignment arguments.

The chapter has established the technical foundation for the thesis: transfer-matrix formalism, density recursion relations, symmetry reduction, and eigenvector analysis at sinks. In the language of Chapter 1, the Potts and clock models represent "simpler" systems whose

RG flows converge to isolated fixed points with two-phase diagrams. Yet even these simple systems exhibit interface density reentrance, demonstrating that coarse-graining reveals emergent behavior invisible to microscopic analysis. Subsequent chapters progressively add complexity generators to these baseline models.

3. UNIVERSAL SPIN-GLASS CHAOS

3.1 Introduction

3.1.1 Generalized Ising system and frustration

Since the blossoming days of modern phase transitions and critical phenomena, theoretical insight has been obtained from model spin systems studied systematically as a function of the number of local states, namely for all s (Domb and Sykes, 1962; Domb and Green, 1974; Vandyke and Camp, 1974; Camp and Vandyke, 1975; Berker, 1975; Camp et al., 1976; Nienhuis et al., 1979; Jensen et al., 1996; Sardar and Chakraborty, 1997; Yokota, 2002; Butera and Comi, 2002a,b; Butera et al., 2003; Butera and Comi, 2004; Rojas et al., 2007). Indeed, some of the authors in these references are the founders of the field. However, the same systematic studies have not been done on the complex ordering systems of current interest, such as in the presence of frozen disorder, presumably due to calculational difficulties, now surmountable by global renormalization group, as shown below.

3.1.2 Chaos under scale transformation

Frozen disorder of the interactions introduces many qualitatively and quantitatively new effects to statistical mechanical systems, such as the immediate (i.e., with infinitesimal disorder) conversion of first-order phase transitions into second-order phase transitions (Aizenman and Wehr, 1989, 1990; Hui and Berker, 1989a,b) or the creation of an entirely new phase such as the spin-glass phase (Edwards and Anderson, 1975). The latter occurs under frozen (quenched) competing interactions causing local minimum-energy degeneracies dubbed frustration (Toulouse, 1977). The signature of the spin-glass phase is the appearance of a chaotic sequence of interactions (McKay et al., 1982a,b; Berker and McKay, 1984; Hartford and McKay, 1991; Zhu et al., 2016; Wang et al., 2016; Fernandez et al., 2016; Billoire et al., 2018; Eldan, 2020; Wang et al., 2018; Baity-Jesi et al., 2021) under the successive scale changes of a renormalization-group transformation. This trans-

lates to a chaotic spin-spin correlation function, as function of distance, at a given scale. This chaotic behavior signifies that a small change at the microscopic level in the coupling constant (J) or temperature ($1/J$), or randomness (p) in the system causes major changes in the correlation function between two distant spins (Aral and Berker, 2009).

The spin-glass phase and its rescaling chaos appears with the introduction, by rewiring, of infinitesimal frustration to the Mattis phase (Mattis, 1976) obtained by random local spin redefinitions (gauge transformations) in the usual ferromagnetic or antiferromagnetic phase (Ilker and Berker, 2014a). On the other hand, strong chaos, signaled by a large Lyapunov exponent, of the spin-glass phase in fully frustrated systems continues (Demirtaş et al., 2015) until the lower-critical dimension $d_c \simeq 2.5$ of the spin-glass phase (Demirtaş et al., 2015; Franz et al., 1994; Boettcher, 2005; Maiorano and Parisi, 2018; Amoruso et al., 2003; Bouchaud et al., 2003; Maiorano and Parisi, 2018). Thus both gradual (Ilker and Berker, 2014a) or abrupt (Demirtaş et al., 2015) onsets of chaos are seen.

3.1.3 The question of universality

Most spin-glass studies have been on the classical spin $s = 1/2$ Ising model, where locally $s_i = \pm 1$ (Morgenstern and Binder, 1979; Grinstein et al., 1976). Spin-glass studies have also been done on q-state clock models and their continuum limit the XY model (Ilker and Berker, 2013, 2014b), chiral (helical (Kardar and Berker, 1982)) Potts and clock models, in fact leading to chiral spin-glass Potts (Çağlar and Berker, 2016) and clock (Çağlar and Berker, 2017a,b) phases, and quantum Heisenberg models (Kaplan and Berker, 2008). The position-space renormalization-group method appears to be a method suited for such studies, where the rescaling behavior of the distribution of the quenched random interactions is followed and analyzed (Andelman and Berker, 1984). This is best effected (Fig. 3.1) by use of the Migdal-Kadanoff approximation (Migdal, 1975; Kadanoff, 1976) or, equivalently, the exact recursion of a hierarchical lattice (Berker and Ostlund, 1979; Artun and Berker, 2020; Griffiths and Kaufman, 1982; Kaufman and Griffiths, 1984). In the current work, we quantitatively and globally study, in spatial dimension $d = 3$, the Ising spin glass for all spins $s = 1/2, 1, 3/2, 2, 5/2, \ldots$ to the limiting value $s \to \infty$, obtaining the global s-sequence phase diagram (Fig. 3.2) and chaotic behavior.

This chapter establishes the first major result of the thesis: frustration generates complexity through chaotic renormalization-group flows, and this complexity is universal with respect to microscopic details. Specifically, we demonstrate that the Lyapunov exponent $\lambda = 1.93$ characterizing the strength of spin-glass chaos is identical for all spin values

$s = 1/2, 1, 3/2, \ldots, \infty$. This universality is striking: despite radical differences in the microscopic Hilbert space dimension (from 2 states for $s = 1/2$ to a continuum for $s \to \infty$), the emergent chaotic behavior is quantitatively identical.

3.2 Model

The spin-s Ising model is defined by the Hamiltonian

$$-\beta\mathscr{H} = \sum_{\langle ij \rangle} J_{ij}(s_i/s)(s_j/s), \tag{3.1}$$

where $\beta = 1/kT$, at each site i of the lattice the spin $s_i = 0, \pm 1/2, \pm 1, \pm 3/2, \ldots, \pm s$, and $\langle ij \rangle$ denotes summation over all nearest-neighbor site pairs. The division by s is done to conserve the energy scale across the different spin-s models and thereby make meaningful temperature comparisons between them. Note that, for $s = 1/2$, this formalism yields the much studied $s_i/s = \pm 1$ case.

The bond J_{ij} is ferromagnetic $+J > 0$ or antiferromagnetic $-J$ with respective probabilities $1 - p$ and p. Under renormalization-group transformation, this "double-delta" distribution of interactions is not conserved. A more complicated distribution of interactions ensues and is kept track of, as explained below.

3.3 Renormalization-Group Method

3.3.1 Transfer matrix for general spin

Under renormalization group, for $s > 1/2$, the Hamiltonian does not conserve its form in Eq. (3.1). Thus, for any s, the Hamiltonian is most generally expressed as

$$-\beta\mathscr{H} = \sum_{\langle ij \rangle} E_{ij}(s_i, s_j), \tag{3.2}$$

where $E_{ij}(s_i, s_j)$ is the dimensionless interaction between nearest-neighbor spins, starting out as in Eq. (3.1) as $J_{ij}(s_i/s)(s_j/s)$ and generalizing to a $2s \times 2s$ or $(2s+1) \times (2s+1)$ matrix under renormalization group. With no loss of generality, for each $\langle ij \rangle$, the same constant is subtracted from all terms $E(s_i, s_j)$, so that the largest energy $E(s_i, s_j)_{\max}$ of the spin-spin interaction is zero [and all other $E(s_i, s_j) < 0$]. This formulation makes it

possible to follow global renormalization-group trajectories, necessary for the calculation of phase boundaries, Lyapunov exponent, and runaway exponent, without running into numerical overflow problems.

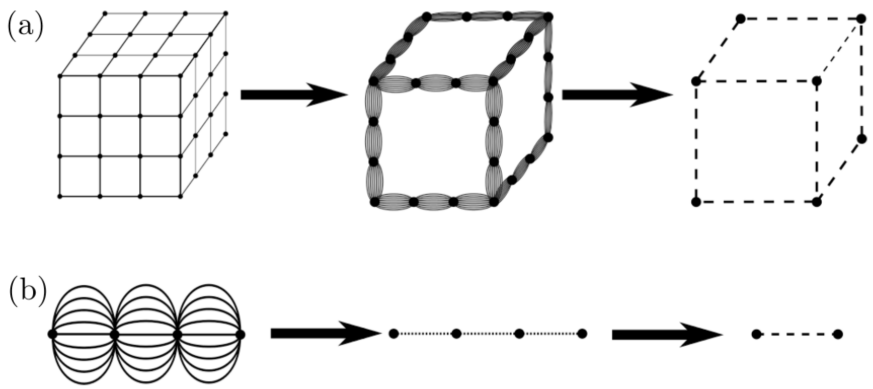


Figure 3.1: (a) Migdal-Kadanoff approximate renormalization-group transformation for the $d = 3$ cubic lattice with the length-rescaling factor of $b = 3$. In this intuitive approximation, bond moving is followed by decimation. (b) Exact renormalization-group transformation of the $d = 3$, $b = 3$ hierarchical lattice for which the Migdal-Kadanoff renormalization-group recursion relations are exact. The construction of a hierarchical lattice proceeds in the opposite direction of its renormalization-group solution.

As the local renormalization-group transformation, the Migdal-Kadanoff approximate transformation (Migdal, 1975; Kadanoff, 1976; Angelini and Biroli, 2017) and, equivalently, the exact transformation for the $d = 3$ hierarchical lattice (Berker and Ostlund, 1979; Griffiths and Kaufman, 1982; Kaufman and Griffiths, 1984) is used (Fig. 3.1). Recent works using exactly soluble hierarchical models are in Refs. (Myshlyavtsev et al., 2020; Derevyagin et al., 2020; Chang et al., 2020; Monthus, 2020; Ruiz, 2018; Rocha-Neto et al., 2018; Ma et al., 2018; Boettcher and Li, 2018). The length rescaling factor of $b = 3$ is used to preserve under renormalization group the ferromagnetic-antiferromagnetic symmetry of the system. This local transformation consists in bond moving followed by decimation, with the above-mentioned subtraction after each local bond moving and decimation, giving the local renormalized energies $E'(s_i, s_j) \leq 0$. In our notation, all renormalized quantities are designated by a prime.

3.3.2 Quenched disorder and distribution flows

The quenched randomness is included by keeping, as a distribution, 10,000 sets of the nearest-neighbor interaction energies $E(s_i, s_j)$. At the beginning of each renormalization-group trajectory, this distribution is formed from the double-delta distribution character-

ized by interactions $\pm J$ with probabilities p, $(1-p)$. Ten thousand local renormalization-group transformations determine each subsequent distribution as explained below.

The local renormalization-group transformation is simply expressed in terms of the transfer matrix $T(s_i, s_j) = e^{E(s_i,s_j)}$: Bond moving consists of multiplying elements at the same position of $b^{d-1} = 9$ transfer matrices randomly chosen from the distribution,

$$\tilde{T}(s_i, s_j) = \prod_{k=1}^{9} T_k(s_i, s_j), \tag{3.3}$$

so that a distribution of 10,000 bond-moved transfer matrices is generated. Decimation consists of matrix multiplication of three randomly chosen bond-moved transfer matrices,

$$\mathbf{T}' = \tilde{\mathbf{T}}_1 \cdot \tilde{\mathbf{T}}_2 \cdot \tilde{\mathbf{T}}_3, \tag{3.4}$$

so that a distribution of 10,000 renormalized transfer matrices is generated.

3.3.3 Phase identification from asymptotic flows

Phases are determined by following trajectories to their asymptotic limit:

- *Ferromagnetic phase*: The asymptotic limit transfer matrices of trajectories starting in the ferromagnetic phase all have 1 in the corner diagonals and 0 at all other positions.

- *Antiferromagnetic phase*: The asymptotic limit transfer matrices of trajectories starting in the antiferromagnetic phase all have 1 in the corner antidiagonals and 0 at all other positions.

- *Spin-glass phase*: The asymptotic limit transfer matrices of trajectories starting in the spin-glass phase all have 1 in the corner diagonals $(s_i = s, s_j = s)$ and $(s_i = -s, s_j = -s)$ *or* in the corner antidiagonals $(s_i = s, s_j = -s)$ and $(s_i = -s, s_j = s)$, and 0 at all other positions.

- *Disordered phase*: The asymptotic limit transfer matrices of trajectories starting in the disordered phase all have 1 at all positions.

We use $(s, s-1, s-2, \ldots, -s+2, -s+1, -s)$ for the order of the rows and columns in the

matrix $E(s_i, s_j)$. Phase diagrams are obtained by numerically determining the boundaries, in the unrenormalized system, of these asymptotic flows. Thus, to numerically obtain the phase diagram, we determine the asymptotic limit, under repeated renormalization-group transformations, of the distribution of transfer matrices. These asymptotic limits for the ferromagnetic, antiferromagnetic, spin-glass, and disordered phases are distinct, as described here. The boundaries between different asymptotic limits, as a function of starting (unrenormalized) J and p, yield the phase diagram numerically, as seen in Fig. 3.2 for different values of the spin s.

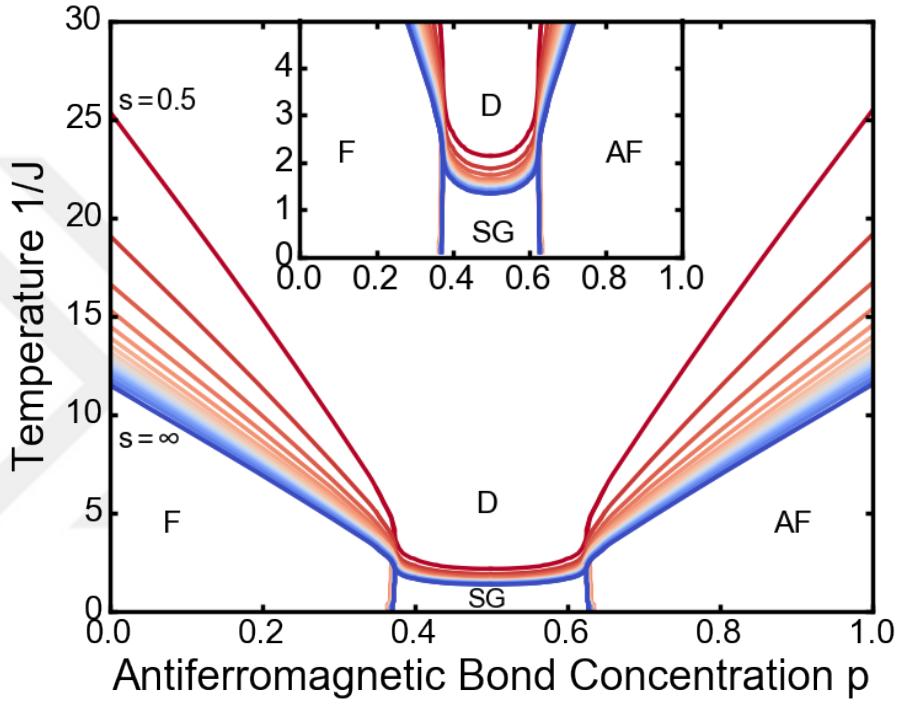


Figure 3.2: Calculated phase diagrams of the spin-s Ising spin glasses in $d = 3$. From top to bottom, $s = 1/2, 1, 3/2, 2, 5/2, 3, \ldots$ to $s \to \infty$. There is an accumulation, from above, of the phase diagrams at the lowermost, but still at finite temperature, phase diagram of the continuum limit $s \to \infty$. The phase diagrams shown here are the results of our numerical calculations and are accurate to the thickness of the lines in this figure. F = ferromagnetic, AF = antiferromagnetic, SG = spin glass, D = disordered.

3.4 Phase Diagrams and Critical Temperatures

3.4.1 Global phase structure

In this and the next sections, we present the numerical results on spin-s Ising spin-glass systems, calculated exactly on a $d = 3$ hierarchical model and, simultaneously, by the Migdal-Kadanoff approximation on the cubic lattice.

The calculated phase diagrams of the spin-s Ising spin glasses in $d = 3$ are shown in Fig. 3.2. From top to bottom, the phase diagrams are for spin $s = 1/2, 1, 3/2, 2, 5/2, 3, \ldots$ to $s \to \infty$. There is an accumulation, from above, of the phase diagrams at the lowermost, but still at finite temperature, phase diagram of the continuum limit $s \to \infty$. The phase diagrams shown in Fig. 3.2 are the results of our numerical calculations and are accurate to the thickness of the lines in this figure.

3.4.2 Critical temperatures as functions of spin magnitude

The calculated ferromagnetic (at $p = 0$) and spin glass (at $p = 0.5$) phase transition temperatures as a function of spin s are given in Fig. 3.3. With increasing s, both transition temperatures saturate around $s \simeq 8$. A similar behavior was found in q-state clock models saturating at the continuum XY model transition temperature. The critical temperatures in Fig. 3.3 are the results of our numerical calculations and are accurate to the size of the data points in this figure.

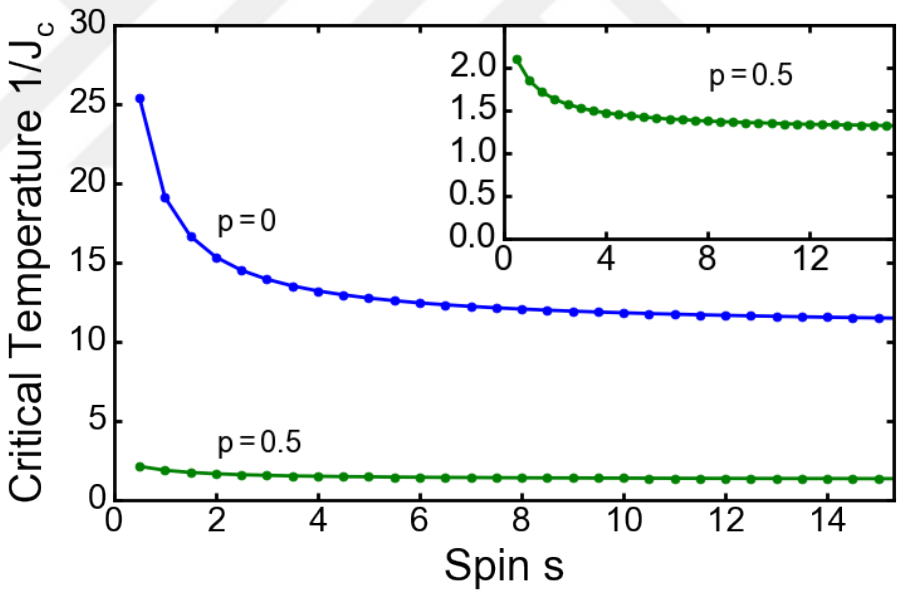


Figure 3.3: The calculated ferromagnetic (at $p = 0$) and spin-glass (at $p = 0.5$) phase transition temperatures as a function of spin value s. Note that, with increasing s, both transition temperatures saturate around $s \simeq 8$. The critical temperatures in this figure are the results of our numerical calculations and are accurate to the size of the data points in this figure.

3.4.3 Percolative nature of phase boundaries

A striking feature of the phase diagrams in Fig. 3.2 is that the ferromagnetic-spin-glass and spin-glass-antiferromagnetic phase transitions occur, along their whole length, respectively at $p_t = 0.37$ and 0.63. These transition concentrations are unaffected by s, confirming the percolative nature of this phase transition. The spin-glass phase exists in a symmetric window around $p = 0.5$ (the maximally frustrated point), and this window is determined purely by the connectivity of ferromagnetic versus antiferromagnetic bonds, independent of the microscopic spin structure.

3.5 Spin-Glass Chaos

3.5.1 Lyapunov exponents

For all spin s, the renormalization-group trajectories starting within the spin-glass phase are asymptotically chaotic, as seen in Fig. 3.4, where the consecutively renormalized (combining with neighboring interactions) values at a given location, meaning $\langle ij \rangle$ then the renormalized $\langle i'j' \rangle$ that includes $\langle ij \rangle$, etc., are followed. For the interaction K_{ij}, we have used the difference between the largest value (which is zero by construction) and the lowest value in $E(s_i, s_j)$. $\overline{K}$ is the average of this interaction over the entire distribution at the given renormalization-group step. Since the dimensionless interaction K is proportional to inverse temperature, as seen from our Eq. (3.1), chaotic K means chaotic temperature.

The chaotic behavior is strong, as measured by the Lyapunov exponent (Grinstein et al., 1976; Collet and Eckmann, 1980; Hilborn, 2003)

$$\lambda = \lim_{n\to\infty} \frac{1}{n} \sum_{k=0}^{n-1} \ln \left| \frac{dx_{k+1}}{dx_k} \right|, \tag{3.5}$$

where $x_k = K_{ij}/\overline{K}$ at step k of the renormalization-group trajectory. We obtain the Lyapunov exponents by numerically calculating the logarithmic sum in Eq. (3.5), eliminating the first 100 renormalization-group steps as crossover from initial conditions to asymptotic behavior and then using the next 1500 steps.

This calculation, for all spins s, yields $\lambda = 1.93$, numerically correct to the three significant figures shown for this hierarchical lattice construction. The universality of this

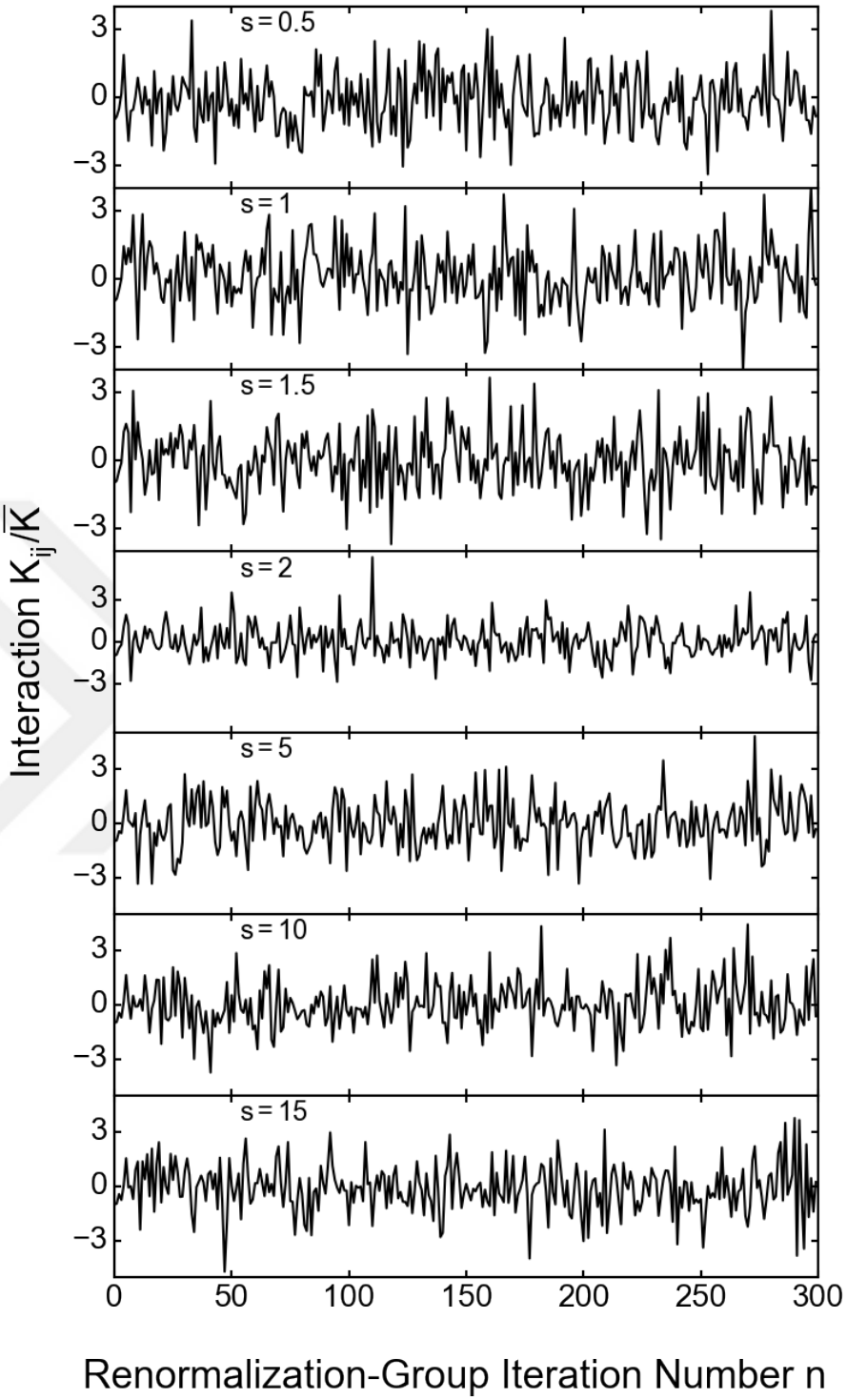


Figure 3.4: The chaotic renormalization-group trajectory of the interaction K_{ij} at a given location $\langle ij \rangle$, for various spin s values, at spatial dimension $d = 3$. Note the strong chaotic behavior for all s, as also reflected by the calculated Lyapunov exponent $\lambda = 1.93$ for all s. The calculated runaway exponent is $y_R = 0.24$ for all s, showing simultaneous strong-chaos and strong-coupling behavior.

Lyapunov exponent across all spin values within the spin-s Ising family is remarkable: from the simplest $s = 1/2$ case with 2 states per site to the continuum $s \to \infty$ limit, the strength of chaos is identical.

We emphasize that this value characterizes spin-s Ising spin glasses on the specific $b = 3$, $d = 3$ hierarchical lattice. Different lattice constructions or different spin symmetries may yield different Lyapunov exponents. What is universal here is the independence of λ from spin magnitude within a given model family.

3.5.2 Runaway exponents and unsaturated order

In addition to strong chaos, the renormalization-group trajectories show asymptotic strong-coupling behavior,

$$\overline{K'} = b^{y_R}\overline{K}, \tag{3.6}$$

where $y_R > 0$ is the runaway exponent (Demirtaş et al., 2015). Again using 1500 RG steps after discarding 100 steps, we find $y_R = 0.24$ for all spins s, numerically correct to the two shown significant figures. We thus find that y_R, too, along with λ, are universal with respect to spin s.

Note that here is a "weak" strong-coupling behavior, as the stronger runaway exponent of the ferromagnetic and antiferromagnetic phases is $y_R = d - 1 = 2$. In fact, the runaway exponent y_R occurs, under renormalization group, in all ordered phases and is $y_R = d - 1$ in all conventionally ordered phases (Çağlar and Berker, 2017b). However, in the spin-glass phase, since deep into this phase where the renormalization-group flows lead (at the sink of this phase), we do not have the rescaling of compactly ordered renormalization-group cells (McKay et al., 1982a), $y_R < d - 1$, as also seen in Refs. (Demirtaş et al., 2015; Atalay and Berker, 2018), where the runaway exponents y_R have been studied in detail.

The small value $y_R = 0.24 < d - 1 = 2$ indicates unsaturated order: the spin-glass phase, while ordered in the sense of having long-range correlations detected through the Edwards-Anderson order parameter, does not achieve the compact domain structure of conventional ferromagnets. The interfaces between differently oriented regions remain rough at all scales, contributing to the chaotic rescaling behavior.

3.6 Conclusion

We have calculated the global spin-s sequence of phase diagrams for all spins $s = 1/2, 1, 3/2, 2, 5/2, 3, \ldots, s \to \infty$ for the Ising spin-glass system in spatial dimension $d = 3$. The phase diagrams, all with a finite-temperature spin-glass phase, for increasing spin s saturate to the limit value of $s \to \infty$. For all spins s, the spin-glass phase has renormalization-group trajectories that are chaotic, with calculated Lyapunov exponent $\lambda = 1.93$ and runaway exponent $y_R = 0.24$, thus simultaneously showing strong chaotic and "weak" strong-coupling behavior.

The results provide the first concrete demonstration of frustration producing complexity. The spin-glass phase is a new thermodynamic phase requiring frustration, with flows that never settle to a fixed point but wander chaotically on a strange attractor. The Lyapunov and runaway exponents are universal—independent of spin s—suggesting that chaos strength is determined by frustration geometry rather than microscopic details. The contrast with Chapter 2 is instructive: frustration transforms RG flow topology from simple (fixed points with $y_R = d - 1$) to complex (chaos with $\lambda = 1.93$ and $y_R = 0.24$).

4. EMERGENT NEMATIC PHASE

4.1 Introduction

4.1.1 Vector spins and frustration

Spin-glass systems have an inherent quantifiable chaos under scale change (McKay et al., 1982a,b; Berker and McKay, 1984; McKay and Berker, 1984) and thus provide a universal classification and clustering scheme for complex phenomena (Artun et al., 2023a), as well as rich ordering phenomena such as spin-glass sponge ordering (Pektaş et al., 2023). Spin-glass studies have been done overwhelmingly with Ising $s_i = \pm 1$ spins. However, a recent study (Tunca and Berker, 2023) with classical Heisenberg spins $\vec{s}_i$ that can continuously point in 4π steradians found, instead of spin-glass order, nematic order, meaning a liquid-crystal phase in a dirty magnet. In the current study, we continue in this direction, studying n-component cubic-spin spin glasses. Cubic spins can be considered as discretized and systematically extended versions of Heisenberg spins.

4.1.2 Cubic spins as discretized Heisenberg spins

The n-component cubic spin is a vector spin that can point along any of the $2n$ Cartesian directions: $\pm\hat{x}_1, \pm\hat{x}_2, \ldots, \pm\hat{x}_n$. For $n = 1$, this reduces to the Ising model with $s_i = \pm 1$. For $n = 3$, the six states are $\pm\hat{x}, \pm\hat{y}, \pm\hat{z}$—a discretized version of the three-dimensional Heisenberg spin.

The n-component cubic-spin spin-glass system is defined by the usual Hamiltonian, where $\beta = 1/kT$,

$$-\beta\mathscr{H} = \sum_{\langle ij \rangle} J_{ij}\vec{s}_i \cdot \vec{s}_j \equiv \sum_{\langle ij \rangle} -\beta H_{ij}, \tag{4.1}$$

but where $\vec{s}_i$ can be in $2n$ different states $\pm\hat{u}$ at each site i, $\hat{u}$ being a unit Cartesian vector. The sum is over nearest-neighbor pairs of sites $\langle ij \rangle$. The interaction J_{ij} is ferromagnetic $+J > 0$ or antiferromagnetic $-J$ with probabilities $1 - p$ and p, respectively.

The cubic-spin spin-glass system studied in this work is of particular interest, because it generalizes the much studied single-component simple spin Ising model to a realistic vector-spin system with n vector components. It is a rich system, since each of the n-component systems has phase transition behavior in a different universality class. As seen below, it is readily treatable by renormalization-group theory, yielding the complex novel result of a band of liquid-crystal phase above the spin-glass phase. This means a liquid-crystal phase occurring in a dirty magnet.

This chapter demonstrates a remarkable consequence of combining frustration with increasing spin dimensionality: the emergence of a nematic phase that exists in neither the pure frustrated system (low n) nor the unfrustrated vector-spin system. The nematic phase exhibits orientational order without directional order—spins align along one Cartesian axis but with no preference between positive and negative directions.

4.2 Model and Method

The cubic spin interpolates between the Ising model ($n = 1$) and the classical Heisenberg model ($n \to \infty$). The discrete nature of the cubic spin makes it computationally tractable while retaining the essential physics of vector spins with multiple components.

The transformation is best implemented algebraically by writing the exponentiated nearest-neighbor Hamiltonian, namely the transfer matrix between two neighboring sites:

$$\mathbf{T}_{ij} \equiv e^{-\beta H_{ij}} = e^{J\vec{s}_i \cdot \vec{s}_j}. \tag{4.2}$$

For $n = 3$ components, this becomes a 6×6 matrix:

$$\mathbf{T}_{ij} = \begin{pmatrix} e^J & e^{-J} & 1 & 1 & 1 & 1 \\ e^{-J} & e^J & 1 & 1 & 1 & 1 \\ 1 & 1 & e^J & e^{-J} & 1 & 1 \\ 1 & 1 & e^{-J} & e^J & 1 & 1 \\ 1 & 1 & 1 & 1 & e^J & e^{-J} \\ 1 & 1 & 1 & 1 & e^{-J} & e^J \end{pmatrix}, \tag{4.3}$$

where the consecutive states are plus and minus directions of the sequence of Cartesian unit vectors $\hat{u}$. The generalization to arbitrary n is straightforward: the transfer matrix is

$2n \times 2n$, with 2×2 blocks of $(e^{J}, e^{-J}; e^{-J}, e^{J})$ along the diagonal (for parallel components) and 1's elsewhere (for orthogonal components).

The Migdal-Kadanoff approximation (Migdal, 1975; Kadanoff, 1976) and its algebraically equivalent, exactly solved hierarchical model (Berker and McKay, 1984; Berker and Ostlund, 1979; Griffiths and Kaufman, 1982; Kaufman and Griffiths, 1984) has been described in previous chapters. Operationally, this renormalization-group transformation consists in decimating inside b bonds in series and then adding b^{d-1} decimated bonds in parallel, where b is the length-rescaling factor ($b = 3$ in this work). It is a very simply done, very effective, and most extensively used (Artun et al., 2023a; Clark and Lochridge, 2023; Kotorowicz and Kozitsky, 2022; Zhang et al., 2022; Jiang et al., 2021; Chio and Roeder, 2021; Myshlyavtsev et al., 2020; Derevyagin et al., 2020; Chang et al., 2020; Monthus, 2020; Sarıyer, 2019) renormalization-group transformation.

The decimation step consists in matrix-multiplying b transfer matrices:

$$\mathbf{T}^{(\mathrm{dec})} = \mathbf{T}_1 \cdot \mathbf{T}_2 \cdot \mathbf{T}_3. \tag{4.4}$$

The bond-moving step consists in taking, after decimation, the power of b^{d-1} of each element in the transfer matrix (or multiplying element-wise these b^{d-1} matrices corresponding to the decimated bonds):

$$T_{mn}^{\prime(\mathrm{final})} = \left[T_{mn}^{(\mathrm{dec})} \right]^{b^{d-1}}. \tag{4.5}$$

Here b is the length-rescaling factor of the renormalization-group transformation.

For quenched-random systems, as in the present work, starting with a large distribution (of 10,000 realizations in this work), a renormalized distribution is generated by randomly associating b^d nearest-neighbor terms, 10,000 times. This is the solution of an actual physical realization (Kraichnan, 1961; Flory, 1986; Kaufman, 2018; Lloyd and Oglesby, 1976). Following the renormalization-group trajectories of the distributions, the phases and phase boundaries are obtained. Thus, our analysis is done by analyzing the renormalization-group trajectories of 20,000 interactions, which is a gigantic calculation.

4.3 Phase Diagrams

4.3.1 Results for $n = 1, 2, 3$ components

Calculated phase diagrams are shown in Fig. 4.1, for the cubic-spin spin-glass systems in spatial dimension $d = 3$. The phase diagrams are for number of components $n = 1, 2, 3$, meaning $2n$ states.

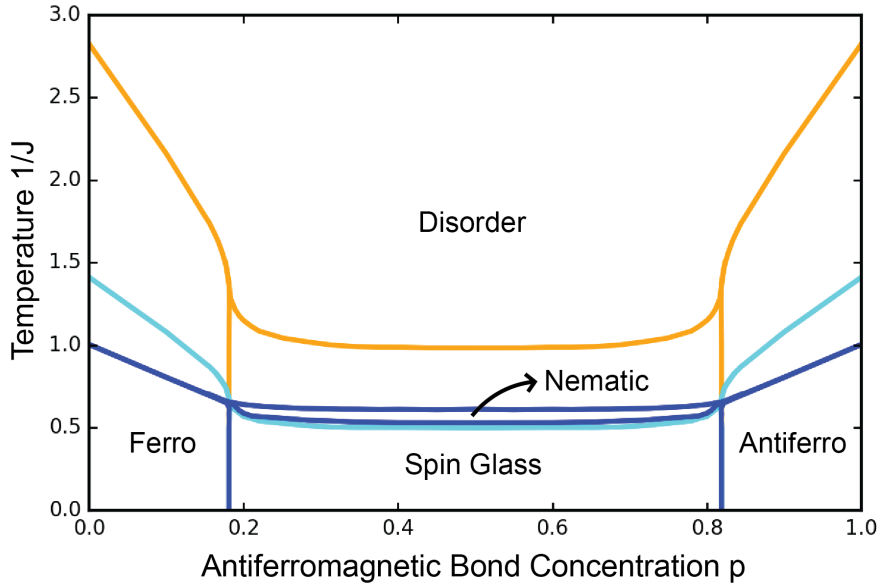


Figure 4.1: Calculated phase diagrams for the cubic-spin spin-glass systems in spatial dimension $d = 3$. The phase diagrams are, from top to bottom, for number of components $n = 1, 2, 3$, meaning $2n$ states. A nematic phase appears for $n = 3$, persisting for $n \geq 3$, as seen in Fig. 4.2.

4.3.2 The emergence of the nematic phase

A nematic phase appears for $n = 3$, persisting for $n \geq 3$, as seen in Fig. 4.2. The nematic phase completely intervenes between the low-temperature spin-glass phase and the high-temperature disordered phase.

For $n = 1$ (Ising) and $n = 2$, the phase diagram shows the familiar structure: ferromagnetic, antiferromagnetic, spin-glass, and disordered phases. The spin-glass phase directly borders the disordered phase at high temperature. However, for $n \geq 3$, a new phase—the nematic phase—emerges between the spin-glass and disordered phases.

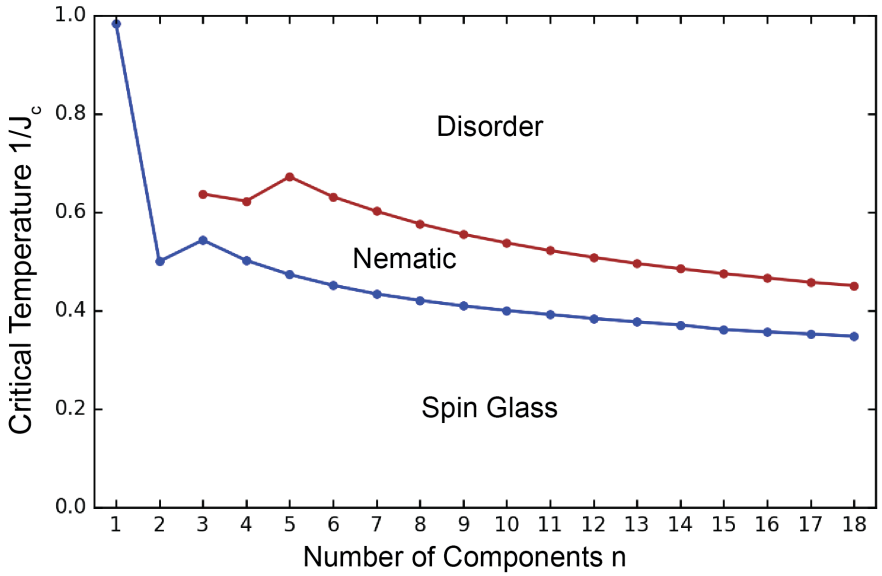


Figure 4.2: Nematic and spin-glass transition temperatures at the ferro-antiferro symmetric value of $p = 0.5$, as a function of the number n of spin components. It is seen that the nematic phase persists for $n \geq 3$.

4.3.3 Persistence for $n \geq 3$

The nematic and spin-glass transition temperatures at the ferro-antiferro symmetric value of $p = 0.5$ are shown in Fig. 4.2 as a function of the number n of spin components. Some features are noteworthy: The nematic phase persists for all $n \geq 3$, with a finite temperature window that initially grows and then stabilizes. The spin-glass transition temperature decreases monotonically with n, consistent with the increased entropy of the higher-dimensional spin space. The nematic-to-disorder transition temperature shows less variation, i.e., it is relatively stable, with n than the spin-glass transition temperature.

The sink values of the nematic phase show that the system aligns along one of the $\pm\hat{u}$, irrespective of the plus or minus direction, which is a nematic phase. This is a spin-space discretized version of the nematic phase in the classical Heisenberg spin-glass system, where the nematic alignment is along one of the continuum of 4π steradians, again irrespective of $\pm$ direction.

In the nematic phase, the frustration prevents the system from choosing between $+\hat{u}$ and $-\hat{u}$ (which would be ferromagnetic or antiferromagnetic order), but the thermal fluctuations are not strong enough to completely disorder the system. The compromise is to

select an *axis* rather than a *direction*—all spins align along the same Cartesian axis, but with random $\pm$ orientations. This is orientational order without directional order.

4.4 Renormalization-Group Sinks of the Phases

4.4.1 Ordered phase sinks

The renormalization-group sinks of the phases are shown in Fig. 4.3 for $n = 3$. The sink fixed-point values of the nearest-neighbor Hamiltonian exponentiated, namely the transfer matrix, Eq. (4.3), are shown. All points in a given phase flow, under renormalization-group, to its corresponding sink, which epitomizes the ordering of the phase.

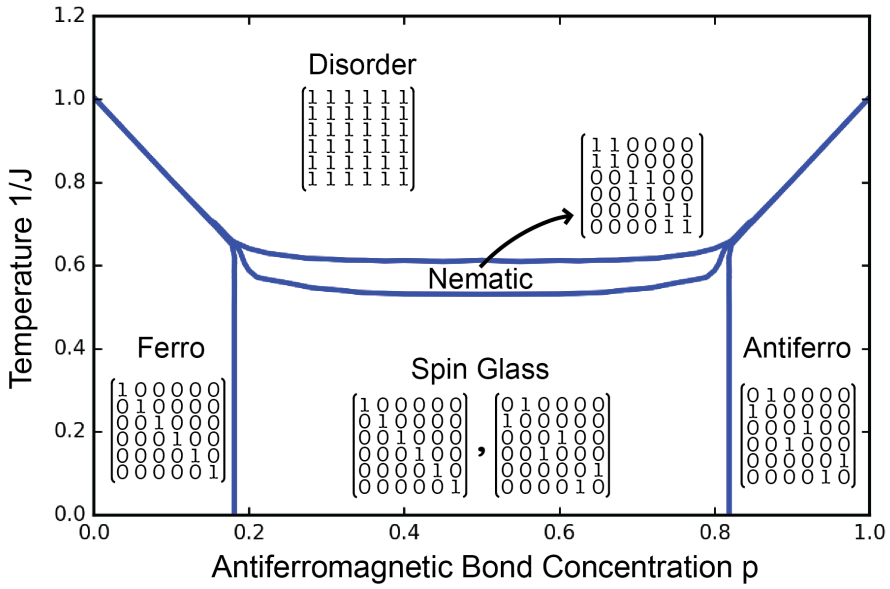


Figure 4.3: Renormalization-group sinks of the phases for $n = 3$. The sink fixed-point values of the nearest-neighbor Hamiltonian exponentiated, namely the transfer matrix, are shown. All points in a given phase flow, under renormalization-group, to its corresponding sink, which epitomizes the ordering of the phase. Except for the spin-glass phase, all phases flow to their respective single transfer matrix, shown in this figure. The spin-glass phase flows to a fixed distribution of diverging ferromagnetic and antiferromagnetic interactions, shown in Fig. 4.4. This fixed-point structure, underpinning the phase diagrams, occurs for all $n \geq 3$.

Disordered phase sink: All transfer matrix elements equal to 1 (equivalent to $J = 0$).

Ferromagnetic phase sink: The 2×2 blocks along the diagonal have the form with large positive J (favoring parallel alignment within each component), while off-diagonal blocks go to zero (orthogonal components become energetically prohibited).

Antiferromagnetic phase sink: Similar structure but with the sign of J reversed in the diagonal blocks.

4.4.2 The nematic sink structure

Nematic phase sink: The key feature is that only one 2×2 block remains active, with equal weights for both $+\hat{u}$ and $-\hat{u}$ states. This represents alignment along axis $\hat{u}$ without preference for direction.

4.4.3 Spin-glass fixed distribution

Spin-glass phase sink: Unlike the other phases, the spin-glass phase flows to a fixed *distribution* of diverging ferromagnetic and antiferromagnetic interactions, shown in Fig. 4.4. The distribution is symmetric around $J = 0$, reflecting the statistical equivalence of ferromagnetic and antiferromagnetic bonds in the frustrated system.

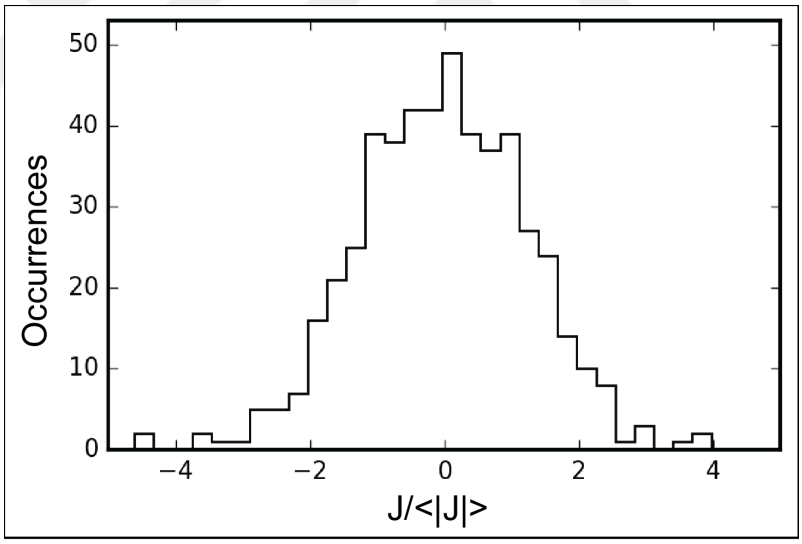


Figure 4.4: The fixed distribution of the sink of the spin-glass phase. The interaction J is extracted from the 2×2 transfer matrix of the spin component $\hat{u}$ that shows spin-glass order.

The renormalization-group trajectories starting in a given phase unmistakably reach their respective sinks within 8 renormalization-group iterations, including the case of the nematic phase. Renormalization-group trajectories starting close to a phase boundary spend iterations close to the unstable fixed point controlling the phase boundary, but reach the sink within 15 iterations for the accuracy of our calculation. The calculational uncertainty in our work is smaller than the thickness of all of the phase boundary lines in our

figures.

This fixed-point structure, underpinning the phase diagrams, occurs for all $n \geq 3$.

4.5 Spin-Glass Chaos

4.5.1 Lyapunov exponents and odd-even oscillations

The renormalization-group trajectories in the spin-glass phase are chaotic, as shown in Fig. 4.5. The strength of chaos under scale change (McKay et al., 1982a,b; Berker and McKay, 1984; McKay and Berker, 1984) is measured by the Lyapunov exponent (Collet and Eckmann, 1980; Hilborn, 2003),

$$\lambda = \lim_{n\to\infty} \frac{1}{n} \sum_{k=0}^{n-1} \ln \left| \frac{dx_{k+1}}{dx_k} \right|, \tag{4.6}$$

where $x_k = J_{ij}/\overline{J}$ at step k of the renormalization-group trajectory and $\overline{J}$ is the average of the absolute value of the interactions in the quenched random distribution. We calculate the Lyapunov exponents by discarding the first 100 renormalization-group steps (to eliminate crossover from initial conditions to asymptotic behavior) and then using the next 900 steps, shown in Fig. 4.5. The initial (J) values do not matter, as long as they are within the specified spin-glass phase.

As seen in Fig. 4.5, the calculated Lyapunov exponents show odd-even oscillations with respect to the number of cubic components n. Such oscillations have been seen previously, for example, as a function of spin s value, in critical temperatures of the Ising magnet (Berker, 1975).

The Lyapunov exponents for $n = 1$ to $n = 12$ are shown in Table 4.1.

The odd-even oscillation pattern is clear: odd values of n (particularly $n = 3,5,7,9,11$) show different Lyapunov exponents than even values, with the pattern being most pronounced for small n.

The odd-even oscillations arise from the different symmetry properties of the transfer matrix for odd versus even numbers of components. For odd n, there is no way to parti-

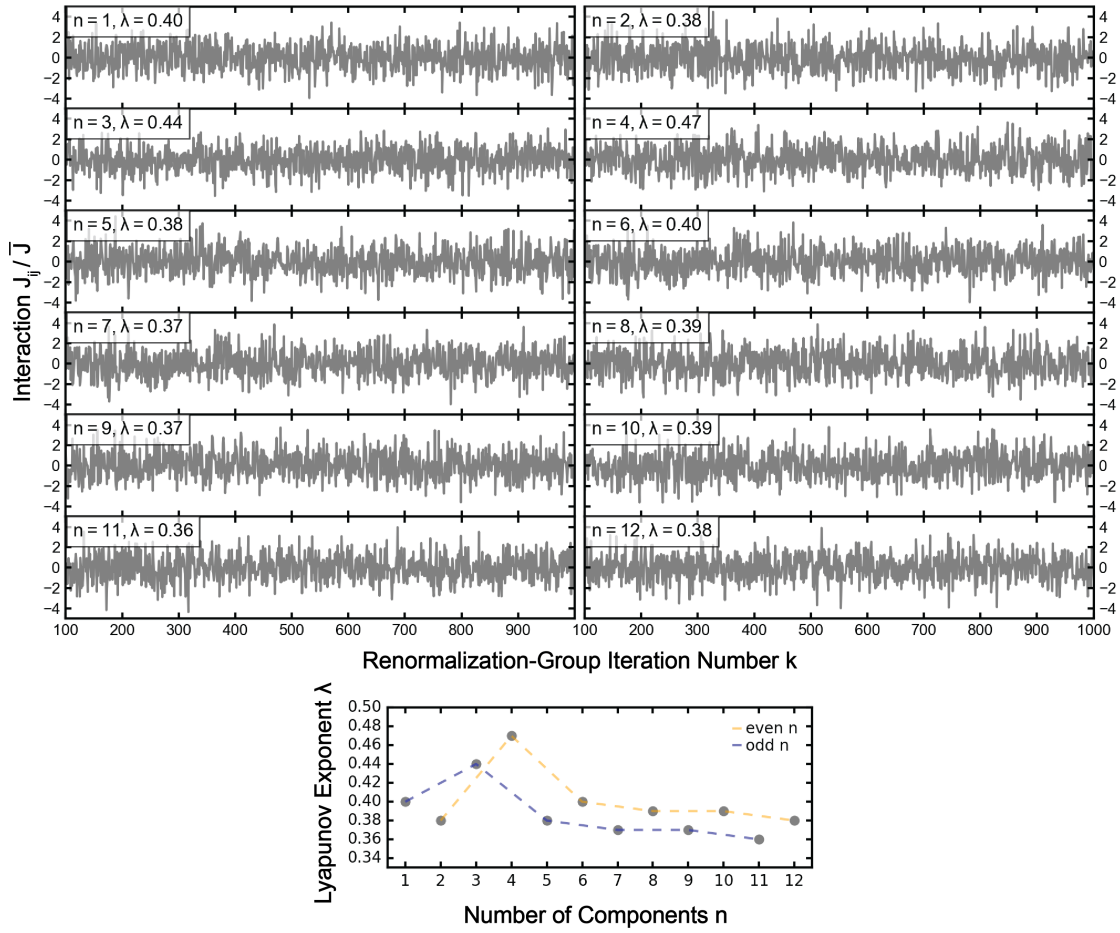


Figure 4.5: Chaotic renormalization-group trajectories of the spin-glass phases and their Lyapunov exponents. The Lyapunov exponents show odd-even oscillations with respect to the number of cubic components n.

Table 4.1: Lyapunov exponents λ for the cubic-spin spin-glass system as a function of the number of components n.

n	λ	n	λ
1	0.40	7	0.37
2	0.38	8	0.39
3	0.44	9	0.37
4	0.47	10	0.39
5	0.38	11	0.36
6	0.40	12	0.38

tion the components into equivalent pairs, leading to a different structure of the chaotic attractor.

4.5.2 Comparison with Ising spin glasses

In addition to chaos, the renormalization-group trajectories show asymptotic strong-coupling behavior (Demirtaş et al., 2015),

$$\overline{J}' = b^{y_R}\overline{J}, \tag{4.7}$$

where $y_R > 0$ is the strong-coupling runaway exponent (Demirtaş et al., 2015). Again using 900 renormalization-group steps after discarding 100 steps, we calculated the runaway exponent and find the same value of $y_R = 0.24$ for all n.

The fact that y_R is much less than $d-1=2$ shows that this spin-glass order is very unsaturated order. In the compact (saturating) ordering of systems without quenched randomness, $y_R = d-1$ reflects the energy of the smooth interface between oppositely aligned renormalization-group cells (Berker and Wortis, 1976). The universal value $y_R = 0.24$—identical to that found in Chapter 3 for spin-s Ising spin glasses—confirms that unsaturated order is a robust characteristic of spin-glass phases regardless of the microscopic spin structure.

4.6 Physical Interpretation: Liquid Crystal Order in Dirty Magnets

This chapter demonstrates that frustration interacts with spin dimensionality to produce emergent complexity that cannot be anticipated from either ingredient alone:

1. Ising spin glass ($n = 1$): Frustration produces chaos but no nematic phase.

2. Unfrustrated n-component system: No spin-glass phase, no nematic phase (in the absence of special interactions).

3. Frustrated n-component system ($n \geq 3$): Both spin-glass and nematic phases emerge, with the nematic phase representing a qualitatively new form of order.

This is a clear example of how frustration generates complex RG dynamics: the spin-

glass phase exhibits chaotic flows that cannot be predicted from the behavior of any finite subset of interactions.

The nematic phase discovered here constitutes a liquid-crystal phase in a dirty (quenched-disordered) magnet. This is remarkable for several reasons: The nematic phase persists across a range of temperatures and disorder concentrations, indicating it is a genuine thermodynamic phase rather than a transient phenomenon. The nematic phase owes its existence to frustration—without competing interactions, the system would simply order ferromagnetically or antiferromagnetically at low temperature. The cubic-spin nematic phase is a discretized version of the nematic phase found in the continuous classical Heisenberg spin-glass system (Tunca and Berker, 2023), showing that the essential physics survives discretization.

4.7 Conclusion

We have calculated the phase diagram of the cubic-spin spin-glass system in $d = 3$. We find that a nematic phase, such as seen in the classical Heisenberg model with continuously orientable spins, emerges from the chaotic spin-glass phase, for number of components $n \geq 3$. The calculated Lyapunov exponents λ, measuring the strength of the spin-glass chaos, show odd-even oscillations with respect to the number of cubic spin components n, whereas the strong-coupling runaway exponent y_R has the same low value of $0.24 < d - 1 = 2$ for all n, showing the much unsaturated order of the spin-glass phase.

This chapter establishes that frustration generates novel phases, not merely chaotic dynamics. The nematic phase exists only because frustration prevents conventional order, forcing the system to find an alternative ordering mechanism. The combination of frustration with vector-spin structure produces phases existing in neither the unfrustrated nor scalar-spin frustrated system—a paradigm of emergent complexity.

5. PHASE PROLIFERATION UNDER MAGNETIC FIELDS

5.1 Introduction

5.1.1 Fields as symmetry probes

This chapter investigates two phenomena: the replacement of the spin-glass phase by the nematic phase in continuum-spin Heisenberg spin glass (Tunca and Berker, 2023) and the occurrence of both phases in the discrete yet spin-multidimensional cubic-spin spin glass (Artun et al., 2024). The effect of various magnetic fields in various spin dimensions yields phase diagrams with a large number of very different phases.

5.1.2 Types of magnetic fields for *n*-component spins

For an n-component spin system, n different types of magnetic fields can be applied, each with $n' \leq n$ components and qualitatively different effects. We perform a global RG study for $n = 2$ and 3-component cubic-spin spin-glass systems, applying axial ($n' = 1$), planar-diagonal ($n' = 2$), and body-diagonal ($n' = 3$) magnetic fields, yielding 17 different phases and two spin-glass phase diagram topologies different from conventional ones.

5.2 Model and Method

5.2.1 Hamiltonian with magnetic field

The n-component cubic-spin spin-glass system in an n'-component uniform magnetic field is defined by the Hamiltonian, where $\beta = 1/kT$,

$$-\beta\mathscr{H} = \sum_{\langle ij \rangle} \left[J_{ij}\vec{s}_i \cdot \vec{s}_j + \vec{H} \cdot (\vec{s}_i + \vec{s}_j) \right] \equiv \sum_{\langle ij \rangle} -\beta H_{ij}, \tag{5.1}$$

where $\vec{s}_i$ can be in $2n$ different states $\pm\hat{u}$ at each site i, $\hat{u}$ being orthogonal unit vectors in spin space. The n'-component uniform magnetic field is $\vec{H} = H(\hat{u}_1 + \ldots + \hat{u}_{n'})$, with of course $n' \leq n$. The sum is over nearest-neighbor pairs of sites $\langle ij \rangle$. The interaction J_{ij} is ferromagnetic $+J > 0$ or antiferromagnetic $-J$ with probabilities $1-p$ and p, respectively.

5.2.2 Transfer matrix formulation

The transformation is best implemented algebraically by writing the exponentiated nearest-neighbor Hamiltonian, namely the transfer matrix between two neighboring sites:

$$\mathbf{T}_{ij} \equiv e^{-\beta H_{ij}} = e^{J\vec{s}_i \cdot \vec{s}_j + \vec{H} \cdot (\vec{s}_i + \vec{s}_j)}. \tag{5.2}$$

For $n = 3$ components, the transfer matrices for axial, planar-diagonal, and body-diagonal magnetic fields are, respectively:

Axial field ($\vec{H} = H\hat{x}$):

$$\mathbf{T}_{ij} = \begin{pmatrix} e^{J+2H} & e^{-J} & e^{H} & e^{H} & e^{H} & e^{H} \\ e^{-J} & e^{J-2H} & e^{-H} & e^{-H} & e^{-H} & e^{-H} \\ e^{H} & e^{-H} & e^{J} & e^{-J} & 1 & 1 \\ e^{H} & e^{-H} & e^{-J} & e^{J} & 1 & 1 \\ e^{H} & e^{-H} & 1 & 1 & e^{J} & e^{-J} \\ e^{H} & e^{-H} & 1 & 1 & e^{-J} & e^{J} \end{pmatrix} \tag{5.3}$$

Planar-diagonal field ($\vec{H} = H(\hat{x} + \hat{y})$):

$$\mathbf{T}_{ij} = \begin{pmatrix} e^{J+2H} & e^{-J} & e^{2H} & 1 & e^{H} & e^{H} \\ e^{-J} & e^{J-2H} & 1 & e^{-2H} & e^{-H} & e^{-H} \\ e^{2H} & 1 & e^{J+2H} & e^{-J} & e^{H} & e^{H} \\ 1 & e^{-2H} & e^{-J} & e^{J-2H} & e^{-H} & e^{-H} \\ e^{H} & e^{-H} & e^{H} & e^{-H} & e^{J} & e^{-J} \\ e^{H} & e^{-H} & e^{H} & e^{-H} & e^{-J} & e^{J} \end{pmatrix} \tag{5.4}$$

Body-diagonal field ($\vec{H} = H(\hat{x}+\hat{y}+\hat{z})$):

$$\mathbf{T}_{ij} = \begin{pmatrix} e^{J+2H} & e^{-J} & e^{2H} & 1 & e^{2H} & 1 \\ e^{-J} & e^{J-2H} & 1 & e^{-2H} & 1 & e^{-2H} \\ e^{2H} & 1 & e^{J+2H} & e^{-J} & e^{2H} & 1 \\ 1 & e^{-2H} & e^{-J} & e^{J-2H} & 1 & e^{-2H} \\ e^{2H} & 1 & e^{2H} & 1 & e^{J+2H} & e^{-J} \\ 1 & e^{-2H} & 1 & e^{-2H} & e^{-J} & e^{J-2H} \end{pmatrix} \tag{5.5}$$

In the transfer matrices, the consecutive states are the plus and minus directions of the sequence of spin-space unit vectors $\hat{u}$. The generalization to arbitrary n is obvious and used in this work. These are the transfer matrices of the initial points of renormalization-group trajectories. The transfer matrices do not conserve these forms under the renormalization-group transformations but evolve to one of the 17 asymptotic forms (sinks) given in Table 5.1 and Fig. 5.5, thereby determining the ordering and thermodynamic phase of the initial point of the renormalization-group trajectory.

5.2.3 Renormalization-group procedure

The hierarchical-lattice (Berker and Ostlund, 1979; Griffiths and Kaufman, 1982; Kaufman and Griffiths, 1984) exact renormalization-group solution or, equivalently, the Migdal-Kadanoff (Migdal, 1975; Kadanoff, 1976) approximate renormalization-group solution proceeds as described in previous chapters. The construction of the hierarchical lattice is by first constructing strands of b nearest-neighbor interactions $-\beta H_{ij}$ in series. Here $b = 3$ is the length rescaling factor. Then b^{d-1} such strands are connected in parallel. Here, $d = 3$ is the spatial dimensionality.

For quenched random systems such as here, 5000 graphs are created by randomly choosing $+J$ or $-J$. The renormalization-group solution proceeds by randomly associating b^d such graphs, to generate the renormalized 5000 graphs. Checks conducted with distributions of 10,000 graphs do not change our results to the accuracy of our figures.

In each local renormalization-group transformation, the decimation step consists in matrix-multiplying $b = 3$ transfer matrices randomly chosen from the distribution:

$$\tilde{\mathbf{T}} = \mathbf{T}_1 \cdot \mathbf{T}_2 \cdot \mathbf{T}_3. \tag{5.6}$$

The bond-moving step consists in multiplying the identically placed elements of $b^{d-1} = 9$ decimated transfer matrices:

$$T'(s_i, s_j) = \prod_{k=1}^{9} \tilde{T}_k(s_i, s_j). \tag{5.7}$$

The renormalization-group trajectories starting in a given phase unmistakably reach their respective sinks within eight renormalization-group iterations. Renormalization-group trajectories starting close to a phase boundary spend iterations close to the unstable fixed point controlling the phase boundary, but reach the sink within 15 iterations for the accuracy of our calculation.

5.3 Zero-Field Baseline

Before examining the effects of magnetic fields, we recall the zero-field phase diagram calculated in Chapter 4. The phase diagrams (see Fig. 5.1) are for number of spin components $n = 2$ (light blue lines) and $n = 3$ (blue lines). The vertical ferromagnetic-spin-glass-antiferromagnetic phase boundaries overlap for $n = 2$ and 3. A nematic phase appears for $n = 3$, between the low-temperature spin-glass phase and the high-temperature disordered phase. This zero-field phase diagram serves as the baseline for understanding how magnetic fields restructure the phase diagram.

5.4 Fields on Ferromagnetic Systems

Calculated phase diagrams for the cubic-spin system under planar-diagonal (in the $+xy$ direction) and body-diagonal (in the $+xyz$ direction) magnetic fields, in spatial dimension $d = 3$, for $p = 0$ (the ferromagnetic system), are shown in Fig. 5.2.

In all three cases, a uniaxially aligned symmetry-broken (x or y or z aligned) ordered phase occurs at low temperatures and persists to all high fields. A phase aligned along the applied magnetic field occurs at high temperatures. The phase transition temperatures between these two phases are essentially independent of field strength and join, at the left intercept of the panels, the ferromagnetic transition temperature of the zero-field systems.

Several features are worth noting: The ordered phases at finite field are doubly (x or y

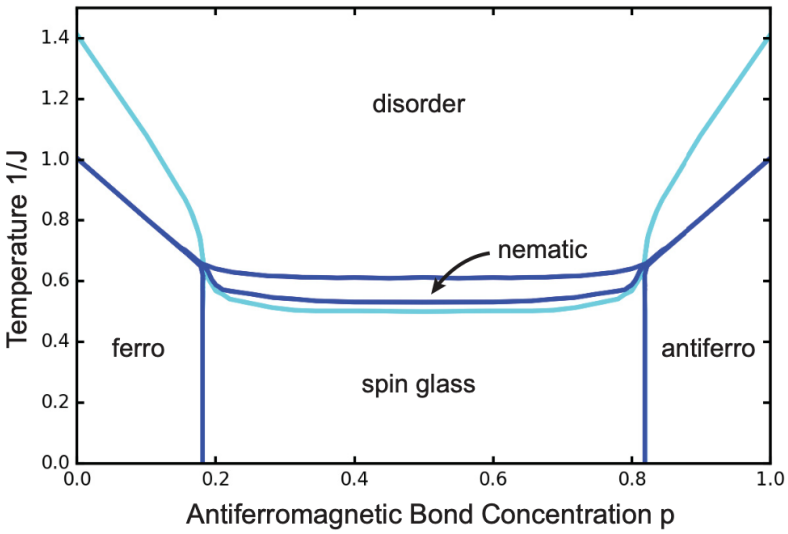


Figure 5.1: Calculated phase diagrams for the cubic-spin spin-glass systems for zero external field in spatial dimension $d = 3$. The phase diagrams are for number of spin components $n = 2$ (light blue lines) and $n = 3$ (blue lines). A nematic phase appears for $n = 3$, between the low-temperature spin-glass phase and the high-temperature disordered phase.

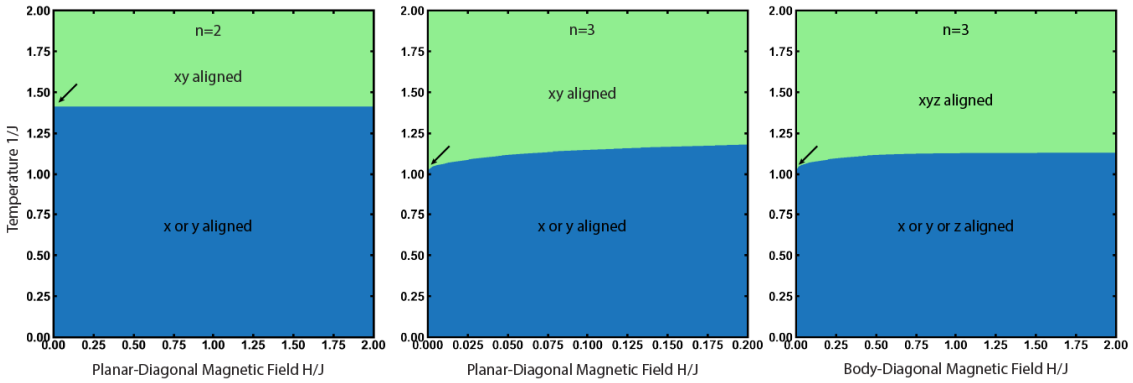


Figure 5.2: Calculated phase diagrams for the cubic-spin system under planar-diagonal and body-diagonal magnetic fields, for $p = 0$ (ferromagnetic system). A uniaxially aligned symmetry-broken ordered phase occurs at low temperatures and persists to all high fields.

aligned, for planar-diagonal field) or triply (x or y or z aligned, for body-diagonal field) degenerate. These degeneracies double at ordered phases joined at zero field, since the reverse magnetized phases also occur. The phase boundaries are essentially horizontal, indicating that the competition between symmetry-broken order and field-aligned order is determined primarily by temperature, not field strength.

With the application to this ferromagnetic system of an axial magnetic field (in the $+x$ direction, even in infinitesimal amount), the ordered phase disappears and the system is uniaxially aligned (along $+x$) at all temperatures. This is the expected behavior: an axial field explicitly breaks the symmetry that the ferromagnetic order would spontaneously break, eliminating the phase transition entirely.

5.5 Fields on Antiferromagnetic Systems

Calculated phase diagrams for the cubic-spin system under axial (in the $+x$ direction), planar-diagonal (in the $+xy$ direction), and body-diagonal (in the $+xyz$ direction) magnetic fields, in spatial dimension $d = 3$, for $p = 1$ (the antiferromagnetic system), are shown in Fig. 5.3.

- *Axial field* (top row): At high temperatures or high fields, the system aligns along the applied field.

- *Planar-diagonal or body-diagonal fields* (bottom row): At high temperatures, the system aligns with the applied field.

In all panels, at low temperatures and low fields, the system orders in the fully antiferromagnetic phase of the zero-field system, namely antiferromagnetic in spin direction x or y or z, each doubly degenerate by spatial translation.

For $n = 3$ under axial or planar-diagonal magnetic fields, an intermediate, less degenerate, antiferromagnetic phase occurs in one of the directions of the axial or planar-diagonal field. In these cases, the fully antiferromagnetic phase persists asymptotically close to the zero-field axis.

For planar-diagonal magnetic field, another ordered phase (doubly degenerate by spatial translation) of xy alternation occurs and continues to all field strengths.

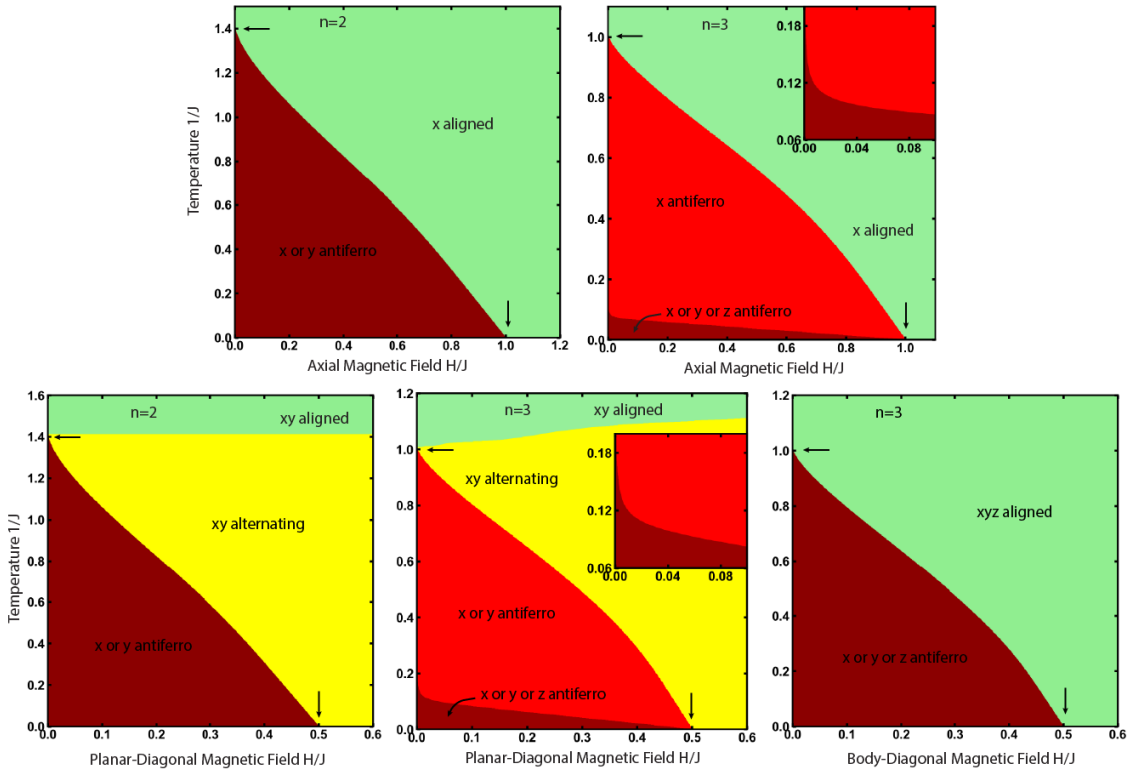


Figure 5.3: Calculated phase diagrams for the cubic-spin system under axial, planar-diagonal, and body-diagonal magnetic fields, for $p = 1$ (antiferromagnetic system). Multiple antiferromagnetic phases with different degeneracies appear.

All finite-temperature phase boundaries meet at the transition temperature of the zero-field system, which thus gives a multiphase point (Hoston and Berker, 1991) of three or four phases, without counting the degeneracies, occurring at finite temperature. The zero-temperature phase transitions occur at the ground-state-energy crossings, which also give multiphase points of three phases.

5.6 Spin-Glass Systems Under Field

5.6.1 Phase diagrams and novel topologies

Calculated phase diagrams for the cubic-spin system under planar-diagonal and body-diagonal magnetic fields, in spatial dimension $d = 3$, for $p = 0.5$ (the spin-glass system), are given in Fig. 5.4. These phase diagrams reveal the most striking results of this chapter.

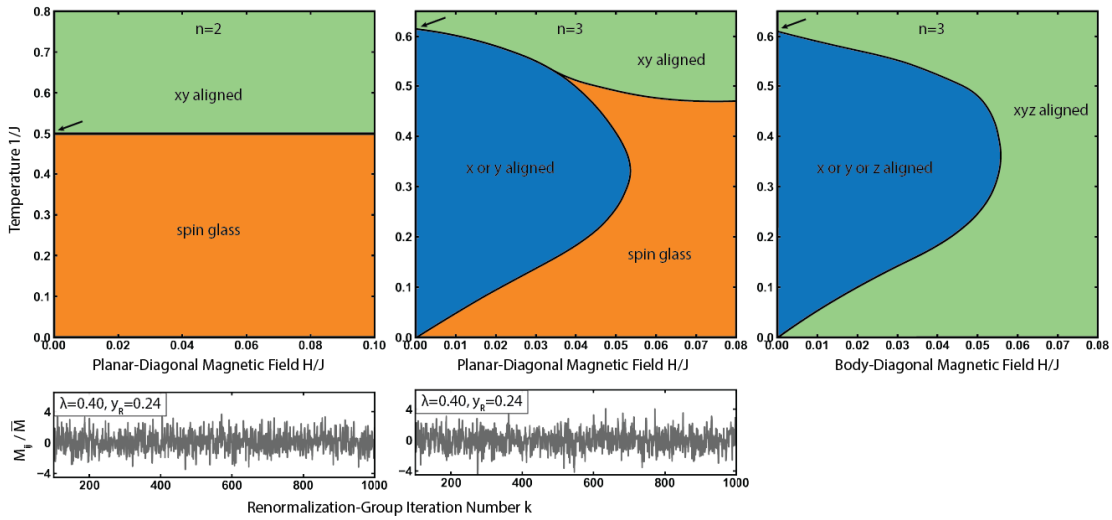


Figure 5.4: Calculated phase diagrams for the cubic-spin system under planar-diagonal and body-diagonal magnetic fields, for $p = 0.5$ (spin-glass system). A spin-glass phase occurs under planar-diagonal magnetic fields with novel topology. The chaotic trajectories and their Lyapunov exponents $\lambda = 0.40$ and runaway exponents $y_R = 0.24$ are shown.

5.6.2 Field-induced spin-glass phase

A spin-glass phase occurs under planar-diagonal magnetic fields. This spin-glass phase results from the asymptotic competition, under renormalization group, of the $+x$ or $+y$ aligned phase and the xy alternating phase. Both of these phases are doubly degenerate, so that the spin-glass phase is quadruply degenerate.

As shown in the second line of Fig. 5.4, a novel chaotic variable is

$$M \equiv \frac{1}{2}\left[-\beta H_{ij}(+x,+x) - \beta H_{ij}(+x,+y)\right] \tag{5.8}$$

that is chaotic under renormalization-group scale change, whereas in conventional spin-glass phases it is

$$J = \frac{1}{2}\left[-\beta H_{ij}(+x,+x) - \beta H_{ij}(+x,-x)\right] \tag{5.9}$$

that is chaotic under renormalization-group scale change.

5.6.3 Asymmetric competition and chaotic variables

Thus, for a cubic-spin spin glass under planar-diagonal magnetic field, an Ising spin-glass phase is realized, but from *asymmetric* phases x or y and xy alternating, rather than from symmetric ferromagnetic and antiferromagnetic phases.

Each of these two spin-glass phase diagram topologies here are very different from conventional spin-glass phase diagram topologies: The axis orthogonal to temperature is not a quenched probability but the magnetic field; one of the competing phases, xy alternating, does not appear in the phase diagram (it is absorbed into the chaotic spin-glass attractor); the spin-glass phase stretches indefinitely in the horizontal axis direction (field strength).

For both $n = 2$ and 3, on the high-temperature side, the transition temperature is unaffected or weakly affected by field strength. An identical behavior occurs in the "usual" spin glasses, where the high-temperature phase transition temperature does not vary or weakly varies in the phase diagram.

In both $n = 3$ cases, namely with or without the occurrence of the spin-glass phase, phase reentrances (Cladis, 1975) occur in the temperature direction. Such phase reentrance behavior has been seen in dipolar liquid crystals (Netz and Berker, 1992; Indekeu et al., 1987), molecular entropic binary liquid mixtures (Vause and Walker, 1982), oversaturatedly adsorbed surface systems (Caflisch et al., 1985), random-field transverse Ising models (Sarmento and Kaneyoshi, 1989), and high-curvature (black hole) gravity (Frassino et al., 2014; Dehghani et al., 2020).

The zero-field intercepts of the phase boundaries in Fig. 5.4 are the transition points be-

tween: the disordered phase and the zero-field spin glass for $n = 2$, and the disordered phase and the zero-field nematic phase for $n = 3$.

Our (exact for hierarchical model) calculation does not give any finite-field phase boundary that ends on the zero-field spin-glass-nematic transition. Thus, the nematic phase appears only for field-free conditions.

On the other hand, with the application to this spin-glass system of an axial magnetic field (in the $+x$ direction, even in infinitesimal amount), the spin-glass phase disappears and the system is uniaxially aligned (along $+x$) at all temperatures. This is consistent with the known result that an Ising ($n = 1$) spin-glass phase is destroyed by infinitesimal uniform field (Berker, 2010).

5.7 Spin-Glass Chaos Characterization

The renormalization-group trajectories in the spin-glass phases are chaotic, as shown in the second line of Fig. 5.4. The strength of chaos under scale change (McKay et al., 1982a,b; Berker and McKay, 1984; McKay and Berker, 1984) is measured by the Lyapunov exponent (Collet and Eckmann, 1980; Hilborn, 2003),

$$\lambda = \lim_{n\to\infty} \frac{1}{n} \sum_{k=0}^{n-1} \ln \left| \frac{dx_{k+1}}{dx_k} \right|, \tag{5.10}$$

where, in the current case, $x_k = M/\overline{M}$ at step k of the renormalization-group trajectory, with M defined as in Eq. (5.8) and $\overline{M}$ being the average of its absolute value in the quenched random distribution.

We calculate the Lyapunov exponents by discarding the first 100 renormalization-group steps (to eliminate crossover from initial conditions to asymptotic behavior) and then using the next 900 steps. As expected from the previous analysis, these very different variables and topologies still give the Ising Lyapunov exponent of $\lambda = 0.40$, whereas non-Ising Lyapunov exponents do very commonly occur (Artun et al., 2024).

In addition to chaos, the renormalization-group trajectories show asymptotic strong-coupling behavior (Demirtaş et al., 2015),

$$\overline{M}' = b^{y_R} \overline{M}, \tag{5.11}$$

where the prime denotes renormalized and $y_R > 0$ is the strong-coupling runaway expo-

nent (Demirtaş et al., 2015). Again using 900 renormalization-group steps after discarding 100 steps, we find here the same value of $y_R = 0.24$, which appears to be common to a large number of otherwise different spin glasses, also reflecting that spin-glass order is a very unsaturated order (Artun et al., 2024).

The fact that y_R is much less than $d - 1 = 2$ indeed shows that this spin-glass order is a very unsaturated order: In the compact (saturating) ordering of systems without quenched randomness, $y_R = d - 1$ reflects the energy of the smooth interface between oppositely aligned renormalization-group cells (Berker and Wortis, 1976).

5.8 Classification of All Seventeen Phases

Table 5.1 presents the renormalization-group sinks for all 17 phases discovered in this study. Under repeated renormalization-group transformations, the phase diagram points of the phases flow to these sinks, giving the exponentiated nearest-neighbor Hamiltonians (transfer matrices). The number of coexisting phases are shown in parentheses.

The sinks reveal the physical nature of each phase:

- Aligned phases: Single nonzero element in the transfer matrix
- Coexistence phases: Multiple nonzero elements indicating degenerate ground states
- Alternating phases: Off-diagonal elements indicating spatial modulation
- Antiferromagnetic phases: Pattern reflecting sublattice structure
- Disordered phase: All elements equal to 1
- Spin-glass phase: Fixed distribution (Fig. 5.5) rather than fixed point

5.9 Discussion and Conclusion

This chapter provides a dramatic demonstration of how external fields interact with frustration to produce complexity:

Table 5.1: Renormalization-group sinks of the $n = 2$ and $n = 3$ finite-field thermodynamic phases. The matrices represent the sink transfer matrices. The number of coexisting phases are shown in parenthesis.

Renormalization-group sinks of the $n = 2$ finite-field thermodynamic phases

$\begin{pmatrix} 1&0&0&0\\ 0&0&0&0\\ 0&0&0&0\\ 0&0&0&0 \end{pmatrix}$	$\begin{pmatrix} 1&0&1&0\\ 0&0&0&0\\ 1&0&1&0\\ 0&0&0&0 \end{pmatrix}$	$\begin{pmatrix} 0&0&1&0\\ 0&0&0&0\\ 1&0&0&0\\ 0&0&0&0 \end{pmatrix}$	$\begin{pmatrix} 1&0&0&0\\ 0&0&0&0\\ 0&0&1&0\\ 0&0&0&0 \end{pmatrix}$	$\begin{pmatrix} 0&1&0&0\\ 1&0&0&0\\ 0&0&0&0\\ 0&0&0&0 \end{pmatrix}$	$\begin{pmatrix} 0&1&0&0\\ 1&0&0&0\\ 0&0&0&1\\ 0&0&1&0 \end{pmatrix}$
Axial x aligned	Planar xy aligned	xy alternating (2)	x or y aligned (2)	x antiferro (2)	x or y antiferro (4)

Renormalization-group sinks of the $n = 3$ finite-field thermodynamic phases

$\begin{pmatrix} 1&0&0&0&0&0\\ 0&0&0&0&0&0\\ 0&0&0&0&0&0\\ 0&0&0&0&0&0\\ 0&0&0&0&0&0\\ 0&0&0&0&0&0 \end{pmatrix}$	$\begin{pmatrix} 1&0&1&0&0&0\\ 0&0&0&0&0&0\\ 1&0&1&0&0&0\\ 0&0&0&0&0&0\\ 0&0&0&0&0&0\\ 0&0&0&0&0&0 \end{pmatrix}$	$\begin{pmatrix} 1&0&1&0&1&0\\ 0&0&0&0&0&0\\ 1&0&1&0&1&0\\ 0&0&0&0&0&0\\ 1&0&1&0&1&0\\ 0&0&0&0&0&0 \end{pmatrix}$	$\begin{pmatrix} 0&0&1&0&0&0\\ 0&0&0&0&0&0\\ 1&0&0&0&0&0\\ 0&0&0&0&0&0\\ 0&0&0&0&0&0\\ 0&0&0&0&0&0 \end{pmatrix}$	$\begin{pmatrix} 1&1&1&1&1&1\\ 1&1&1&1&1&1\\ 1&1&1&1&1&1\\ 1&1&1&1&1&1\\ 1&1&1&1&1&1\\ 1&1&1&1&1&1 \end{pmatrix}$
Axial x aligned	Planar xy aligned	Body xyz aligned	xy alternating (2)	Disordered
$\begin{pmatrix} 1&0&0&0&0&0\\ 0&0&0&0&0&0\\ 0&0&1&0&0&0\\ 0&0&0&0&0&0\\ 0&0&0&0&0&0\\ 0&0&0&0&0&0 \end{pmatrix}$	$\begin{pmatrix} 1&0&0&0&0&0\\ 0&0&0&0&0&0\\ 0&0&1&0&0&0\\ 0&0&0&0&0&0\\ 0&0&0&0&1&0\\ 0&0&0&0&0&0 \end{pmatrix}$	$\begin{pmatrix} 0&1&0&0&0&0\\ 1&0&0&0&0&0\\ 0&0&0&0&0&0\\ 0&0&0&0&0&0\\ 0&0&0&0&0&0\\ 0&0&0&0&0&0 \end{pmatrix}$	$\begin{pmatrix} 0&1&0&0&0&0\\ 1&0&0&0&0&0\\ 0&0&0&1&0&0\\ 0&0&1&0&0&0\\ 0&0&0&0&0&0\\ 0&0&0&0&0&0 \end{pmatrix}$	$\begin{pmatrix} 0&1&0&0&0&0\\ 1&0&0&0&0&0\\ 0&0&0&1&0&0\\ 0&0&1&0&0&0\\ 0&0&0&0&0&1\\ 0&0&0&0&1&0 \end{pmatrix}$
x or y aligned (2)	x or y or z aligned (3)	x antiferro (2)	x or y antiferro (4)	x, y, or z antiferro (6)

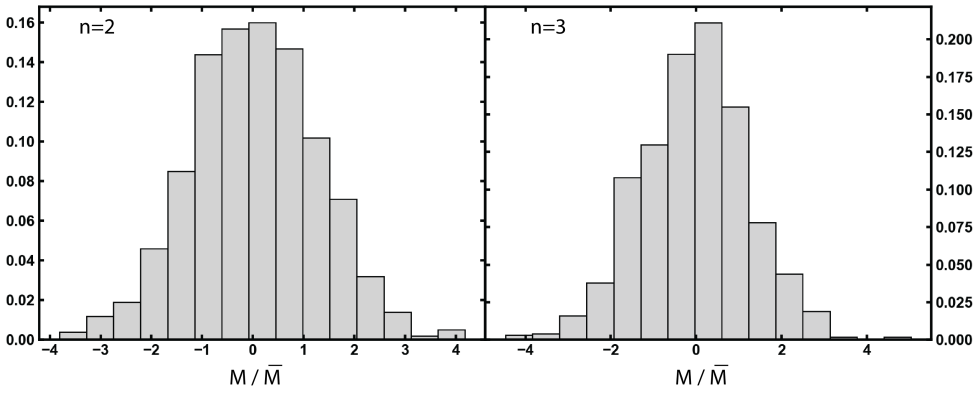


Figure 5.5: Fixed distributions that are the sinks of the spin-glass phases. The fixed distributions of the chaotic variable $M = [-\beta H_{ij}(+x,+x) - \beta H_{ij}(+x,+y)]/2$ are given.

Table 5.2: Phase proliferation under magnetic field.

System	Zero Field	With Field	Change
Ferromagnetic ($p = 0$)	2 phases	3 phases	+1
Antiferromagnetic ($p = 1$)	2 phases	4–5 phases	+2 to +3
Spin glass ($p = 0.5$)	4–5 phases	6–8 phases	+2 to +3
Total distinct phases	5	**17**	**+12**

The proliferation of phases under field is not simply additive—it reflects qualitative restructuring of the phase diagram topology.

The discovery of two qualitatively different spin-glass phase-diagram topologies is significant:

- *Field-continued topology* ($n = 2$, planar-diagonal field): The spin-glass phase at finite field is continuously connected to the zero-field spin-glass phase.

- *Field-induced topology* (alternative scenario): The spin-glass phase appears only at finite field, with no connection to zero-field behavior.

Both topologies share the characteristic that the horizontal axis is magnetic field strength rather than quenched disorder concentration—a strong departure from conventional spin-glass phenomenology.

It is of interest that such a discrete-spin model houses two different spin-glass phases (counting the one at zero fields) and the nematic phase (at zero field), both of which are high built-in entropy phases—the spin glass due to frustration and the nematic due to bidirectional ordering. Furthermore, the spin-glass phase here under finite field presents two qualitatively different phase diagram topologies, namely, field continued (from zero field) and field induced (at finite field).

Moreover, the competing orderings in the field-induced spin glass are $+x$ or $+y$ aligned versus xy alternating—phases that do not map onto each other under any symmetry. This is in contrast to conventional spin glasses where the competing phases (ferromagnetic versus antiferromagnetic, or left versus right chiral (Çağlar and Berker, 2017a)) are related by a symmetry transformation.

We have solved the $n = 2$ and 3-component cubic-spin spin-glass system under uniform axial, planar-diagonal, and body-diagonal magnetic fields. We find 17 different phases including a spin-glass phase and two spin-glass phase-diagram topologies very different from the conventional spin-glass phase-diagram topologies.

This chapter establishes several key points for the thesis argument:

1. *Fields as complexity amplifiers*: External magnetic fields do not simply select among

existing phases but qualitatively restructure the phase diagram, creating new phases and new topologies.

2. *Novel spin-glass phenomenology*: The field-induced spin glass has the magnetic field (not disorder concentration) as the control parameter—a paradigm shift in spin-glass physics.

3. *Universal chaos characteristics*: Despite the novel topology and competing phases, the Lyapunov exponent and runaway exponent maintain their universal values, confirming that these are robust characteristics of spin-glass order.

4. *Frustration enables field effects*: The rich phase structure under field exists only because frustration prevents simple alignment—the field competes with multiple ordering tendencies rather than a single ground state.

6. SURFACE CHAOS IN SPIN-GLASS SPONGES

6.1 Introduction

6.1.1 Surfaces and boundaries in statistical mechanics

All materials are largely observed from their surfaces, so we have studied in $d = 3$ the spin-glass systems with a surface. We find both bulk-chaos-driven surface chaos and surface chaos in the absence of bulk chaos. The latter phenomenon does occur not on flat surfaces, but on convoluted fractal surfaces, namely in spin-glass sponges. All chaoses are numerically observed and quantified by distinctive Lyapunov exponents. These results may further refine the spin-glass chaos classification scheme which was developed by Artun et al. (2023a), in systems with identifiable peripheral complexity.

6.1.2 Dimensional thresholds for spin-glass order

This chapter completes the exploration of frustration as complexity generator by demonstrating how spatial topology modifies the expression of spin-glass chaos. While Chapters 3–5 examined spin-glass behavior in homogeneous bulk systems, this chapter introduces inhomogeneity through the surface-bulk distinction, revealing:

1. *Driven versus intrinsic chaos*: Surface spin-glass order can arise either through coupling to a chaotic bulk (driven chaos) or spontaneously on fractal surfaces (intrinsic chaos). These represent fundamentally different mechanisms for complexity generation.

2. *Dimensional threshold for surface chaos*: A flat ($d_S = d - 1 = 2$) surface cannot sustain spin-glass order independently, but fractal surfaces with $d_S > 2$ can. This connects to the known lower-critical dimension $d_c \simeq 2.5$ for spin-glass phases.

3. *Hierarchy of Lyapunov exponents*: The three types of chaos (sole surface, driven

surface, bulk) have distinct Lyapunov exponents, with the ordering $\lambda_S > \lambda_D$ and $\lambda_B > \lambda_D$. This provides a refined classification of chaotic phenomena.

4. *Special multicritical point*: The meeting of three phases (surface-only spin glass, bulk-and-surface spin glass, disordered) at a multicritical point represents a new type of critical behavior specific to inhomogeneous frustrated systems.

In the thesis framework, this chapter demonstrates that spatial topology acts as a modulator that can either suppress (flat surface) or enable (fractal surface) the complexity generated by frustration.

6.2 Model: The Spin-Glass Sponge

6.2.1 Bulk and surface interactions

The surfaced spin-glass system is defined by the Hamiltonian

$$-\beta\mathscr{H} = \sum_{\langle ij\rangle}^{S} J_{ij}^{S} s_i s_j + \sum_{\langle ij\rangle}^{B} J_{ij}^{B} s_i s_j, \tag{6.1}$$

where $\beta = 1/kT$, $s_i = \pm 1$ at each site i of the semi-infinite d-dimensional lattice, and the first (second) sum $\langle ij\rangle$ is over all pairs of nearest-neighbor sites in the surface (bulk).

The surface bond J_{ij}^{S} is ferromagnetic $+J_S > 0$ or antiferromagnetic $-J_S$ with probabilities $1 - p_S$ and p_S, respectively. The bulk bond J_{ij}^{B} is ferromagnetic $+J_B > 0$ or antiferromagnetic $-J_B$ with probabilities $1 - p_B$ and p_B, respectively.

We concentrate on full realization of spin-glass order, and therefore study $p_S = p_B = 0.5$. The complete range of random interaction strengths J_S and J_B is studied and phase diagrams are obtained.

6.2.2 Surface dimensionality and sponge geometry

The key parameter distinguishing different surfaced systems is the surface dimensionality d_S:

- Flat surface: $d_S = d - 1 = 2$ for bulk $d = 3$

- Fractal (sponge) surface: $d - 1 < d_S < d$, i.e., $2 < d_S < 3$

The sponge is characterized by two parameters: b^{d_S} (determining surface dimensionality) and n (the number of bulk bonds contributing to surface renormalization). Different combinations (b^{d_S}, n) give different sponge geometries with varying degrees of "sponginess."

6.3 Renormalization-Group Method for Surfaced Systems

6.3.1 Double-graph hierarchical construction

The renormalization-group theory of surfaced systems is most easily done with the Migdal-Kadanoff procedure (Migdal, 1975; Kadanoff, 1976) or, equivalently, the exactly solvable hierarchical models (Berker and McKay, 1984; Berker and Ostlund, 1979; Griffiths and Kaufman, 1982; Kaufman and Griffiths, 1984). The procedure is similar to the solution of anisotropic spin, percolation, high-T_C superconductivity, and spin-glass systems, where two interconnected graphs are used (Erbaş et al., 2005; Hinczewski and Berker, 2006; Güven, 2008).

The Migdal-Kadanoff procedure is a physically intuited approximation: A system is rendered renormalizable by removing some of the bonds. Thus a scale change can be achieved by decimation. Then the effect of the removed bonds is added and the renormalized interactions are obtained.

In surfaced systems, the bulk is transformed as just explained. It is transformed by decimation followed by bond-moving, with the final addition involving the sum of b^{d-1} decimated bulk bonds, where d is the bulk spatial dimensionality and b is the length-rescaling factor. For the surface, the final addition involves the sum of b^{d_S-1} decimated surface bonds and n decimated bulk bonds, where d_S is the surface spatial dimensionality and, from the interior,

$$n = \frac{b^{d-1} - b^{d_S-1}}{2}. \tag{6.2}$$

For flat surfaces, $d_S = d - 1$ and, for fractal surfaces, $d - 1 < d_S < d$. Furthermore, we use different values of n, as long as $n + b^{d_S-1} < b^{d-1}$, thus conserving contact with the

outside.

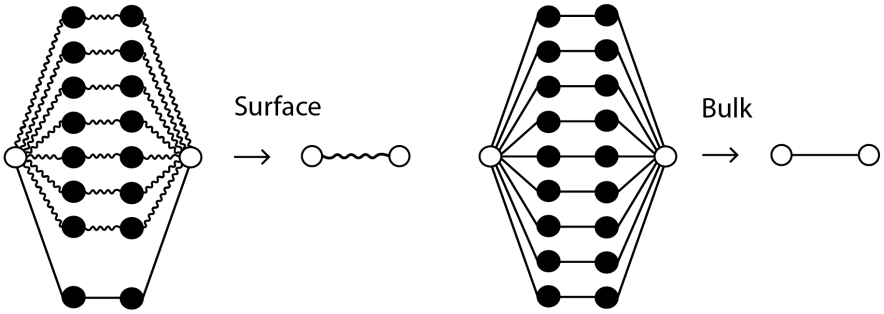


Figure 6.1: Exact renormalization-group transformation for the surfaced hierarchical model. The straight and squiggly lines represent bulk and surface bonds, respectively. The hierarchical lattice is constructed by proceeding in the opposite direction, multiply self-imbedding and cross-imbedding the double graphs.

The double-graphical (Erbaş et al., 2005; Hinczewski and Berker, 2006; Güven, 2008) representation of the equivalent, exactly solved hierarchical lattice (Berker and McKay, 1984; Berker and Ostlund, 1979; Griffiths and Kaufman, 1982; Kaufman and Griffiths, 1984) is shown in Fig. 6.1. The straight and squiggly lines represent bulk and surface bonds, respectively. The hierarchical lattice is constructed by proceeding in the opposite direction, multiply self-imbedding and cross-imbedding the double graphs.

Such a double-graph hierarchical model construction was previously used in the study of anisotropic spin, percolation, high-T_C superconductivity, and spin-glass systems (Erbaş et al., 2005; Hinczewski and Berker, 2006; Güven, 2008). Exactly solved hierarchical lattices are widely used for a large variety of systems (Artun et al., 2023a; Clark and Lochridge, 2023; Kotorowicz and Kozitsky, 2022; Zhang et al., 2022; Jiang et al., 2021; Chio and Roeder, 2021; Myshlyavtsev et al., 2020; Derevyagin et al., 2020; Chang et al., 2020; Monthus, 2020). Thus, the Migdal-Kadanoff approximation is a physically realizable approximation, as is used in turbulence (Kraichnan, 1961), polymers (Kaufman, 1990), electronic systems (Lloyd and Oglesby, 1976), and therefore a robust approximation (e.g., it will never yield a negative entropy).

6.3.2 Coupled distribution flows

For quenched random systems, a distribution of bulk interactions and a distribution of surface interactions are used in the calculation. We use, for each distribution, 15,000 interactions originally bimodally chosen as described above. At each renormalization-

group step:

- b^d bulk interactions, randomly chosen from the bulk distribution, give a renormalized bulk interaction

- b^{d_S} surface interactions and bn bulk interactions, randomly chosen from their respective distributions, give a renormalized surface interaction

Both distributions are renormalized (and of course do not remain bimodal) by repeating this operation 15,000 times. Under repeated renormalization-group transformations, each phase, phase boundary and, in this case, special multicritical point is attracted to its own fixed distribution and, thus, phase diagrams are obtained.

6.4 Phase Diagrams

6.4.1 Surface-only spin-glass phase

Calculated phase diagrams for sponge surface dimensionalities $d_S = 2.77$ and 2.63 are shown in Fig. 6.2. The sponges are indicated with (b^{d_S}, n) next to the surface-only chaos boundary.

Both of these spin-glass sponges exhibit surface spin-glass ordering in the absence of bulk spin-glass ordering. The phase diagram has:

1. *Surface-only spin-glass ordered phase*: Spin-glass order exists on the surface but not in the bulk

2. *Surface-and-bulk spin-glass ordered phase*: Both surface and bulk exhibit spin-glass order

3. *Disordered phase*: Neither surface nor bulk is ordered

The bulk ordering is not affected by the surface interaction, so that the phase boundary to the surface-and-bulk spin-glass ordered phase is a vertical line in the J_S-J_B phase diagram. This vertical boundary covers the phase transitions to both the surface-only spin-glass ordered phase and the disordered phase.

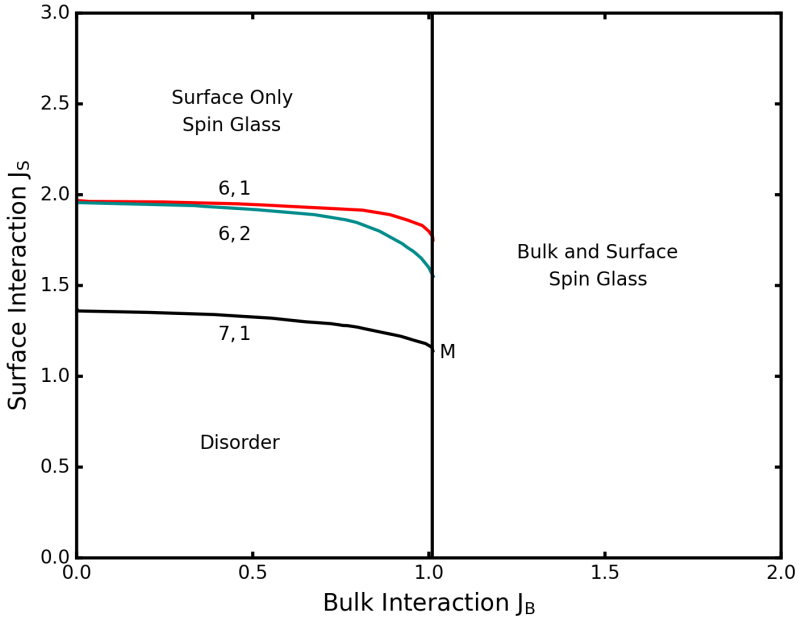


Figure 6.2: Calculated phase diagrams for sponge surface dimensionalities $d_S = 2.77$ and 2.63. The sponges are indicated with (b^{d_S}, n) next to the surface-only chaos boundary. These spin-glass sponges exhibit surface spin-glass ordering in the absence of bulk spin-glass ordering. The phase diagram has a surface-only spin-glass ordered phase, a surface-and-bulk spin-glass ordered phase, and a disordered phase. The three phase boundary lines meet at the special multicritical point M.

On the other hand, the bulk interaction J_B enhances surface-only spin-glass ordering, even in the absence of bulk spin-glass ordering. This is seen from the downwards deviation, as the bulk interaction J_B increases, of the near-horizontal phase boundary between the surface-only spin-glass and disordered phases. As expected, the two phase boundaries for the same d_S merge as J_B goes to zero.

6.4.2 The special multicritical point

The three phase boundary lines meet at a special multicritical point M. This multicritical point represents a unique type of critical behavior where:

- Surface spin-glass order onsets simultaneously with bulk spin-glass order
- The critical fluctuations of both subsystems become correlated
- The universality class is distinct from either pure bulk or pure surface transitions

Sponge surfaces with $d_S \leq 2.46$ do not exhibit a surface-only spin-glass ordered phase. The surface-only spin-glass ordered phase transition has a finite transition temperature at $d_S = 2.63$ as seen in Fig. 6.2. Thus this transition must also occur at dimensions below $d_S = 2.63$, but, in our sequence of lattices, does not occur at $d_S = 2.46$. This is consistent with the knowledge that the spin-glass lower-critical dimension, where the transition temperature reaches zero, is around 2.5 (Franz et al., 1994; Amoruso et al., 2003; Bouchaud et al., 2003; Boettcher, 2005; Demirtaş et al., 2015; Maiorano and Parisi, 2018; Atalay and Berker, 2018). Our sequence of models does not access dimensions $2.63 > d > 2.46$, but the results strongly suggest that the surface spin-glass lower-critical dimension lies in this interval.

6.5 Three Types of Chaos

The asymptotically chaotic renormalization-group trajectories starting within the surface or bulk spin-glass phase are shown in Fig. 6.3, where the consecutively renormalized (combining with neighboring interactions) values at a given location $\langle ij \rangle$ are followed.

For each of our three sponge systems, we identify three distinct types of chaos:

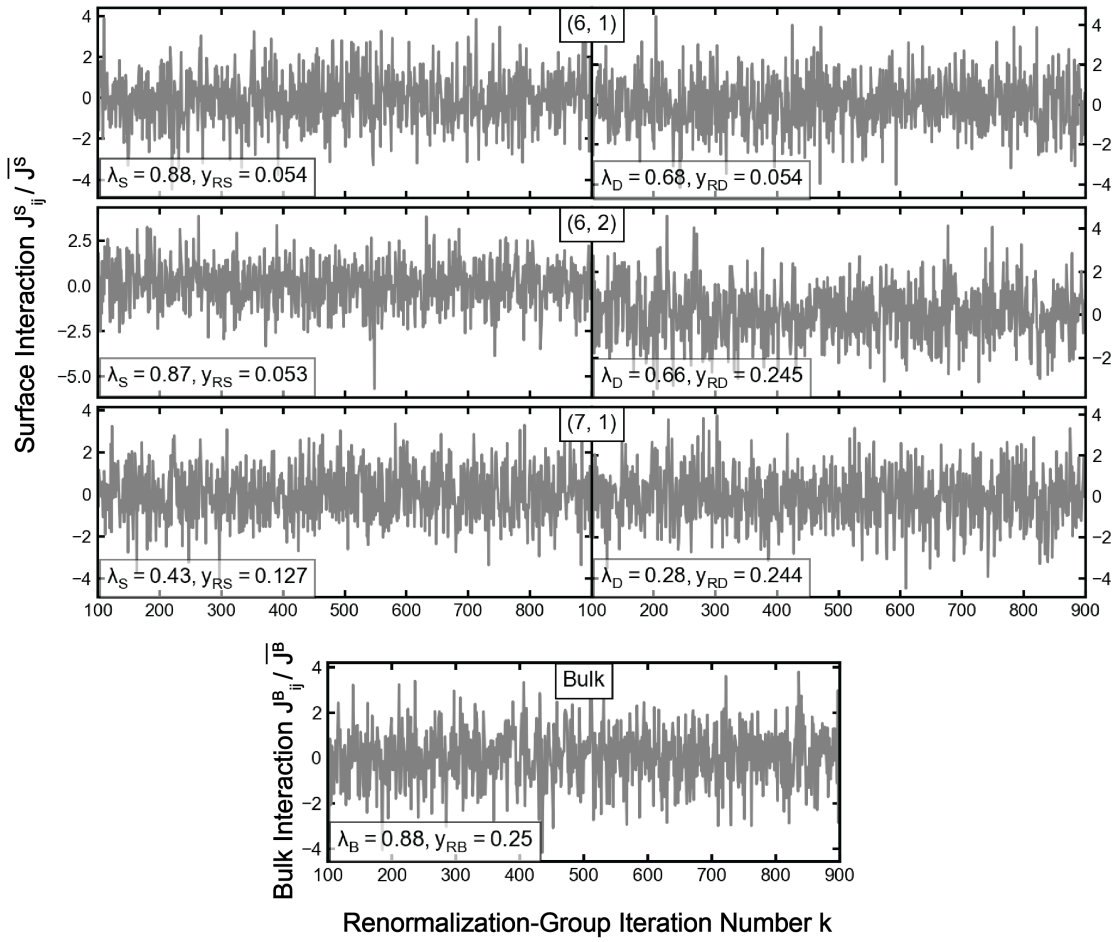


Figure 6.3: For each of our three spin-glass sponges (7,1), (6,2), (6,1), the chaotic renormalization-group trajectories for sole surface chaos (S), driven surface chaos (D), and bulk chaos (B). The calculated Lyapunov exponents λ_S, λ_D, λ_B and runaway exponents y_{RS}, y_{RD}, y_{RB} are given. The bulk is not influenced by the surface and thus the bulk items are the same for all three systems.

1. *Sole surface chaos* (*S*): Chaotic trajectories of surface interactions when the bulk is disordered

2. *Driven surface chaos* (*D*): Chaotic trajectories of surface interactions when the bulk is also spin-glass ordered

3. *Bulk chaos* (*B*): Chaotic trajectories of bulk interactions (independent of surface state)

The strength of chaos is measured by the Lyapunov exponent (Collet and Eckmann, 1980; Hilborn, 2003)

$$\lambda = \lim_{n\to\infty} \frac{1}{n} \sum_{k=0}^{n-1} \ln \left| \frac{dx_{k+1}}{dx_k} \right|, \tag{6.3}$$

where $x_k = J_{ij}/\overline{J}$ at step k of the renormalization-group trajectory and $\overline{J}$ is the average of the absolute value of the interactions in the quenched random distribution.

We calculate the Lyapunov exponents by discarding the first 100 renormalization-group steps (to eliminate crossover from initial conditions to asymptotic behavior) and then using the next 800 steps. The initial (J_B, J_S) values do not matter, as long as they are within the specified spin-glass phase.

For the $b^{d_S} = 6$, namely $d_S = 2.63$ systems, after decimation the strong coupling interactions, in certain of the randomly chosen combinations, do nearly cancel each other, meaning frustration. In these cases, the derivative in Eq. (6.3) is vanishingly small and not included in the summation, when the result of the bond-moving gives an interaction which is 10^{-6} times or less than the average interaction in the distribution. Chaotic runaway does of course continue in the next renormalization-group iteration.

Table 6.1: Calculated Lyapunov exponents for the three types of chaos in spin-glass sponges.

Sponge (b^{d_S}, n)	d_S	λ_S (sole surface)	λ_D (driven)	λ_B (bulk)
(6, 1)	2.63	0.43	0.28	0.88
(6, 2)	2.63	0.87	0.66	0.88
(7, 1)	2.77	0.88	0.68	0.88

In all three sponges, the Lyapunov exponent is larger (chaos is stronger) for sole surface chaos than for driven chaos:

$$\lambda_S > \lambda_D \tag{6.4}$$

The Lyapunov exponent is even larger and chaos is even stronger for bulk chaos in all three systems. The bulk is not influenced by the surface, so the bulk items ($\lambda_B = 0.88$) are the same for all three systems.

In addition to chaos, the renormalization-group trajectories show asymptotic strong-coupling behavior,

$$\overline{J}' = b^{y_R}\overline{J}, \tag{6.5}$$

where $y_R > 0$ is the runaway exponent (Demirtaş et al., 2015). Again using 800 renormalization-group steps after discarding 100 steps, we calculated the runaway exponent for sole surface chaos y_{RS}, driven surface chaos y_{RD}, and bulk chaos y_{RB}.

Table 6.2: Calculated runaway exponents for the three types of chaos in spin-glass sponges.

Sponge (b^{d_S}, n)	d_S	y_{RS} (sole surface)	y_{RD} (driven)	y_{RB} (bulk)
(6, 1)	2.63	0.127	0.244	0.25
(6, 2)	2.63	0.053	0.245	0.25
(7, 1)	2.77	0.054	0.054	0.25

The sole surface runaway exponents ($y_{RS} \approx 0.05$–0.13) are consistently smaller than the driven and bulk runaway exponents ($y_{RD} \approx 0.24$–0.25, $y_{RB} = 0.25$). This indicates that sole surface spin-glass order is even more "unsaturated" than bulk spin-glass order.

6.6 Physical Interpretation: Intrinsic Versus Driven Complexity

The ordering $\lambda_S > \lambda_D$ has a physical interpretation: coupling to the chaotic bulk actually reduces the chaos strength of the surface. This counterintuitive result can be understood as follows:

- In sole surface chaos, the surface degrees of freedom evolve according to their own frustrated dynamics, leading to strong chaos.
- In driven surface chaos, the bulk provides an additional "bath" that partially regularizes the surface dynamics, reducing the effective chaos strength.
- The bulk chaos is the strongest because the bulk has full dimensionality ($d = 3$) and is not constrained by boundary effects.

The fractal (sponge) surface topology enables surface spin-glass order that would not

exist on a flat surface. This is because: The fractal surface has $d_S > 2$, placing it above the spin-glass lower-critical dimension; the sponge geometry provides more pathways for spin-spin correlations, strengthening the tendency toward order; the "interior" surface of the sponge has different boundary conditions than a flat exterior surface.

The distinction between sole surface chaos, driven surface chaos, and bulk chaos provides a refined classification scheme for chaotic phenomena:

1. *Intrinsic chaos*: Arises from the internal dynamics of a subsystem (sole surface chaos)

2. *Driven chaos*: Arises from coupling to an external chaotic bath (driven surface chaos)

3. *Bulk chaos*: The "standard" chaos of a homogeneous frustrated system

This classification may be applicable beyond spin glasses, to any system where a smaller-dimensional subsystem is coupled to a larger-dimensional chaotic environment.

6.7 Conclusion

We have studied surfaced spin-glass systems by exact renormalization-group theory of $d = 3$ hierarchical lattices. We find that a flat surface does not support chaotic rescaling and therefore does not have a surface spin-glass phase. Therefore, we have constructed spin-glass sponges, with higher fractal dimensional surfaces. We find that for higher "spongevity," surface chaotic rescaling occurs even in absence of bulk chaotic rescaling.

We calculate phase diagrams with sole surface spin-glass phase, surface-and-bulk spin-glass phase, and disordered phase. All three phases meet at a special multicritical point M.

Chaos in the sole surface spin-glass phase is stronger than in the bulk-driven surface spin glass.

This chapter demonstrates that spatial topology modulates the expression of frustration. Flat surfaces ($d_S = 2$) cannot sustain independent spin-glass order, but fractal surfaces

above the lower-critical dimension can. The distinction between driven and intrinsic chaos represents a fundamental dichotomy in complexity generation.

7. SYMMETRY COMPETITION IN MERGED POTTS-CLOCK MODELS

7.1 Introduction

7.1.1 Potts Symmetry Versus Clock Symmetry

The q-state Potts models, ever since the establishment of their quantitative relevance to surface phase transitions (Berker et al., 1978) and of the intricate renormalization-group mechanism for their changeover from second- to first-order phase transitions (Nienhuis et al., 1979; Andelman and Berker, 1981), have held high interest in statistical physics. The q-state clock models, ever since the establishment of their algebraic ordering in relation to the XY model (José et al., 1977), have also held high interest. In this chapter, we merge the two models into the q-state Potts-clock models and solve, in spatial dimensions $d = 2$ and $d = 3$, with the recently improved Migdal-Kadanoff approximation (Devre and Berker, 2022) or, equivalently, exactly on hierarchical lattices (Berker and Ostlund, 1979; Griffiths and Kaufman, 1982; Kaufman and Griffiths, 1984; Berker and McKay, 1984), obtaining algebraically (Berker and Kadanoff, 1980a; Saleur, 1991; Ilker and Berker, 2014b) and conventionally ordered multistructured multicritical global phase diagrams.

This merged model has been recently studied (Polackova and Gendiar, 2023) on the square lattice for $q = 6$ for positive couplings J and K (see below) by the corner transfer matrix renormalization-group method, showing the ferromagnetic phase with a single phase transition from the disordered phase for the Potts limit and with a narrow intermediate BKT phase in the clock limit.

This chapter provides the first major demonstration of symmetry competition as a complexity generator as defined in Chapter 1. The merged Potts-clock model combines two fundamentally different symmetries: In the Potts interaction $J\delta(s_i, s_j)$, all states that differ from a reference state are energetically equivalent—there is no notion of "neighboring" states in spin space, unlike the clock model where angular proximity matters. In the

clock interaction $K\vec{s}_i \cdot \vec{s}_j = K\cos\big(2\pi(n_i - n_j)/q\big)$, states have a natural geometric relationship. States that are "nearby" in angle contribute differently than states that are "far apart."

7.1.2 Incompatible ordering tendencies

These symmetries have incompatible ordering tendencies: The Potts term favors alignment ($s_i = s_j$) or antialignment ($s_i \neq s_j$) with no intermediate preference; the clock term favors smooth angular alignment with a continuous spectrum of energies depending on angular separation. When both interactions are present with independent strengths J and K, neither symmetry can be fully satisfied. The system responds by generating five distinct ordered phases—ferromagnetic, quadrupolar, antiferromagnetic, algebraic antiferromagnetic, and algebraic antiquadrupolar—connected by a rich network of phase boundaries and multicritical points.

The contrast between even-q and odd-q systems is particularly striking: even-q systems exhibit conventional antiferromagnetic order, while odd-q systems exhibit algebraic antiferromagnetic order due to ground-state entropy. This demonstrates how microscopic degeneracy structure propagates through the RG to determine macroscopic phase topology.

Chapters 3–6 demonstrated how frustration produces complexity through chaotic RG flows. This chapter demonstrates a complementary mechanism: symmetry competition produces complexity through phase proliferation, even in the absence of quenched disorder or frustration.

7.2 Model

The merged Potts-clock model is defined by the Hamiltonian

$$-\beta\mathscr{H} = \sum_{\langle ij\rangle} \left[J\,\delta(\vec{s}_i, \vec{s}_j) + K\,\vec{s}_i \cdot \vec{s}_j\right], \tag{7.1}$$

where $\beta = 1/k_B T$, at site i the spin $\vec{s}_i$ can point in q different directions $\theta_i = 2\pi n_i/q$ in the xy plane, with $n_i = 0, 1, \ldots, q-1$ providing the q different possible states, the delta function $\delta(\vec{s}_i, \vec{s}_j) = 1$ for $\vec{s}_i = \vec{s}_j$ and 0 otherwise, and the sum is over all interacting pairs of spins. We independently vary the Potts interaction strength J and the clock interaction

strength K of the merged Potts-clock model, to obtain the multistructured multicritical global phase diagram.

For even-q models (e.g., $q = 4$), at interaction ratio $J/K = -2$, a cancellation occurs between the Potts and clock terms and the energies are equal for the completely aligned ($n_i = n_j$) and completely antialigned ($|n_i - n_j| = q/2$) interacting pairs of spins. Thus, along this line on the phase diagram, all phases must be invariant under π rotation of any individual spin. Only the quadrupolar (Sivardière et al., 1973) and disordered phases are seen along this line in our calculated phase diagrams.

For odd-q models (e.g., $q = 5$), the energies are equal for the two most antialigned (but cannot be completely antialigned due to odd q) pairs of spins ($|n_i - n_j| \pm 1/2 = q/2$), so that for interactions favoring antialignment, there is a ground-state energy degeneracy. Thus, fluctuations will occur no matter how low the temperature, leading to a nonzero-temperature sink fixed point if an ordered phase occurs, making the latter algebraically ordered (Berker and Kadanoff, 1980a).

This fundamental distinction between even and odd q underlies the qualitatively different phase diagram topologies obtained in each case.

7.3 Method

The Migdal-Kadanoff approximation (Migdal, 1975; Kadanoff, 1976) renders a non-doable renormalization-group transformation doable by a physically motivated approximate step. As shown in Fig. 7.1(a), an exact renormalization-group transformation cannot be applied to the cubic lattice. Thus, as an approximation, some of the bonds are removed. The removed bonds can be compensated by adding the appropriate number of bonds to the result of the decimation, this being the number of decimated bonds that the removed bonds would have given. Alternately, a certain fraction f of the removed bonds could be compensated before decimation and the remaining fraction $1 - f$ could be compensated after the decimation. The choice of $0 \leq f \leq 1$ is left to us.

7.3.1 Hierarchical lattice equivalence

Furthermore, as shown in Figs. 7.1(b)–7.1(d), the renormalization-group recursion relations of the Migdal-Kadanoff approximation are identical to those of an exactly solved

hierarchical model (Berker and Ostlund, 1979; Griffiths and Kaufman, 1982; Kaufman and Griffiths, 1984; Berker and McKay, 1984), making the Migdal-Kadanoff approximation a physically realizable approximation, as used in polymers, electronic systems, and turbulence, respectively, in Refs. (Flory, 1986; Kaufman, 2018; Lloyd and Oglesby, 1976; Kraichnan, 1961), and therefore a robust approximation.

7.3.2 Calibration to exact results

In this chapter, our calculation corresponds to the hierarchical model in Fig. 7.1(c), with the factor f chosen so that our calculation yields the exact transition temperature of the model with $q = 2$, namely the Ising model. This choice was used previously, e.g., in the quantum mechanical renormalization-group study of high-temperature superconductivity in the t-J model of electronic conduction (Falicov and Berker, 1995; Hinczewski and Berker, 2008). Thus, the exact critical temperatures (Onsager, 1944; Talapov and Blöte, 1996) of $1/(J/2+K) = 2.26918531$ and 4.51152785 are obtained, in $d = 2$ and 3, with $f = 0.5459793$ and 0.1775492, respectively. Note that for $q = 2$, both the Potts and clock terms in Eq. (7.1) reduce to the Ising model, with combined interaction constant $J/2+K$.

7.3.3 Transfer matrix formulation

The above can be rendered algebraically in the most straightforward way by writing the transfer matrix between two neighboring spins. For example, for $q = 4$,

$$\mathbf{T}_{ij} \equiv e^{-\beta H_{ij}} = \begin{pmatrix} e^{J+K} & 1 & e^{-K} & 1 \\ 1 & e^{J+K} & 1 & e^{-K} \\ e^{-K} & 1 & e^{J+K} & 1 \\ 1 & e^{-K} & 1 & e^{J+K} \end{pmatrix}, \tag{7.2}$$

and for $q = 5$,

$$\mathbf{T}_{ij} \equiv e^{-\beta H_{ij}} = \begin{pmatrix} e^{J+K} & e^{0.31K} & e^{-0.81K} & e^{-0.81K} & e^{0.31K} \\ e^{0.31K} & e^{J+K} & e^{0.31K} & e^{-0.81K} & e^{-0.81K} \\ e^{-0.81K} & e^{0.31K} & e^{J+K} & e^{0.31K} & e^{-0.81K} \\ e^{-0.81K} & e^{-0.81K} & e^{0.31K} & e^{J+K} & e^{0.31K} \\ e^{0.31K} & e^{-0.81K} & e^{-0.81K} & e^{0.31K} & e^{J+K} \end{pmatrix}, \tag{7.3}$$

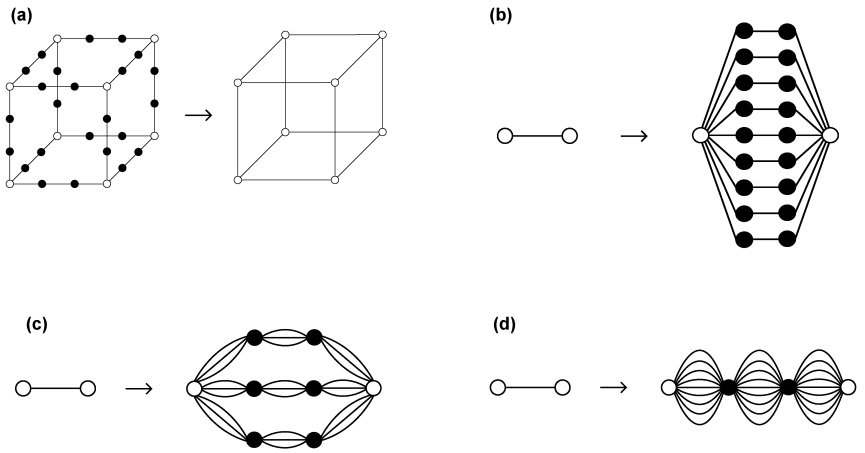


Figure 7.1: (a) The Migdal-Kadanoff approximate renormalization-group transformation on the cubic lattice. Bonds are removed from the cubic lattice to make the renormalization-group transformation doable. The removed bonds are compensated by adding them to the remaining bonds: before, after, or partially before partially after. In each of (b)–(d), a hierarchical model is constructed by self-imbedding a graph into each of its bonds, *ad infinitum* (Berker and Ostlund, 1979). The exact renormalization-group solution proceeds in the reverse direction, by summing over the internal spins shown with the dark circles. Shown in (b)–(d) are the most used, so-called diamond hierarchical lattices (Berker and Ostlund, 1979; Griffiths and Kaufman, 1982; Kaufman and Griffiths, 1984). The length-rescaling factor b is the number of bonds in the shortest path between the external spins shown with the open circles, $b = 3$ in these cases. The volume rescaling factor b^d is the number of bonds replaced by a single bond, $b^d = 27$ in these cases, so that $d = 3$. In the renormalization-group solutions, in (b), b^{d-1} bond moving is done after summing over (namely decimating) the internal spins along a length-rescaling line of b bonds. In (d), b^{d-1} bond moving is done before decimation over b bonds. In (c), the fraction f of the bond moving is done before and the remaining fraction $1-f$ is done after the decimation.

where $-\beta H_{ij}$ is the part of the Hamiltonian between the two spins at the neighboring sites i and j. An important degeneracy difference between these two transfer matrices, with important phase diagram consequences, will be discussed below.

7.3.4 Inclusion of effective vacancies

An important aspect of an occurring phase transition is the order of the phase transition. The q-state Potts models have a second-order phase transition for $q \leq q_c$ and a first-order phase transition for $q > q_c$ (Baxter, 1973; Wu, 1982; Bazavov et al., 2008). In renormalization-group theory, this has been understood and reproduced as a condensation of effective vacancies formed by regions of disorder (Nienhuis et al., 1979; Berker and Andelman, 1982).

The above has been included (Devre and Berker, 2022) as a local disorder state into the two-spin transfer matrix of Eq. (7.2). Inside an ordered region of a given spin value, a disordered site does not significantly contribute to the energy in Eq. (7.1), but has a multiplicity of $q-1$. The subtraction comes from the fact that the disordered site cannot be in the spin state of its surrounding ordered region. This is equivalent to the exponential of an on-site energy and, with no approximation, is shared on the transfer matrices of the $2d$ incoming bonds. The transfer matrix becomes, for example, for $q = 4$,

$$\mathbf{T}_{ij} = \begin{pmatrix} e^{J+K} & 1 & e^{-K} & 1 & (q-1)^{1/2d} \\ 1 & e^{J+K} & 1 & e^{-K} & (q-1)^{1/2d} \\ e^{-K} & 1 & e^{J+K} & 1 & (q-1)^{1/2d} \\ 1 & e^{-K} & 1 & e^{J+K} & (q-1)^{1/2d} \\ (q-1)^{1/2d} & (q-1)^{1/2d} & (q-1)^{1/2d} & (q-1)^{1/2d} & (q-1)^{1/d} \end{pmatrix}. \tag{7.4}$$

The renormalization-group flows, under the transformation applied here, of the transfer matrices determine the phases, the phase transitions and all of the thermodynamic densities of the system.

7.4 Results: Global Phase Diagrams

7.4.1 Overview of phase diagram structure

Phase diagram predictions can be made from the *a priori* examination of the Hamiltonian of the Potts-clock model in Eq. (7.1).

For the $q = 4$ model (and in general for all even-q Potts-clock models), for interaction ratio $J/K = -2$, a cancellation occurs between the Potts and clock terms and the energies are equal for the completely aligned ($n_i = n_j$) and completely antialigned ($|n_i - n_j| = q/2$) interacting pairs of spins. Thus, along this line on the phase diagram, all phases must be invariant under π rotation of any individual spin. In fact, only the quadrupolar (Sivardière et al., 1973) and disordered phases are seen along this line in our calculated phase diagrams (Figs. 7.2 and 7.3). Indeed, in the quadrupolar phase, the neighboring spins are, randomly, either aligned or π antialigned.

For the $q = 5$ model (and in general for all odd-q Potts-clock models), the energies are equal for the two most antialigned (but cannot be completely antialigned due to odd q) pairs of spins ($|n_i - n_j| \pm 1/2 = q/2$), so that for interactions favoring antialignment, there is a ground-state energy degeneracy. Thus, fluctuations will occur no matter how low the temperature, leading to a nonzero-temperature sink fixed point if an ordered phase occurs, making the latter algebraically ordered (Berker and Kadanoff, 1980b). This is in fact what is seen, with the algebraic antiferromagnetic and algebraic antiquadrupolar phases in our calculated phase diagrams (Figs. 7.2 and 7.3).

7.4.2 Renormalization-group sinks of the ordered phases

Under repeated renormalization-group transformations, the phase diagram points of the ordered phases of the Potts-clock model flow to the sinks shown in Table 7.1. The sink values of the transfer matrix elements epitomize the whole basin of attraction of the completely stable fixed point that is the sink.

Table 7.1: Sinks of the ordered phases. Only the top row of the sink transfer matrix is shown. The subsequent rows are obtained by cyclically rotating the elements. The last row and last column of the transfer matrix, corresponding to the effective vacancies, have all elements zero at the ordered sinks and are not given here.

Sinks of the Ordered Phases of the $(q = 4)$*-state Potts-Clock Model*	
Phase	Top Row of Sink Transfer Matrix
Antiferromagnetic	$[0,0,1,0]$
Quadrupolar	$[1,0,1,0]$
Ferromagnetic	$[1,0,0,0]$
Sinks of the Ordered Phases of the $(q = 5)$*-state Potts-Clock Model*	
Phase	Top Row of Sink Transfer Matrix
Algebraic Antiferromagnetic	$[0,1/3,1,1,1/3]$
Algebraic Antiquadrupolar	$[0,1,1/3,1/3,1]$
Ferromagnetic	$[1,0,0,0,0]$

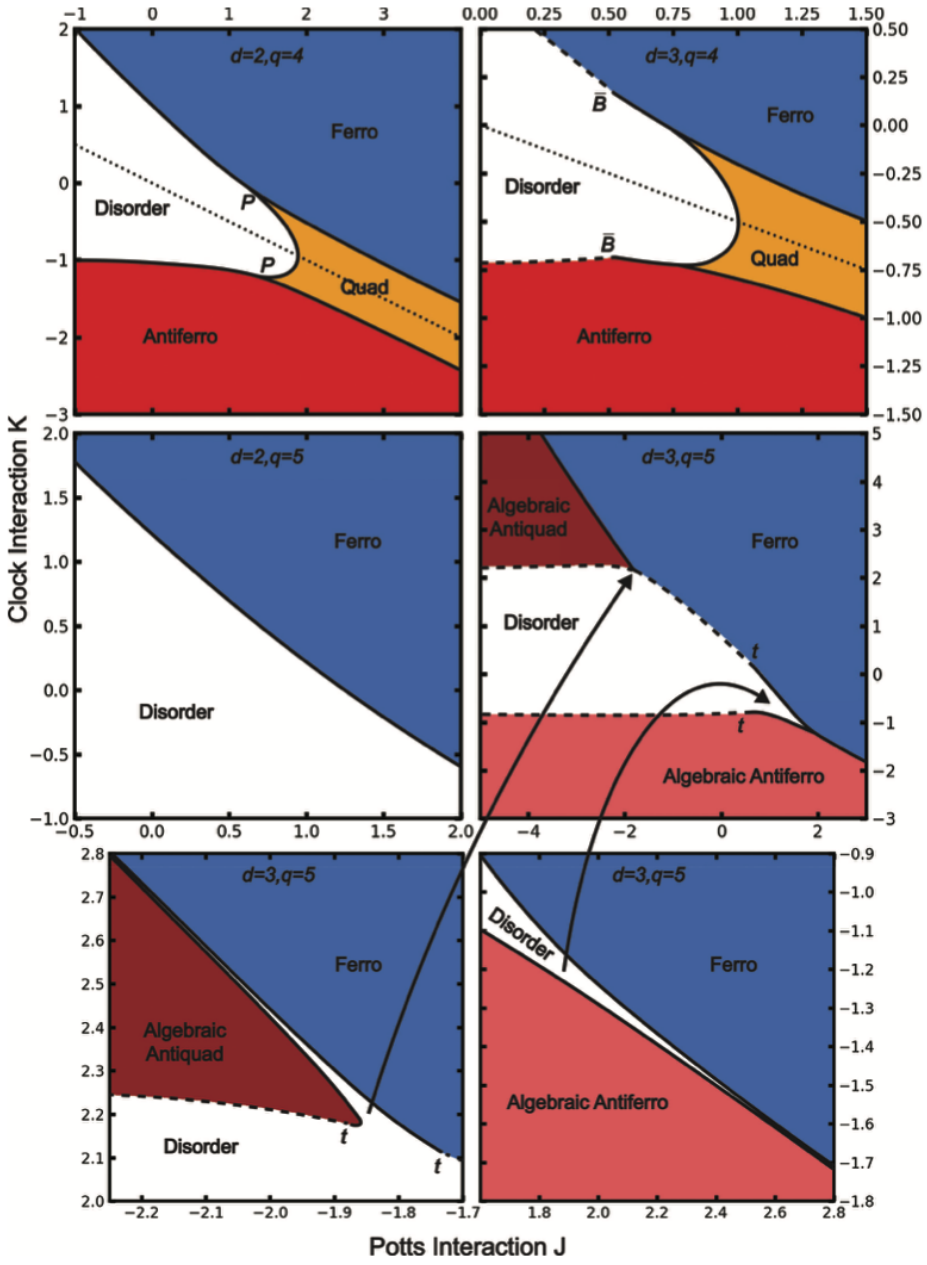


Figure 7.2: Calculated phase diagrams of the $q = 4$ and 5 state Potts-clock models in $d = 2$ and 3, in terms of the respective interactions J and K. First- and second-order phase transition lines are shown with dashed and full lines, respectively. The disorder line, occurring in $q = 4$, is shown with a dotted line. Two types (namely, bordered by different phases) of inverted (see Fig. 7.3) bicritical points B, two types of second-order bifurcation points P, three types of tricritical points t are seen. As seen in the insets (bottom two panes), the narrow disordered phase, between the algebraically ordered ferromagnetic phase or the algebraically ordered quadrupolar phase and the ferromagnetic phase, narrowly extends to two types of zero-temperature (see insets) bicritical points Z (Fig. 7.3). Both in $d = 2$ and 3, the conventionally ordered quadrupolar phase ($q = 4$) non-narrowly extends to zero-temperature highly degenerate multicritical point S, given in Fig. 7.3. Thus, a qualitatively very different picture emerges for even and odd number of states q.

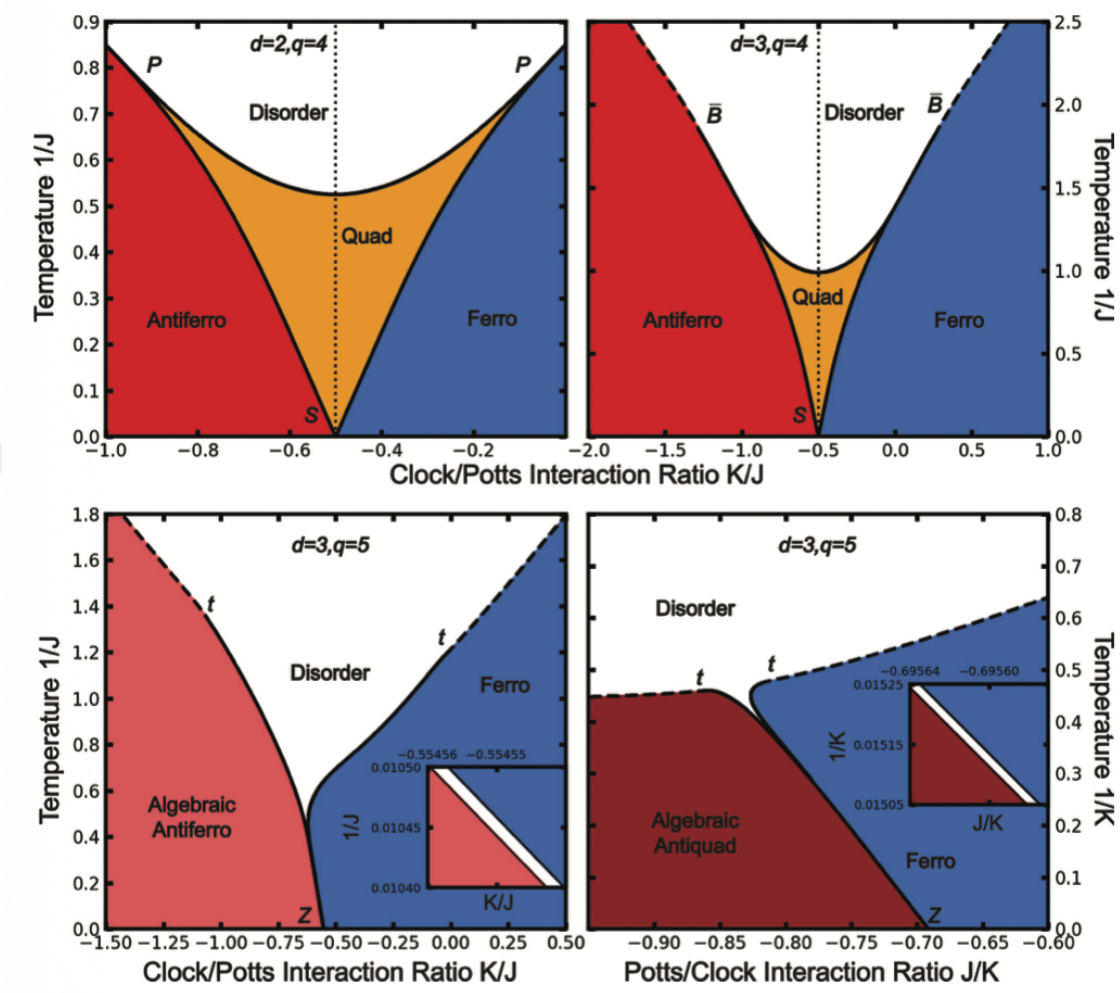


Figure 7.3: Calculated strong-coupling behaviors in $d = 2$ and $d = 3$, in terms of the temperature variables $1/J$ or $1/K$ and the ratio of the Potts-clock interactions K/J or J/K. First- and second-order phase transitions are shown with dashed and full lines, respectively. Top row: The $q = 4$ state Potts-clock models. The disorder line is shown with a dotted line. Both in $d = 2$ and 3, the conventionally ordered quadrupolar phase nonnarrowly extends to the zero-temperature highly degenerate multicritical point S. Bottom row: The $q = 5$ state Potts-clock model in $d = 3$. As also seen in the insets, the narrow disordered phase, between the algebraically ordered ferromagnetic phase or the algebraically ordered quadrupolar phase and the ferromagnetic phase, narrowly extends to two types (namely, bordered by different phases) of zero-temperature (see insets of Fig. 7.2) bicritical points Z. As also seen in Ref. (Berker and Kadanoff, 1980a,b), the algebraically ordered phases do not occur in $d = 2$. Two different types of tricritical points t occur in each pane of the figure.

In the ferromagnetic phase, the spins are aligned along one of the q spin directions. In the antiferromagnetic phase, the spins up-down alternate along a spatial direction. In the quadrupolar phase, the spins align, randomly, in a spin direction and its opposite direction. The disordered phase has two sinks: one sink with the lower-right $(q+1) \times (q+1)$ element of the transfer matrix equal to 1 and the rest zero, another sink with all elements in the upper-left $q \times q$ block equal to one and the rest zero. Analysis at the unstable fixed points attracting the phase boundaries gives the order of the phase transition (Berker et al., 1978).

7.4.3 Even-*q* systems: conventional order

For $q = 4$ (Figs. 7.2 and 7.3), ferromagnetic and antiferromagnetic phases, with intervening quadrupolar (Sivardière et al., 1973) and disordered phases, are seen. The quadrupolar phase intervenes between the ferromagnetic and antiferromagnetic phases, up to a second-order bifurcation point P in $d = 2$ and up to an inverted bicritical (Nelson et al., 1974; Hoston and Berker, 1991) point B in $d = 3$.

The bicritical points are inverted, namely, their first-order stem is on the high-temperature side (Fig. 7.3), whereas in previously studied bicritical points the first-order stem extends towards low temperature. All other phase transitions are second order.

A highly degenerate multicritical point S occurs at $1/J = 0$, $K/J = -0.5$ (Fig. 7.3), due to the degeneracy discussed at the beginning of this section. The ferromagnetic, quadrupolar, antiferromagnetic phases meet at this single zero-temperature multicritical point (Hoston and Berker, 1991) in both $d = 2$ and 3.

7.4.4 Odd-*q* systems: algebraic order from ground-state degeneracy

For $q = 5$ (Figs. 7.2 and 7.3), in $d = 3$, an algebraically ordered antiferromagnetic phase or the algebraically ordered antiquadrupolar phase and the ferromagnetic phase are separated by a narrow disordered phase terminating at a zero-temperature bicritical point Z. In both cases, at the phase boundaries at higher temperatures on each side of the phase diagram, a tricritical point t separates first- and second-order transition lines (Fig. 7.3).

In $d = 2$, second-order phase transitions separate the ferromagnetic and disordered phases. Previous work has consistently shown for both Potts (Berker and Kadanoff, 1980a) and

odd-q clock (Ilker and Berker, 2014b) models, that the algebraically ordered phases occur for $d = 3$, but not for $d = 2$, where the disordered phase persists to zero temperature.

7.4.5 Multicritical points and phase boundary structure

It is seen from Table 7.1 that the sinks of the $q = 5$ antiferromagnetic and antiquadrupolar phases have a temperature scale, namely that all elements of the sink transfer matrix are not 1 or 0. In general, at a renormalization-group fixed point, the system is scale invariant, so that the correlation length ξ is zero (at disordered or conventionally ordered phase sinks), which cannot be if there is a temperature scale, or infinity (at fixed points attracting critical systems) (Wilson, 1971a,b).

Thus, in the present case the entirety of these antiferromagnetic and antiquadrupolar phases are critical (Berker and Kadanoff, 1980a; Saleur, 1991). The correlation length ξ is infinite throughout these phases and, having no length scale, the phases are algebraically ordered.

7.4.6 Nature of the algebraically ordered phases

The algebraic phases discovered here demonstrate that symmetry competition can produce phases that exhibit properties characteristic of scale invariance as a complexity generator. The ground-state degeneracy in odd-q systems creates a situation where fluctuations persist to arbitrarily low temperatures, preventing the system from flowing to a conventional ordered sink. Instead, the RG attractor is a fixed line characterized by a nonzero temperature scale.

7.4.7 Limiting Cases: pure Potts and pure clock

For $K = 0$ and $J = 0$, the model reduces to the Potts and clock models, respectively.

For $q = 4$ (Figs. 7.2 and 7.3), the expected second-order phase transitions are seen for both Potts and clock models in $d = 2$, but in $d = 3$ the expected Potts first-order phase transition is narrowly missed in the proximity of a bicritical point.

For $q = 5$ (Figs. 7.2 and 7.3), the expected first-order phase transition is not seen for Potts in $d = 2$, and the expected Potts first-order phase transition is narrowly missed, in the

proximity of a tricritical point, in $d = 3$. Similarly, in $d = 2$, the narrow intermediate BKT phase (Polackova and Gendiar, 2023) is missed for the clock model.

7.5 Discussion: Symmetry Competition Generates Phase Complexity

This chapter demonstrates symmetry competition as a complexity generator in action. The key observations are: A simple Hamiltonian with only two coupling constants (J, K) generates six distinct thermodynamic phases. This is more than either the pure Potts model (2 phases: ordered, disordered) or the pure clock model (2–3 phases depending on d and q) produces alone. The competition between Potts and clock symmetries creates a rich network of multicritical points—inverted bicritical, zero-temperature bicritical, tricritical, second-order bifurcation, and zero-temperature highly degenerate multicritical points. In odd-q systems, the ground-state degeneracy inherent in the clock term (when favoring antialignment) creates algebraically ordered phases with infinite correlation length throughout. The phase diagram topology depends qualitatively on the parity of q, demonstrating how discrete symmetry properties propagate through the RG to determine macroscopic behavior.

7.5.1 Comparison with frustrated systems

Table 7.2: Comparison of frustration-driven complexity (Chs. 3–6) and symmetry-competition-driven complexity (Ch. 7).

Property	**Frustration (Chs. 3–6)**	**Symmetry Competition (Ch. 7)**
Phase count from two couplings	4–5 (F, AF, SG, D, nematic)	6 (F, Q, AF, Alg-AF, Alg-AQ, D)
Chaos in RG	Yes	No
Algebraic order	No	Yes (odd q)
Multicritical points	Special point M (Ch. 6)	Multiple types (B, P, t, Z, S)
Order type	Unsaturated ($y_R < d-1$)	Both saturated and critical
Requires disorder	Yes	No

The comparison reveals that symmetry competition and frustration are complementary complexity generators. Frustration produces chaotic flows and unsaturated order; symmetry competition produces multiple well-defined phases with algebraic order possible in clean systems.

7.5.2 The role of ground-state degeneracy

The contrast between even-q and odd-q systems highlights a key principle: microscopic degeneracy structure determines macroscopic phase topology.

Even q: Complete antialignment is possible ($|n_i - n_j| = q/2$), leading to a unique antiferromagnetic ground state. The system can flow to a conventional ordered sink with $\xi = 0$.

Odd q: Complete antialignment is impossible (no integer $|n_i - n_j|$ equals $q/2$), creating ground-state degeneracy between the two "most antialigned" configurations. Fluctuations persist to zero temperature, the system cannot reach a conventional ordered sink, and algebraic order results (Berker and Kadanoff, 1980a).

This mechanism—ground-state degeneracy preventing flow to conventional sinks—is a precursor to the fixed-line structure that will be fully developed in Chapter 8 for continuous-spin systems.

7.6 Conclusion

The much-used Potts models and clock spin models have been merged into a simple but complex Potts-clock model and solved by renormalization-group theory. The resulting global phase diagram contains a disordered phase and five different ordered phases, namely conventionally ordered ferromagnetic, quadrupolar, and antiferromagnetic phases; algebraically ordered antiferromagnetic and antiquadrupolar phases.

These six different phases are separated by first- and second-order phase boundaries, themselves delimited by multicritical points: inverted bicritical, zero-temperature bicritical, tricritical, second-order bifurcation, and zero-temperature highly degenerate multicritical points. A rich sequence of phase diagram topologies is thus obtained from a simple model.

This chapter demonstrates symmetry competition generating complexity. Competition between Potts and clock symmetries produces richer phase diagrams than either alone. The even/odd asymmetry shows how microscopic degeneracy structure determines macroscopic topology: ground-state degeneracy in odd-q systems prevents flow to conventional sinks, producing algebraic order. The algebraic phases found here with their nonzero tem-

perature sinks are discrete-spin precursors to the fixed lines of potential surfaces that will characterize the continuous-spin XY-Ashkin-Teller model in Chapter 8.

8. ALGEBRAIC PHASES IN THE *XY*-ASHKIN-TELLER MODEL

8.1 Introduction

8.1.1 Algebraic order and the absence of length scale

A distinctive low-temperature phase, which actually is a continuously varying continuum of critical points, with the absence of length scale, is seen in spatial dimension $d = 2$ in the XY model (Berezinskii, 1970; Kosterlitz and Thouless, 1973; Halperin and Nelson, 1978; Nelson and Halperin, 1979; Berker and Kadanoff, 1980a; Saleur, 1991),

$$-\beta\mathscr{H} = \sum_{\langle ij \rangle} J\,\vec{s}_i \cdot \vec{s}_j, \tag{8.1}$$

where $\beta = 1/k_B T$ is the inverse temperature, at each site i there is an XY unit spin $\vec{s}_i$ that can point in an angle between 0 and 2π, and the sum is over all pairs of spins on nearest-neighbor sites.

On the other hand, the conventional Ashkin-Teller model (Ashkin and Teller, 1943; Ditzian et al., 1980; Keçoğlu and Berker, 2023) is a doubled-up progeny of the up-down discrete-spin Ising model, ushering a multiplicity of order parameters and ordered phases from this discrete-spin model. Using continuously orientable XY spins instead of discrete Ising spins, with the algebraic ordering of $d = 2$, brings a multiplicity of algebraic orders. This XY Ashkin-Teller model is defined by the Hamiltonian

$$\begin{aligned} -\beta\mathscr{H} &= \sum_{\langle ij \rangle} \left[J\left(\vec{s}_i \cdot \vec{s}_j + \vec{t}_i \cdot \vec{t}_j\right) + M\left(\vec{s}_i \cdot \vec{s}_j\right)\left(\vec{t}_i \cdot \vec{t}_j\right) \right] \\ &= \sum_{\langle ij \rangle} -\beta H_{ij}\left(\vec{s}_i, \vec{t}_i; \vec{s}_j, \vec{t}_j\right), \end{aligned} \tag{8.2}$$

where at each site i there are two XY unit spins $\vec{s}_i, \vec{t}_i$ that can point in an angle between 0 and 2π, and the sum is over all interacting quadruples of spins on nearest-neighbor pairs of sites.

A thermodynamic phase with algebraic order (Berezinskii, 1970; Kosterlitz and Thouless, 1973; Halperin and Nelson, 1978; Nelson and Halperin, 1979; Berker and Kadanoff, 1980a; Saleur, 1991) does not have a nonzero order parameter such as a magnetization, but is characterized by long-range algebraically decaying correlations, such as a spin-spin correlation function, as opposed to an exponentially decaying correlation function. The algebraically ordered phase has no physical length scale (therefore no exponentially decaying correlation function, since there is no physical length to divide the length variable in the exponent).

In fact, an algebraically ordered phase can be seen as a continuum of critical points, with continuously varying critical exponents (resulting from a renormalization-group fixed line), or uniform critical exponents (resulting from a finite-temperature phase-sink fixed point). Algebraically ordered phases occur: in $d = 2$, in XY spin systems, solids, liquid crystals (Berezinskii, 1970; Kosterlitz and Thouless, 1973; Halperin and Nelson, 1978; Nelson and Halperin, 1979) and, in a variety of d, in antiferromagnetic Potts models (Berker and Kadanoff, 1980a; Saleur, 1991).

8.1.2 The Ashkin-Teller construction with continuous spins

This chapter represents the culmination of the symmetry competition theme and provides the fullest realization of scale invariance in this thesis. The XY spins can point in any direction, invoking the Mermin–Wagner theorem and enabling algebraic order in $d = 2$. Unlike the discrete-spin models of previous chapters, where fixed points are characterized by finite transfer matrices, here the RG attractors are continuous manifolds of potential surfaces in function space, producing continuously varying critical exponents throughout entire thermodynamic phases.

8.2 Quasi-Disorder Lines

Before proceeding to the solution, we note an important structural feature of the model that constrains the phase diagram topology.

Considering the aligned and antialigned spin states, also as representatives for continuous deviations from these states, on the semi-infinite line $M = J < 0$, 12 of the 16 possible states of $(\vec{s}_i, \vec{t}_i, \vec{s}_j, \vec{t}_j)$ have the lowest interaction energy $\beta H = J < 0$, whereas the other four states have energy $\beta H = -3J > 0$, with a gap of $4J$. These four states contribute less

and less as temperature is lowered (i.e., as $|J|$ is increased).

Thus, on the $J = M < 0$ semi-infinite line, there is a 12-fold ground-state degeneracy and this line is a quasi-disorder line: If all 16 spin states had the same energy, no ordering would occur in this totally degenerate system. Nevertheless, in the current situation of 12 degenerate ground states and 4 less participating high-energy states, the lack of ordering can be anticipated. Thus we call this semi-infinite line a quasi-disorder line (Keçoğlu and Berker, 2023) and, in fact, no ordering occurs, as seen below.

The same happens along the semi-infinite line $-M = J > 0$, which is therefore also a quasi-disorder line. We shall see that the disordered phase hugs these two quasi-disorder lines all the way to infinite interactions, i.e., zero temperature.

8.3 Renormalization-Group Method

8.3.1 Double Fourier representation

The renormalization-group transformation, explained in Fig. 8.1, is done with length rescaling factor $b = 3$, an odd number in order to conserve the ferromagnetic-antiferromagnetic symmetry of the method (van Leeuwen, 1975). The approximate solution on the $d = 2$ square lattice is, simultaneously, an exact solution on the $d = 2$ hierarchical lattice (Berker and Ostlund, 1979; Griffiths and Kaufman, 1982; Kaufman and Griffiths, 1984; Berker and McKay, 1984). The simultaneous exact solution makes the approximate solution a physically realizable, therefore robust approximation.

As seen in Fig. 8.1, the first step of the renormalization-group transformation involves decimation over three consecutive bonds. A decimated bond is obtained by integrating over the shared two spins of two bonds. With $u_{ij}(\theta_{ij},\phi_{ij}) = e^{-\beta H_{ij}(\vec{s}_i,\vec{t}_i;\vec{s}_j,\vec{t}_j)}$ being the exponentiated nearest-neighbor Hamiltonian between sites (i,j), and $\theta_{ij} = \theta_i - \theta_j$ and $\phi_{ij} = \phi_i - \phi_j$ being the angles between the planar unit vectors $(\vec{s}_i,\vec{s}_j)$ and $(\vec{t}_i,\vec{t}_j)$, decimation proceeds as

$$\tilde{u}_{13}(\theta_{13},\phi_{13}) = \int_0^{2\pi} u_{12}(\theta_{12},\phi_{12})\, u_{23}(\theta_{23},\phi_{23})\, \frac{d\theta_2}{2\pi}\frac{d\phi_2}{2\pi}. \tag{8.3}$$

On the left side of this equation, the tilde means decimated.

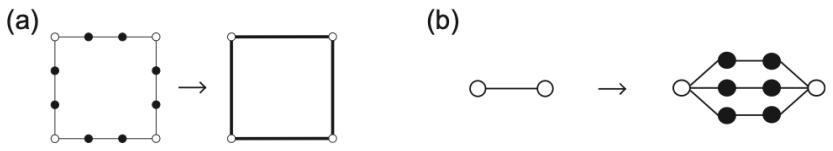


Figure 8.1: Exact solution of the $d = 2$ hierarchical model and Migdal-Kadanoff: (a) The Migdal-Kadanoff approximate renormalization-group transformation on the square lattice. Bonds are removed from the square lattice to make the renormalization-group transformation doable. The removed bonds are compensated by adding their effect to the decimated remaining bonds. (b) A hierarchical model is constructed by self-imbedding a graph into each of its bonds, *ad infinitum* (Berker and Ostlund, 1979). The exact renormalization-group solution proceeds in the reverse direction, by summing over the internal spins shown with dark circles. Here is the most used, so-called "diamond" hierarchical lattice (Berker and Ostlund, 1979; Griffiths and Kaufman, 1982; Kaufman and Griffiths, 1984; Berker and McKay, 1984). The length-rescaling factor b is the number of bonds in the shortest path between the external spins shown with the open circles ($b = 3$ in this case). The volume rescaling factor b^d is the number of bonds replaced by a single bond ($b^d = 9$ in this case), so that $d = 2$.

Using a double Fourier transformation,

$$f(k,l) = \int_0^{2\pi}\int_0^{2\pi} u(\theta,\phi)\, e^{ik\theta+il\phi}\, \frac{d\theta}{2\pi}\frac{d\phi}{2\pi}, \tag{8.4}$$

$$u(\theta,\phi) = \sum_{k=-\infty}^{\infty}\sum_{l=-\infty}^{\infty} e^{-ik\theta-il\phi}\, f(k,l), \tag{8.5}$$

the decimation of Eq. (8.3) becomes

$$\tilde{f}_{13}(k,l) = f_{12}(k,l)\, f_{23}(k,l), \tag{8.6}$$

where $f_{ij}(k,l)$ are the Fourier coefficients for the interaction between sites i and j.

As also seen in Fig. 8.1, the second step of the renormalization-group transformation involves bond moving three bonds. Bond moving bonds $(i_1 j_1)$ and $(i_2 j_2)$ to obtain bond (ij) is effected as

$$u'_{ij}(\theta,\phi) = \tilde{u}_{i_1 j_1}(\theta,\phi)\, \tilde{u}_{i_2 j_2}(\theta,\phi), \tag{8.7}$$

$$f'_{ij}(k,l) = \sum_{m=-\infty}^{\infty}\sum_{n=-\infty}^{\infty} \tilde{f}_{i_1 j_1}(k-m,l-n)\, \tilde{f}_{i_2 j_2}(m,n). \tag{8.8}$$

On the left side of this equation, the prime means bond moved.

8.3.2 Numerical implementation

We have followed the renormalization-group flows in terms of the $k = 0$ to 20 and $l = 0$ to 20 double Fourier components, thus having 441 renormalization-group flow quantities, and also using the symmetries $f_{ij}(k,l) = f_{ij}(-k,l) = f_{ij}(k,-l) = f_{ij}(-k,-l)$. We also made spot checks with a higher number of double Fourier components (up to $k,l = 0$ to 100). The spot checks have yielded no differences to the accuracy of the thickness of the lines in our figures. This is also the case in Refs. (Kosterlitz and Thouless, 1973; Halperin and Nelson, 1978).

We set to unity the maximum value of the double Fourier components, by dividing with the same constant (the raw maximal value), which amounts to adding the same constant to all energies.

8.4 Phase Diagram and Fixed Lines

The phase diagram (Fig. 8.2) is obtained by following the renormalization-group flows of the double Fourier coefficients $f(k,l)$, obtained as described above, respectively to their stable fixed lines and stable fixed point (D), namely, sinks. The basin of attraction of each sink is a corresponding thermodynamic phase (Berker and Wortis, 1976). In this XY-Ashkin-Teller model, there are five sinks and therefore five distinct thermodynamic phases.

The five phases are:

- Ferromagnetic phase F: both $\vec{s}$ and $\vec{t}$ spins order ferromagnetically.
- Antiferromagnetic phase A: both $\vec{s}$ and $\vec{t}$ spins order antiferromagnetically.
- Locked ferromagnetic phase F_σ: the composite variable $\vec{s}\cdot\vec{t}$ orders ferromagnetically.
- Locked antiferromagnetic phase A_σ: the composite variable orders antiferromagnetically.
- Disordered phase D: no long-range order.

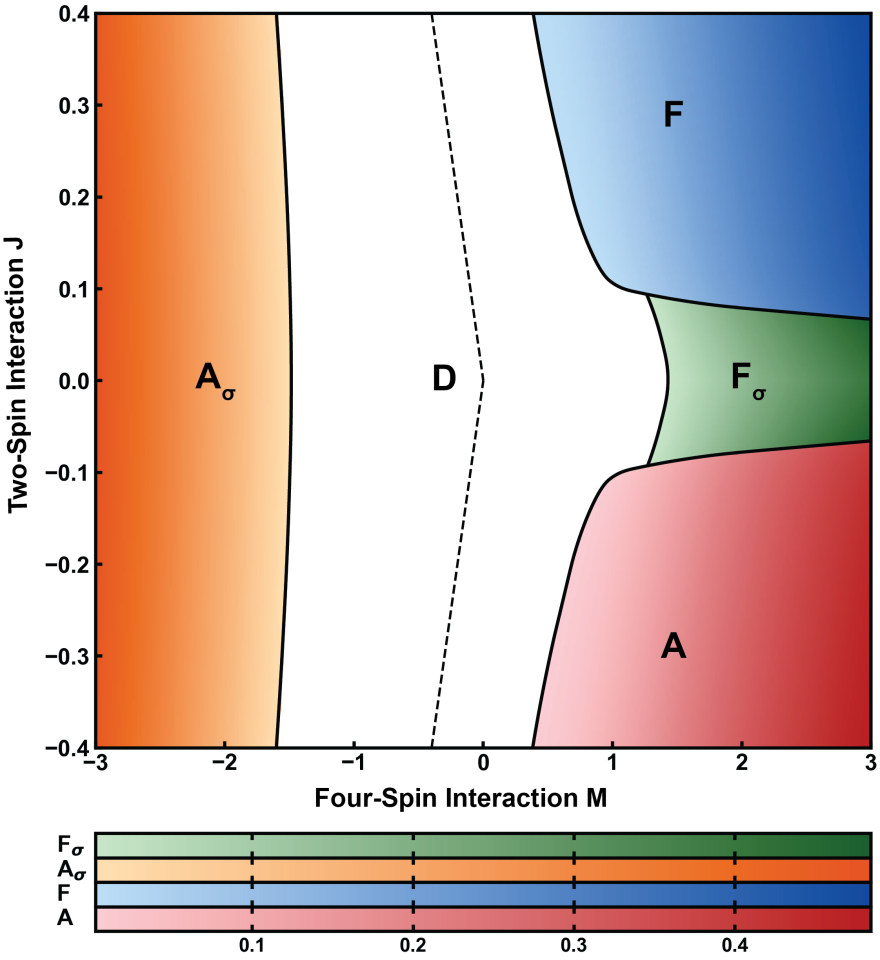


Figure 8.2: Calculated phase diagram of the XY Ashkin-Teller model in spatial dimension $d = 2$. The ferromagnetic (F) and antiferromagnetic (A) phases of the continuously orientable spin variables $\vec{s}_i$ and $\vec{t}_i$, the ferromagnetic (F_σ) and antiferromagnetic (A_σ) phases of the composite spin variable $\vec{s}_i\vec{t}_i$, and the disordered phase (D) are shown. The color intensity shows the continuously varying criticality of the algebraically ordered phases, by the mechanism of trajectories starting at different points in the phase diagram reaching different points on the fixed line. The dashed semi-infinite lines show the *a priori* quasi-disorder lines. The disordered phase D hugs the quasi-disorder lines all the way to infinite-strength interactions, namely, zero temperature.

The color intensity in Fig. 8.2 shows the continuously varying criticality of the algebraically ordered phases, by the mechanism of trajectories starting at different points in the phase diagram reaching different points on the fixed line.

The critical exponents are evaluated by calculating the derivative matrix of the renormalization-group recursion matrix. In this case, this would be the recursion of the Fourier coefficients. Such a determination, done at various points on the fixed line, yields continuously varying critical exponents (Kosterlitz and Thouless, 1973). Thus, the color intensity indicates the numerical value of, taken for example, the double Fourier coefficient $f(2,2)$ of the final destination, on the fixed line, of the renormalization-group trajectory starting at the phase diagram point.

The dashed semi-infinite lines in Fig. 8.2 show the *a priori* quasi-disorder lines. The disordered phase D hugs the quasi-disorder lines all the way to infinite-strength interactions, namely, zero temperature. This is a striking feature of the phase diagram: disorder persists to $T = 0$ along these special lines, despite the presence of strong interactions.

8.5 Fixed Lines of Potential Surfaces

8.5.1 Factorization at the fixed lines

The sinks of the renormalization-group flows, for the four ordered phases (Fig. 8.2) in this system, are fixed lines of potential surfaces that are determined by the terminal fixed values of the double Fourier coefficients $f(k,l)$.

At the ordered sinks (but not in the flows leading to the sinks), the double Fourier coefficient factorizes. This factorization is the mathematical signature of the algebraic ordering.

Ferromagnetic phase F:

$$f(k,l) = f(k)\, f(l), \tag{8.9}$$

where $f(k)$ are the Fourier coefficients at the ferromagnetic sink of a single XY model, given in the left panel of Fig. 8.3.

Antiferromagnetic phase A:

$$f(k,l) = f^A(k)\, f^A(l), \tag{8.10}$$

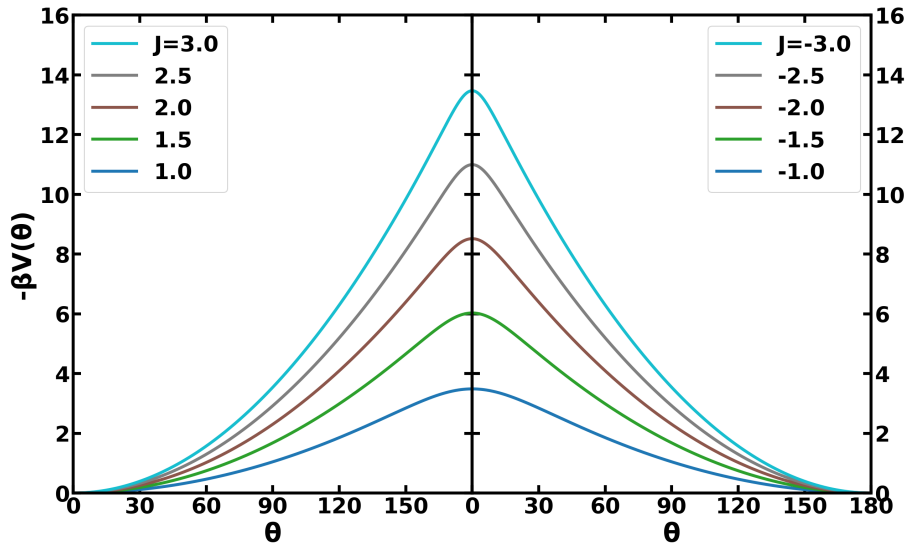


Figure 8.3: Renormalization-group trajectory terminal energy functions in the algebraically ordered phases of the single XY model, in the ferromagnetic (left panel) and antiferromagnetic (right panel) phases. The negative logarithm $\beta V(\theta) = -\ln(u)$ of the multiply renormalized exponentiated nearest-neighbor energy $u_{XY} = e^{-\beta H_{ij}(\vec{s}_i,\vec{s}_j)}$ is shown, as an energy, as a function of the angle θ between the spins $\vec{s}_i$, $\vec{s}_j$. For each energy curve, the starting spin-spin coupling J is indicated, from top to bottom. The continuum of such curves constitutes the fixed-line sink (Berker and Wortis, 1976) of the algebraically ordered phase.

where $f^A(k) = (-1)^k f(k)$ are the Fourier coefficients at the antiferromagnetic fixed-line sink of a single XY model, given in the right panel of Fig. 8.3.

Locked ferromagnetic phase F_σ:

$$f(k,l) = f_L(k)\, f_L(l), \tag{8.11}$$

where $f_L(k)$ are the Fourier coefficients of the ferromagnetic coupling between combination neighboring angles $(\theta_{ij} + \phi_{ij})/2$.

Locked antiferromagnetic phase A_σ:

$$f(k,l) = f_L^A(k)\, f_L^A(l), \tag{8.12}$$

where $f_L^A(k)$ are the Fourier coefficients of the antiferromagnetic coupling between combination neighboring angles $(\theta_{ij} - \phi_{ij})/2$.

This factorization, and the factorizations given above, only occur at the fixed surfaces,

but not in the renormalization-group flows from any system with $M \neq 0$. The factorization emerges as the system flows to the fixed line—it is an emergent property of the RG attractor.

8.5.2 Physical interpretation of the fixed-line sinks

The potential functions resulting from these double Fourier coefficients are shown in Figs. 8.3–8.5.

Ferromagnetic phase F: At the sink, the $\vec{s}_i$ spins are aligned ($\theta_{ij} = 0$) with each other and separately the $\vec{t}_i$ spins are aligned ($\phi_{ij} = 0$) with each other.

Antiferromagnetic phase A: At the sink, the neighboring $\vec{s}_i$ spins are antialigned ($\theta_{ij} = \pi$) with each other and separately the neighboring $\vec{t}_i$ spins are antialigned ($\phi_{ij} = \pi$) with each other.

Locked ferromagnetic phase F_σ: At the sink, the neighboring spins satisfy $\vec{s}_i = \pm\vec{s}_j$ and simultaneously $\vec{t}_i = \pm\vec{t}_j$, the upper (or lower) signs being jointly valid, $\theta_{ij}, \phi_{ij} = 0$ or π.

Locked antiferromagnetic phase A_σ: At the sink, neighboring $(\vec{s}_i, \vec{s}_j)$ and $(\vec{t}_i, \vec{t}_j)$ are either respectively aligned and antialigned, or respectively antialigned and aligned.

8.5.3 Entropy and degeneracy structure

The latter two ordered phases (F_σ and A_σ) have an entropy per bond $S/N = \ln 2$. This entropy arises from the discrete choice between the two "locked" configurations at each bond.

Furthermore, in all four ordered phases, the relative orientation of the $\vec{s}_i$ and $\vec{t}_i$ systems has a global degeneracy of 2π. This continuous degeneracy reflects the fact that while the $\vec{s}$ and $\vec{t}$ systems each order internally, there is no energetic preference for their relative global orientation.

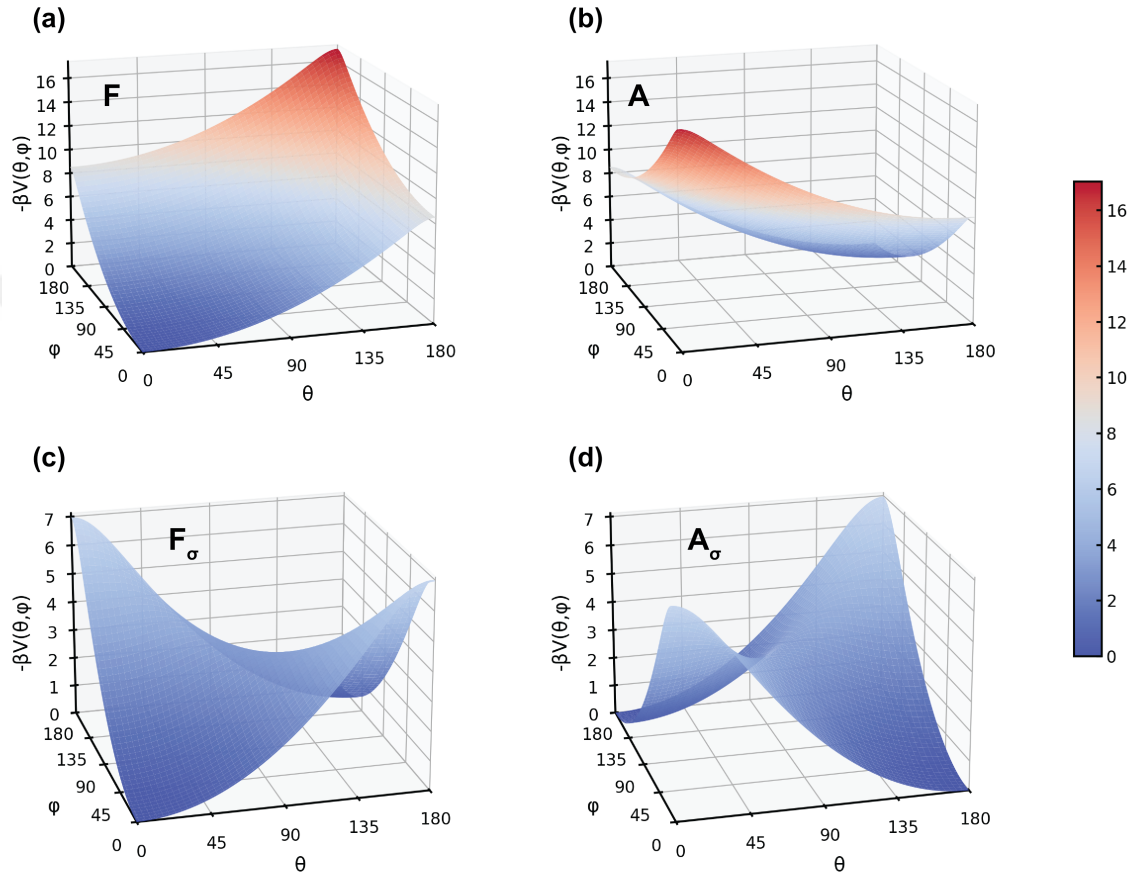


Figure 8.4: Potential functions on the fixed lines of the renormalization-group sinks of the (a) ferromagnetic phase F, (b) antiferromagnetic phase A, (c) locked ferromagnetic phase F_σ, and (d) locked antiferromagnetic phase A_σ of the XY Ashkin-Teller model. The potential function, namely, the negative logarithm $\beta V(\theta,\phi) = -\ln(u)$ of the exponentiated nearest-neighbor energy $u = e^{-\beta H_{ij}(\vec{s}_i,\vec{t}_i;\vec{s}_j,\vec{t}_j)}$ is shown, as a function of the angle θ between the spins $\vec{s}_i$, $\vec{s}_j$ and the angle ϕ between the spins $\vec{t}_i$, $\vec{t}_j$. The starting couplings of the renormalization-group trajectories leading to these potentials are $(J,M) = (2,1)$, $(-2,1)$, $(0.02,2)$, and $(0.1,-2)$ for (a), (b), (c), and (d), respectively.

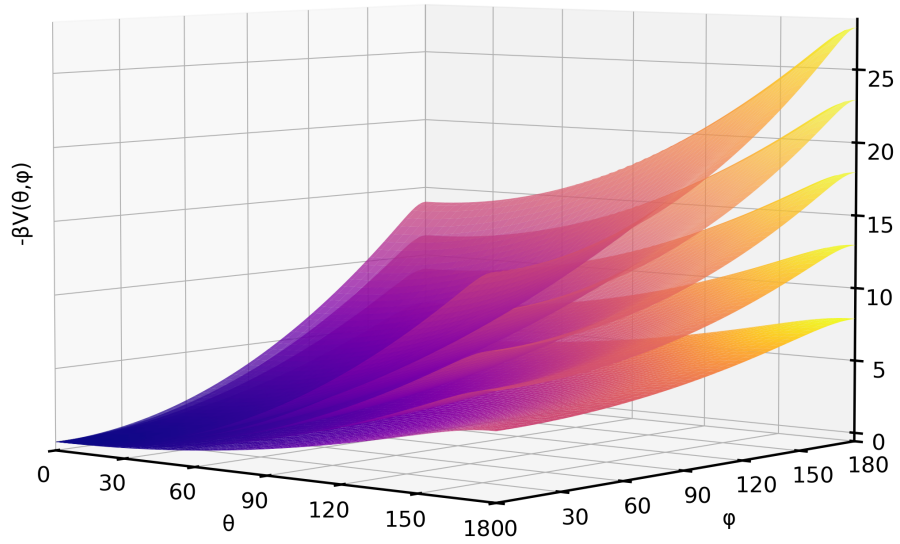


Figure 8.5: Examples of potential functions on the fixed line of the renormalization-group sink of the ferromagnetic phase F, $\beta V(\theta,\phi) = -\ln(u)$ of the exponentiated nearest-neighbor energy $u = e^{-\beta H_{ij}(\vec{s}_i,\vec{t}_i;\vec{s}_j,\vec{t}_j)}$. The various fixed energy surfaces are reached from different initial couplings (J,M). In this figure, from bottom to top, the initial couplings are $(J,M) = (1,0.1)$, $(1.5,0.1)$, $(2,0.1)$, $(2.5,0.1)$, and $(3,0.1)$.

8.5.4 The disordered phase sink

The sink of the disordered phase D has the $(0,0)$ double Fourier coefficient equal to unity; all other double Fourier coefficients are equal to zero. Therefore,

$$u_{ij}(\theta_{ij},\phi_{ij}) = e^{-\beta H_{ij}(\vec{s}_i,\vec{t}_i;\vec{s}_j,\vec{t}_j)} = 1, \tag{8.13}$$

and $\beta V(\theta,\phi) = 0$ independent of angle. This is the unique fixed point (not a fixed line) in the system—disorder corresponds to complete loss of angular preference.

8.6 Continuously Varying Critical Exponents

8.6.1 Single *XY* model fixed line

Figure 8.3 shows the renormalization-group trajectory terminal energy functions in the algebraically ordered phases of the single XY model, in the ferromagnetic (left panel) and antiferromagnetic (right panel) phases. The negative logarithm $\beta V(\theta) = -\ln(u)$ of the multiply renormalized exponentiated nearest-neighbor energy $u_{XY} = e^{-\beta H_{ij}(\vec{s}_i;\vec{s}_j)}$ is

shown, as an energy, as a function of the angle θ between the spins $\vec{s}_i$, $\vec{s}_j$.

For each energy curve, the starting spin-spin coupling J is indicated. The continuum of such curves constitutes the fixed-line sink (Berker and Wortis, 1976) of the algebraically ordered phase. Different initial coupling strengths flow to different points on the fixed line, and these different terminal points correspond to different critical exponents.

8.6.2 *XY*-Ashkin-Teller fixed surfaces

Figure 8.4 shows the potential functions on the fixed lines of the renormalization-group sinks of all four ordered phases. The potential function, namely, the negative logarithm $\beta V(\theta,\phi) = -\ln(u)$ of the exponentiated nearest-neighbor energy $u = e^{-\beta H_{ij}(\vec{s}_i,\vec{t}_i;\vec{s}_j,\vec{t}_j)}$ is shown, as a function of the angle θ between the spins $\vec{s}_i$, $\vec{s}_j$ and the angle ϕ between the spins $\vec{t}_i$, $\vec{t}_j$.

The starting couplings of the renormalization-group trajectories leading to these potentials are: $(J,M) = (2,1)$ for ferromagnetic phase F, $(J,M) = (-2,1)$ for antiferromagnetic phase A, $(J,M) = (0.02,2)$ for locked ferromagnetic phase F_σ, and $(J,M) = (0.1,-2)$ for locked antiferromagnetic phase A_σ.

8.6.3 Variation along the fixed line

Figure 8.5 shows examples of potential functions on the fixed line of the renormalization-group sink of the ferromagnetic phase F. The various fixed energy surfaces are reached from different initial couplings (J,M). From bottom to top, the initial couplings are $(J,M) = (1,0.1)$, $(1.5,0.1)$, $(2,0.1)$, $(2.5,0.1)$, and $(3,0.1)$.

This figure demonstrates the key feature of the fixed line: different starting points in the phase diagram flow to different points on the fixed line, yielding different potential surfaces and hence different critical exponents. The entire phase is critical, but the nature of the criticality varies continuously across the phase.

8.7 Discussion: The Richest Form of Scale Invariance

This chapter demonstrates the most complex form of the RG attractor structure encountered in this thesis (a comparison of RG attractor structures across chapters can be seen in

Table 8.1):

Table 8.1: Attractor structures encountered across the thesis. The XY-Ashkin-Teller ordered phases are governed by fixed lines of potential surfaces, i.e., infinite-dimensional attractors in the space of coupling functions.

Attractor Type	Dimension	Example	Chapter
Fixed point	0	Ferromagnetic sink	2
Fixed point with temperature scale	0	Algebraic AF (discrete)	7
Chaotic attractor	Fractal	Spin-glass phase	3–6
Fixed line of surfaces	∞	XY-Ashkin-Teller phases	8

The fixed lines of potential surfaces represent infinite-dimensional attractors in the space of coupling functions. This is the highest-dimensional attractor structure in the thesis and produces the most complex form of emergent behavior: continuously varying critical exponents throughout entire thermodynamic phases.

8.7.1 Generators and modulators in the XY-Ashkin-Teller model

Symmetry competition: The competition between direct ordering (J term) and composite ordering (M term) generates four distinct phases where either the individual spins or the composite spin variable orders.

Scale invariance: The continuous XY symmetry in $d = 2$ forbids conventional long-range order (Mermin–Wagner theorem), but allows algebraic order. The fixed lines are the mathematical realization of this scale invariance.

Interplay: The combination of symmetry competition and scale invariance produces the richest structure: multiple types of algebraic order, each with its own fixed line of continuously varying criticality.

8.7.2 Comparison with discrete-spin systems

The structure of the phase diagram (five phases) is identical, but the nature of the ordered phases is fundamentally different: conventional versus algebraic order. Table 8.2 shows a comparison of the discrete and continuous Ashkin-Teller constructions.

Table 8.2: Comparison of discrete and continuous Ashkin-Teller constructions. The phase labels coincide, but the ordered phases in the XY case are algebraic and controlled by fixed lines rather than isolated fixed points.

Property	Ising-Ashkin-Teller	XY-Ashkin-Teller
Spin variables	$s_i, t_i = \pm 1$	$\vec{s}_i, \vec{t}_i \in S^1$
Phases	F, A, F_σ, A_σ, D	F, A, F_σ, A_σ, D
Order type	Conventional	**Algebraic**
RG attractor	Fixed points	**Fixed lines**
Critical exponents	Fixed	**Continuously varying**
Dimension	$d \geq 2$	$d = 2$

8.7.3 The factorization phenomenon

The factorization of the double Fourier coefficients at the fixed lines [Eqs. (8.9)–(8.12)] is a remarkable emergent property. Starting from a general interaction with $M \neq 0$, the RG flow does not preserve factorization—the $f(k,l)$ do not factor during the flow. But at the fixed line, factorization emerges:

$$f(k,l) \xrightarrow{\text{RG flow}} f^*(k)\, f^*(l). \tag{8.14}$$

8.7.4 Quasi-disorder lines and zero-temperature disorder

The persistence of the disordered phase along the quasi-disorder lines to $T = 0$ is a striking feature not usually seen in simpler models. It arises from the high degeneracy (12-fold) along these special lines, which prevents ordering even at zero temperature (Keçoğlu and Berker, 2023).

This is related to but distinct from the phenomena in frustrated systems (Chapters 3–6): in spin glasses, disorder arises from quenched randomness and leads to chaotic RG flows; here, disorder arises from high intrinsic degeneracy and the disordered fixed point remains stable along special lines in the clean system.

8.8 Conclusion

We have solved, by renormalization-group theory, the Ashkin-Teller type doubled-up XY magnetic spin model in spatial dimension $d = 2$. We find four different ordered phases, with ferromagnetic and antiferromagnetic orderings of the direct and composite spins.

All four ordered phases have algebraic order, subtended by renormalization-group fixed lines of potential surfaces. The disordered phase occurs around two semi-infinite *a priori* quasi-disorder lines, down to zero temperature (infinite coupling).

This chapter demonstrates the richest form of complexity: fixed lines of potential surfaces represent infinite-dimensional attractors, producing continuously varying critical exponents throughout phases. The factorization at fixed lines is an emergent property absent during the flow—a dramatic example of attractor structure having symmetries absent in the approach to it.

Chapters 7 and 8 together complete the demonstration of symmetry competition as a complexity generator: Chapter 7 showed that competition between Potts and clock symmetries generates five ordered phases in a discrete-spin system, with algebraic order appearing for odd q due to ground-state degeneracy. Chapter 8 showed that competition between direct and composite ordering in a continuous-spin system generates four algebraically ordered phases, each subtended by fixed lines with continuously varying criticality. Together, these chapters establish that symmetry competition is a powerful generator of complexity, capable of producing multiple distinct thermodynamic phases, both conventional and algebraic order, rich multicritical structure, and continuously varying critical behavior. This completes the treatment of symmetry competition as a complexity generator and provides the fullest realization of scale invariance as a complexity generator in the thesis. The subsequent chapters will turn to interaction range as a complexity modulator, demonstrating how long-range interactions modify the phenomena produced by the complexity generators.

9. LONG-RANGE ISING MODEL

9.1 Introduction

9.1.1 Order in low dimensions

Whereas systems with finite-range interactions do not order above zero temperature in one dimension, certain systems with long-range interactions do order (Thouless, 1969; Ruelle, 1969; Griffiths, 1972; Aizenman and Newman, 1986; Aizenman et al., 1988). The archetypical example is the Ising ferromagnetic model with power-law interactions, Jr^{-a}. Also as seen below, for antiferromagnetic interactions, the system incorporates saturated frustration and spin-glass ordering without antiferromagnetic ordering, in the absence of quenched randomness.

The model that we study is defined by the Hamiltonian

$$-\beta\mathscr{H} = \sum_{r_1 \neq r_2} J|r_1 - r_2|^{-a} s_{r_1} s_{r_2} + H \sum_{r_1} s_{r_1}, \tag{9.1}$$

where $\beta = 1/k_B T$ is the inverse temperature, r_1 and r_2 designate the sites on the one-dimensional system, at each site r_i there is an Ising spin $s_{r_i} = \pm 1$, and the sums are over all sites in the system. For ferromagnetic and antiferromagnetic systems, the two-spin interactions J are $J = |J| > 0$ and $J = -|J| < 0$, respectively. For the spin-glass system, for each two spins at any range, their interaction is randomly ferromagnetic (with probability $1 - p$) or antiferromagnetic (with probability p). The second term in Eq. (9.1) is the magnetic-field H term.

9.1.2 Power-law interactions and effective dimensionality

This chapter initiates the investigation of interaction range as a modulator of complexity. Long-range interactions fundamentally alter the physics of statistical mechanical systems by enabling order in low dimensions, tuning between local and mean-field physics, mod-

ifying universality, and transforming frustration effects. Chapters 3–6 established frustration as producing spin-glass chaos in $d = 3$ short-range systems. This chapter extends the investigation to $d = 1$ with long-range interactions.

9.2 Renormalization-Group Method for Long-Range Interactions

9.2.1 Cell-spin construction

For systems with long-range power-law interactions, the standard transfer-matrix approach employed in Chapters 2–8 is not directly applicable: interactions at all separation distances must be tracked, making a single transfer matrix insufficient. Instead, we employ the Niemeyer–van Leeuwen cell-spin method (Niemeyer and van Leeuwen, 1974; van Leeuwen, 1975; Berker and Wortis, 1976), which constructs renormalization-group recursion relations through partition function conservation rather than transfer-matrix manipulation.

The renormalization-group transformation is constructed by first choosing cells on the $d = 1$ system, as shown in Fig. 9.1. Each of our cells has three spins. This cell structure projects both local ferromagnetism and antiferromagnetism, and therefore also spin-glass order.

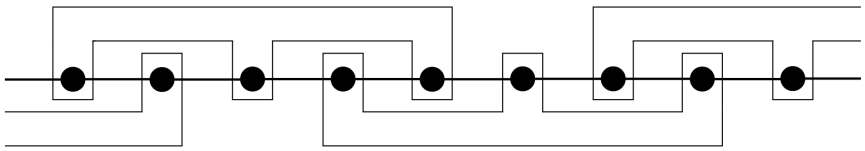


Figure 9.1: Renormalization-group cells for $d = 1$. Each cell contains three spins, and the cell-spin is defined as the sign of the sum of the three spins.

For each cell, a cell-spin is defined as the sign of the sum of the three spins in the cell,

$$s'_{r'} = \text{signum}(s_{r-4} + s_{r-2} + s_r), \tag{9.2}$$

where the signum function returns the sign of its argument, primes denote the renormalized system, and $r' = r/b$, where $b = 3$ is the length-rescaling factor.

9.2.2 Partition function conservation

The renormalized interactions are obtained from the conservation of the partition function Z,

$$\begin{aligned} Z &= \sum_{\{s\}} e^{-\beta\mathscr{H}(\{s\})} = \sum_{\{s'\}}\sum_{\{\sigma\}} e^{-\beta\mathscr{H}(\{s'\},\{\sigma\})} \\ &= \sum_{\{s'\}} e^{-\beta\mathscr{H}'(\{s'\})} = Z', \end{aligned} \tag{9.3}$$

where the summed variable σ represents, for each cell, the four states that give the same cell-spin value. Thus, the renormalized interactions are obtained from

$$e^{-\beta\mathscr{H}'(\{s'\})} = \sum_{\{\sigma\}} e^{-\beta\mathscr{H}(\{s'\},\{\sigma\})}. \tag{9.4}$$

9.2.3 Two-cell cluster approximation

The two-cell cluster approximation of Niemeyer and van Leeuwen consists in carrying out this transformation for two cells, including the six intracell interactions and the nine intercell interactions. A recursion relation is obtained for each renormalized interaction,

$$\begin{aligned} J'_{r'} &= \frac{1}{4}\ln\frac{R_{r'}(+1,+1)R_{r'}(-1,-1)}{R_{r'}(+1,-1)R_{r'}(-1,+1)}, \\ H' &= \frac{1}{4}\ln\frac{R_1(+1,+1)}{R_1(-1,-1)}, \end{aligned} \tag{9.5}$$

where

$$R_{r'}(s'_0,s'_{r'}) = \sum_{\sigma_0,\sigma_{r'}} e^{-\beta H_{0r'}}, \tag{9.6}$$

and the unrenormalized two-cell Hamiltonian contains the six intracell interactions and the nine intercell interactions between the six spins in cells 0 and r'.

9.2.4 Tracking interactions at multiple distances

A crucial feature of this calculation is that we must track the renormalized interactions $J'_1, J'_2, J'_3, \ldots, J'_n$ for multiple separation distances. Unlike short-range models where only nearest-neighbor interactions need to be tracked, the long-range model requires following interactions at all distances that contribute significantly. We have verified convergence by

calculation up to $n = 20$ separation distances.

9.3 Ferromagnetic Results

9.3.1 Phase diagram

The calculated phase diagram of the $d = 1$ long-range ferromagnetic Ising model, with interactions Jr^{-a}, is shown in Fig. 9.2, in terms of temperature $1/J$ and interaction range exponent a. A finite-temperature ferromagnetic phase occurs for $0.74 < a < 2$. The second-order phase transition temperature monotonically decreases between these two limits. At $a = 2$, the phase transition becomes first order, as predicted by rigorous results (Aizenman et al., 1988). For $a > 2$, the phase transition temperature discontinuously drops to zero and there is no ordered phase above zero temperature, also as predicted by rigorous results (Ruelle, 1969; Griffiths, 1972). At the other end, on approaching $a = 0.74$ from above, the phase transition temperature diverges to infinity, meaning that, at all non-infinite temperatures, the system is ferromagnetically ordered.

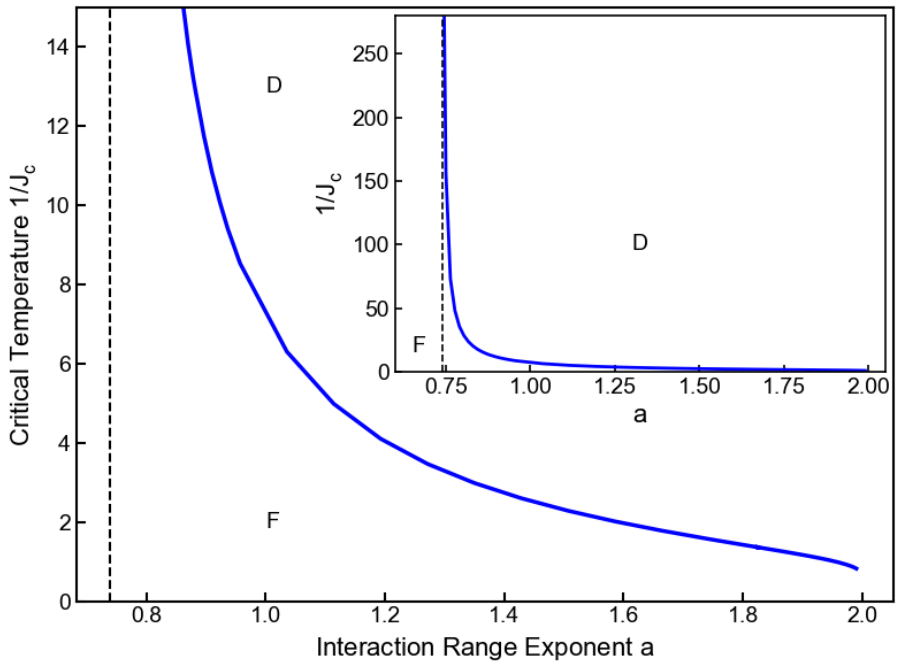


Figure 9.2: Calculated phase diagram of the $d = 1$ long-range ferromagnetic Ising model with interactions Jr^{-a}. Ferromagnetic (F) and disordered (D) phases are seen.

A particularly striking result is that the equivalent-neighbor interactions regime is entered before ($a > 0$) the neighbors become equivalent, namely before the interactions become equal for all separations. At $a = 0.74$, the system is already in the "always ordered"

regime characteristic of infinite-range (mean-field) models, even though the interactions still decay with distance. Note that our calculated value is below the exact value $a = 1$ where the interaction sum diverges. This discrepancy arises from finite-cluster (two-cell) approximation effects: the Niemeyer–van Leeuwen method with finite cell sizes does not capture the exact long-range behavior. The qualitative physics—entry into a regime where the system is always ordered—is correctly reproduced, but the threshold value should be regarded as approximate.

9.3.2 Critical exponents as functions of range

The calculated critical exponents, continuously varying as a function of interaction range a for the finite-temperature ferromagnetic phase transition, are shown in Fig. 9.3. These include the correlation-length critical exponent ν, correlation-function exponent η, specific heat exponent α, magnetization exponents β and δ, and susceptibility exponent γ.

The largest (and only relevant) eigenvalue $\lambda_T = b^{y_T}$ of the derivative matrix of the recursion relations gives $\nu = 1/y_T$ and $\alpha = 2 - d/y_T = 2 - 1/y_T$. The magnetization and susceptibility exponents are obtained from $\partial H'/\partial H = b^{y_H}$ at criticality (Berker and Wortis, 1976). At $a = 2$, $\beta \to 0$ and $\delta \to \infty$, signaling a first-order transition (Fisher and Berker, 1982), in agreement with rigorous results (Aizenman et al., 1988).

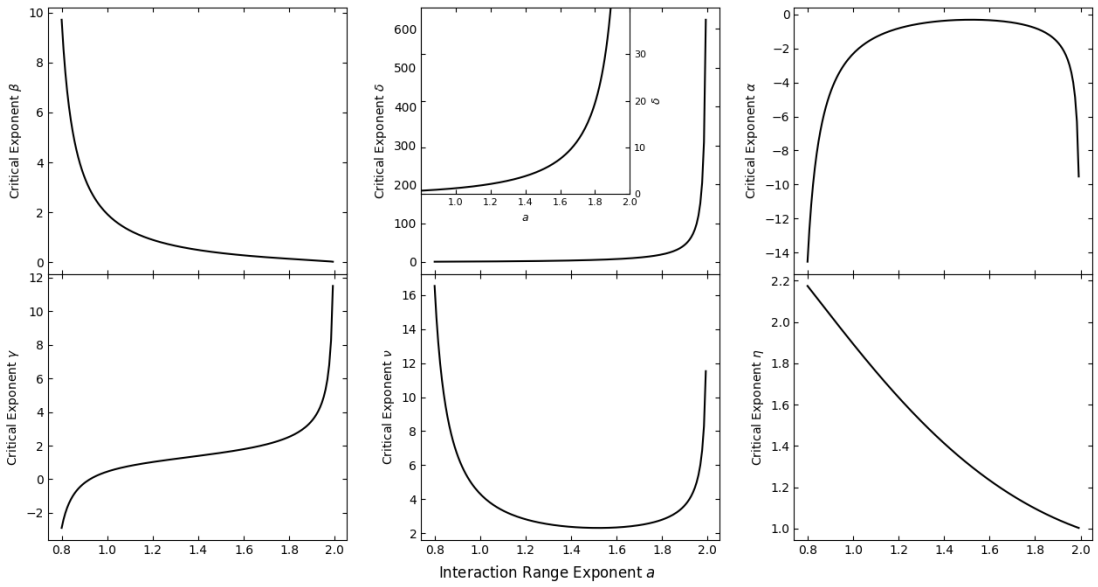


Figure 9.3: Critical exponents ν, η, α, β, γ, and δ as a function of interaction range a for the finite-temperature ferromagnetic phase transition.

9.4 Antiferromagnetic Results: Pervasive Frustration

9.4.1 Absence of antiferromagnetic order

For the antiferromagnetic case, $J < 0$, all triplets of spins at all ranges have competing interactions and this highly frustrated system does not have an ordered phase. Every triplet of spins is frustrated, leading to the complete destruction of antiferromagnetic order even at zero temperature.

9.4.2 Contrast with short-range antiferromagnet

In a short-range ($d = 1$ nearest-neighbor) antiferromagnet, the ground state is the simple alternating pattern $\uparrow\downarrow\uparrow\downarrow\cdots$, which satisfies all bonds. With long-range interactions, frustration becomes pervasive and eliminates even this simple order. Thus, long-range interactions enable ferromagnetic order but destroy antiferromagnetic order in one dimension.

9.5 Spin-Glass Results

9.5.1 Phase diagram without antiferromagnetic order

The spin-glass system, where all couplings for all separations are randomly ferromagnetic or antiferromagnetic (with probability p), does have finite-temperature spin-glass phase transitions, as shown in Fig. 9.4. This phase diagram is highly unusual: it contains ferromagnetic, spin-glass, and disordered phases, but no antiferromagnetic phase.

Typical reentrance behavior (Hinczewski and Berker, 2005) is observed: as temperature is lowered at fixed p, the ferromagnetic phase appears but disappears again at lower temperature in favor of the spin-glass phase.

9.5.2 Piecewise chaotic interaction functions

In the spin-glass phase, the chaos under rescaling signature (McKay et al., 1982a,b; McKay and Berker, 1984; Berker and McKay, 1984) appears in a richer form than in short-range systems. In the long-range case, the interactions at every separation become

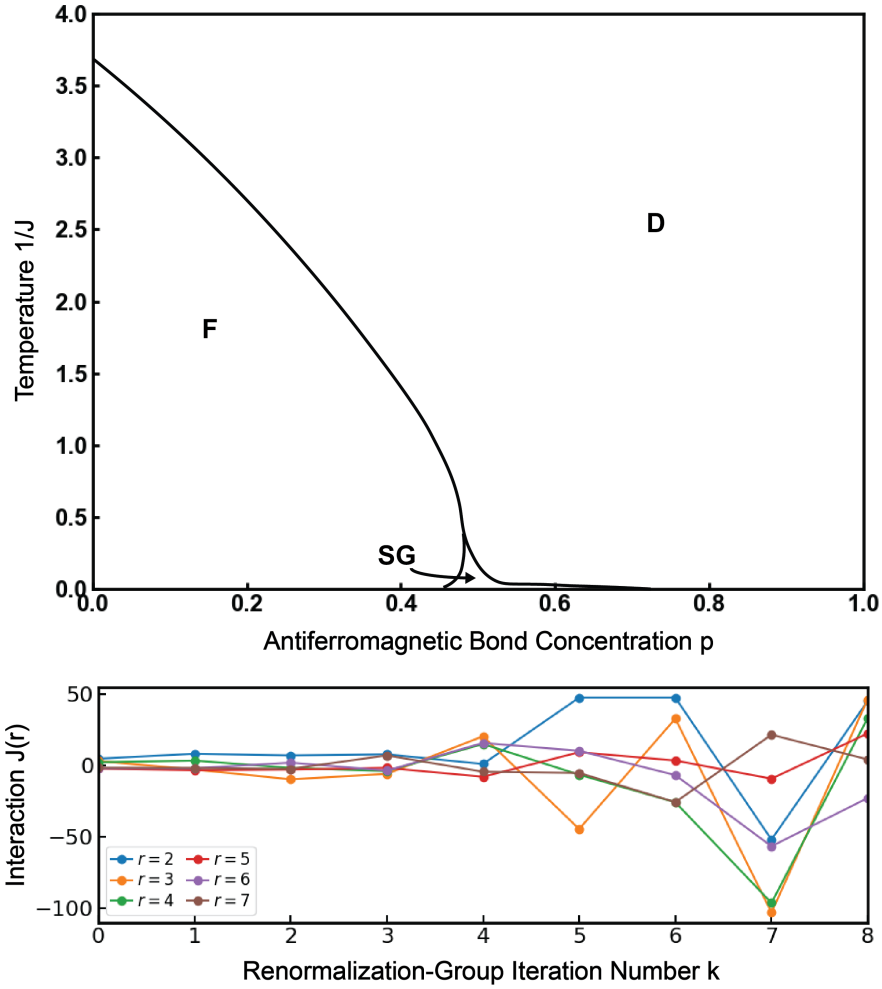


Figure 9.4: Top: Phase diagram of the $d = 1$ long-range Ising spin-glass system. Bottom: Chaos inside the spin-glass phase, showing piecewise chaotic interaction functions.

chaotic, yielding a piecewise chaotic interaction function $J_k(r)$ that varies chaotically with RG iteration k at every distance r.

9.6 Discussion: Interaction Range as Control Parameter

This chapter demonstrates that interaction range acts as a powerful modulator of complexity generated by frustration. Long-range interactions enable order in low dimensions, modify universality, and qualitatively transform frustration effects. Ferromagnetic order is stabilized, antiferromagnetic order is destroyed, and spin-glass order becomes richer, with chaos appearing in a higher-dimensional interaction space.

The range exponent a continuously tunes the system between short-range behavior ($a > 2$), an intermediate regime with finite-temperature order ($0.74 < a < 2$), and an equivalent-neighbor regime ($a < 0.74$). The continuous variation of critical exponents with a demonstrates that interaction range is a relevant RG parameter, altering universality classes.

9.7 Conclusion

We have solved the $d = 1$ Ising ferromagnet, antiferromagnet, and spin glass with long-range power-law interactions Jr^{-a} by a renormalization-group transformation that simultaneously projects ferromagnetic, antiferromagnetic, and spin-glass order.

Long-range interactions enable ferromagnetic order in one dimension, destroy antiferromagnetic order through saturated frustration, and produce a spin-glass phase with piecewise chaotic interactions. This chapter establishes interaction range as a fundamental modulator of complexity. In the next chapter, this long-range RG methodology will be applied to the Blume–Capel model, revealing giant reentrance phenomena.

10. LONG-RANGE BLUME–CAPEL MODEL

10.1 Introduction

10.1.1 The Blume-Capel model and tricritical behavior

Microscopic model systems have played a crucial role in understanding and predicting the complex mathematics of nature, such as the critical singularities at a phase transition (indeed, the occurrence of a phase transition) and the chaos inside a spin-glass phase. Capel (1966), together with Blume (1966), made a seminal contribution to the usefulness of model systems, by including to the local degree of freedom the magnitude as well as the alignment, leading to a multitude of successful theories for qualitatively new phenomena.

The Blume–Capel model introduces a "vacancy" or "zero" spin state in addition to the usual ± 1 Ising states. The competition between magnetic ordering (favored by low temperature) and vacancy proliferation (controlled by a chemical potential Δ) produces tricritical behavior: a line of second-order transitions meeting a line of first-order transitions at a tricritical point.

In this chapter, we study a Blume–Capel model with long-range power-law interactions, defined by the Hamiltonian

$$-\beta\mathscr{H} = \sum_{r_1 \neq r_2} \left[J s_{r_1} s_{r_2} - \Delta \left(s_{r_1}^2 + s_{r_2}^2 \right) \right] |r_1 - r_2|^{-a}, \tag{10.1}$$

where $\beta = 1/k_B T$ is the inverse temperature, r_1 and r_2 designate the sites on the one-dimensional system, at each site r_i there is a spin $s_{r_i} = \pm 1, 0$, and the sums are over all sites in the system. The interaction is ferromagnetic, $J > 0$. In the second term, Δ is the chemical potential of the non-zero spins.

10.1.2 Motivation for long-range extension

This chapter completes the systematic investigation of interaction range as a complexity modulator begun in Chapter 9. While Chapter 9 examined how long-range interactions affect the Ising model (with and without quenched disorder), this chapter investigates how long-range interactions interact with a more complex microscopic model—one that already exhibits tricritical behavior in its short-range version.

The key result is *giant reentrance*: as temperature is lowered, the system passes through the sequence disorder $\rightarrow$ order $\rightarrow$ disorder. This dramatic non-monotonic behavior arises from the interplay between (i) long-range interactions that enable finite-temperature order in $d = 1$, (ii) vacancy chemical potential that controls the density of magnetic ($s = \pm 1$) versus non-magnetic ($s = 0$) sites, and (iii) temperature that affects both magnetic ordering and vacancy proliferation.

The Blume–Capel model (Capel, 1966; Blume, 1966) was introduced to describe magnetic systems where the local moment can be "quenched" (reduced to zero) by crystal field effects or other mechanisms. The model has found applications in: He^3–He^4 mixtures, where the vacancy state represents He^3 atoms in a He^4 superfluid (Blume et al., 1971); microemulsions (Schick and Shih, 1986); metamagnets (Yüksel et al., 2022). The tricritical point—where first- and second-order transitions meet—is the defining feature of the Blume–Capel phase diagram. Our investigation reveals how long-range interactions modify this tricritical structure.

10.2 Renormalization-Group Method

10.2.1 Cell-spin assignment with vacancies

This chapter builds directly on Chapter 9, using the same renormalization-group methodology for long-range interactions, and using the 3-spin cells shown in Fig. 9.1. The three site-spins inside each cell determine a cell-spin $s'_{r'_i} = \pm 1, 0$, where primes designate quantities of the renormalized system.

The majority value of the site-spins is the value of the cell-spin (see Table 10.1). When no majority exists, meaning that the site-spins have the values $(+1, -1, 0)$ in any order, the cell-spin has the value 0. This reflects the fact that local disorder represents an effective

Table 10.1: Cell-spin assignment rules. The majority value of the site spins defines the cell spin. The configuration $(+1,-1,0)$ has no majority and maps to 0.

Site-spin configuration	Cell-spin value
$(+1,+1,+1)$	$+1$
$(+1,+1,0)$, $(+1,+1,-1)$	$+1$
$(-1,-1,-1)$	-1
$(-1,-1,0)$, $(-1,-1,+1)$	-1
$(0,0,0)$, $(0,0,\pm1)$	0
$(+1,-1,0)$	0

vacancy and in fact has been used to determine the crossover from second-order to first-order phase transitions in Potts models (Nienhuis et al., 1979; Devre and Berker, 2022) and the multicritical phase diagrams of the Ashkin–Teller models (Keçoğlu and Berker, 2023; Zeynioğlu and Berker, 2025).

10.2.2 Recursion relations

The renormalized interactions are obtained from a partial summation of the partition function Z,

$$Z = \sum_{\{s\}} e^{-\beta\mathscr{H}(\{s\})} = \sum_{\{s'\}} \sum_{\{\sigma\}} e^{-\beta\mathscr{H}(\{s'\},\{\sigma\})} = \sum_{\{s'\}} e^{-\beta\mathscr{H}'(\{s'\})} = Z', \tag{10.2}$$

where the summed variable σ represents, for each cell, the seven (in the case of $s'_{r'_i} = \pm1$) or thirteen (in the case of $s'_{r'_i} = 0$) site-spin states that give the same cell-spin value. Thus,

$$e^{-\beta\mathscr{H}'(\{s'\})} = \sum_{\{\sigma\}} e^{-\beta\mathscr{H}(\{s'\},\{\sigma\})} \tag{10.3}$$

yields the renormalized interactions.

Under the renormalization-group transformations, the long-ranged Hamiltonian takes the most general form (Berker and Wortis, 1976; Blume et al., 1971)

$$-\beta\mathscr{H} = \sum_{r_1\neq r_2} \left[J_{r_1r_2} s_{r_1} s_{r_2} + K_{r_1r_2} s_{r_1}^2 s_{r_2}^2 - \Delta_{r_1r_2}(s_{r_1}^2 + s_{r_2}^2) \right]. \tag{10.4}$$

Equation (10.1) gives the initial conditions of the renormalization-group flows, written in the variables of Eq. (10.4). The biquadratic term $K_{r_1r_2} s_{r_1}^2 s_{r_2}^2$ is generated under RG even when absent initially—a standard feature of Blume–Capel RG flows (Berker and Wortis, 1976).

Niemeyer and van Leeuwen's two-cell cluster approximation (Niemeyer and van Leeuwen, 1974; van Leeuwen, 1975; Berker and Wortis, 1976) is used. The two-cell cluster approximation consists in carrying out the transformation of Eq. (10.3) for two cells, including the 6 intracell interactions and the 9 intercell interactions.

A recursion relation is obtained for each renormalized interaction (for each separation, in the long-range setting),

$$\begin{aligned} J' &= \frac{1}{2}\ln\frac{R(+1,+1)}{R(+1,-1)}, \\ \Delta' &= \ln\frac{R(+1,0)}{R(0,0)}, \\ K' &= \frac{1}{2}\ln\frac{R(+1,+1)R(+1,-1)R(0,0)^2}{R(0,+1)^4}, \end{aligned} \tag{10.5}$$

where

$$R(s'_{r'_1}, s'_{r'_2}) = \sum_{\sigma_{r'_1},\sigma_{r'_2}} e^{-\beta H_{r'_1 r'_2}}, \tag{10.6}$$

and the unrenormalized two-cell Hamiltonian includes the six intracell and nine intercell interactions between the six spins in cells at r'_1 and r'_2.

10.2.3 Computational implementation

Our (approximate) renormalization-group calculation proceeds as follows: We start with a linear system of $3^{10} = 59{,}049$ spins, all interacting with the starting long-range power-law interaction of Eq. (10.1). After one transformation, we have 19,683 spins interacting with the renormalized long-range interaction of Eq. (10.4). After one more transformation, we have 6,561 spins, and we viably carry out six transformations.

For spot checks, we start with $3^{20} = 3{,}486{,}784{,}401$ spins and can carry out sixteen transformations. It is thus seen that our calculation becomes less viable for longer-range interactions, namely smaller a.

10.3 Results: Phase Diagrams

10.3.1 Range dependence of phase structure

Seven different calculated phase diagrams of the $d = 1$ Blume–Capel model with long-range power-law interactions are overlaid in Fig. 10.1. Ferromagnetic (F) and disordered (D) phases are seen. First- and second-order phase boundaries are respectively shown with dashed and full lines. The dashed and full lines meet at a tricritical point.

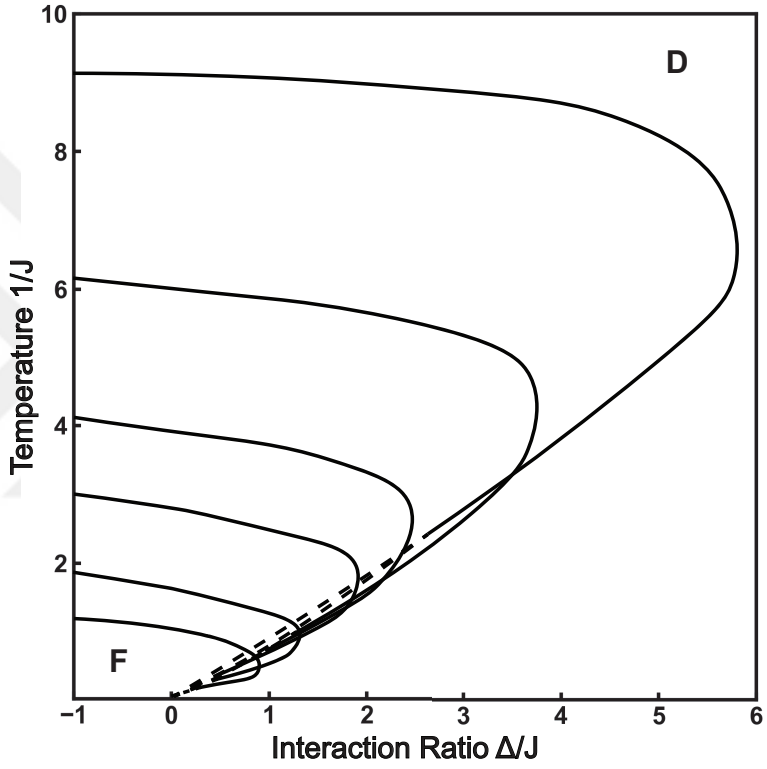


Figure 10.1: Calculated phase diagrams of the $d = 1$ Blume–Capel model with long-range power-law interactions. Ferromagnetic (F) and disordered (D) phases are seen. First- and second-order phase boundaries are shown with dashed and full lines, meeting at a tricritical point. The phase diagrams shown are, from high temperatures downwards, for $a = 0.5, 0.85, 0.9, 1.0, 1.1, 1.3, 1.5$. After the $a = 0.85$ diagram, each consecutive diagram is shifted by 0.5 in Δ/J for visibility. For $a > 0.74$, a giant reentrance (D→F→D) occurs as temperature is lowered. The system for $a = 0.5$ lies in the near-equivalent-neighbor regime.

Starting at a point in each phase, the renormalization-group trajectory flows to a completely stable fixed point (a sink) (Berker and Wortis, 1976). Thus, the basin of attraction of a sink constitutes the corresponding thermodynamic phase.

The sinks are best characterized by the exponentiated Hamiltonian between two interacting sites,

$$T_{ij} \equiv e^{-\beta H_{r_i r_j}} = e^{J_{ij} s_i s_j + K_{ij} s_i^2 s_j^2 + \Delta_{ij}(s_i^2 + s_j^2)}. \tag{10.7}$$

The sink transfer matrices (each divided by its largest element), written with $(1,-1,0)$ basis in row/column order, are:

Ferromagnetic phase sink:

$$T_F = \begin{pmatrix} 1 & 0 & 0 \\ 0 & 1 & 0 \\ 0 & 0 & 0 \end{pmatrix} \tag{10.8}$$

Dense disordered phase sink:

$$T_{D,\text{dense}} = \begin{pmatrix} 1 & 1 & 0 \\ 1 & 1 & 0 \\ 0 & 0 & 0 \end{pmatrix} \tag{10.9}$$

Dilute disordered phase sink:

$$T_{D,\text{dilute}} = \begin{pmatrix} 0 & 0 & 0 \\ 0 & 0 & 0 \\ 0 & 0 & 1 \end{pmatrix} \tag{10.10}$$

These matrices occur, at the sinks, for any two spins at any separation.

Starting at a point on each phase boundary, the renormalization-group trajectory flows to a singly unstable fixed point, unstable toward the two phases separated by this boundary. Thus:

F—Dense D boundary (second order):

$$T_{\text{F-D,dense}} = \begin{pmatrix} 1 & 9 & 0 \\ 9 & 1 & 0 \\ 0 & 0 & 0 \end{pmatrix} \tag{10.11}$$

F—Dilute D boundary (first order):

$$T_{\text{F-D,dilute}} = \begin{pmatrix} 0 & 0 & 1 \\ 0 & 1 & 1 \\ 1 & 1 & 1 \end{pmatrix} \tag{10.12}$$

Dense D—Dilute D boundary (no phase transition):

$$T_{\text{D-D}} = \begin{pmatrix} 1 & 1 & 1 \\ 1 & 1 & 1 \\ 1 & 1 & 1 \end{pmatrix} \tag{10.13}$$

Thus, the entire global phase diagram is extracted from the renormalization-group flows.

The calculated phase diagrams in Fig. 10.1 are, from high temperatures downwards, for $a = 0.5, 0.85, 0.9, 1.0, 1.1, 1.3, 1.5$. After the $a = 0.85$ phase diagram, each consecutive phase diagram is drawn shifted by 0.5 in Δ/J, for better visibility. Thus, in fact the first-order boundaries of all phase diagrams meet at $\Delta/J = 0$ at zero temperature $1/J = 0$.

10.3.2 Giant reentrance phenomenon

As exemplified in Fig. 10.1, for $a > 0.74$, the phase diagrams show a giant (numerically speaking) reentrance behavior, with the sequence disordered $\rightarrow$ ferromagnetic $\rightarrow$ disordered as temperature is lowered.

10.3.3 Physical mechanism

The giant reentrance can be understood as follows:

1. High temperature: The system is disordered because thermal fluctuations overcome magnetic interactions.

2. Intermediate temperature: Magnetic ordering becomes favorable. The ferromagnetic coupling J dominates over thermal disorder, and the system orders ferromagnetically.

3. Low temperature: The vacancy chemical potential Δ becomes dominant. If Δ favors vacancies (non-zero spins are penalized), the system fills with vacancies ($s = 0$), which cannot order magnetically. The system becomes disordered again, not by thermal fluctuations but by vacancy dilution.

The long-range interactions are essential for this phenomenon in $d = 1$: without them, there would be no finite-temperature ferromagnetic phase to enter and then leave.

The system for $a = 0.5$ is in the near-equivalent-neighbor regime. In the absence of zeroes, this system is magnetized for all non-infinite temperatures. However, with the introduction of zeroes via the chemical potential, a tricritical phase diagram occurs, with a reverse phase transition, from high-temperature ordered to low-temperature disordered phase, as seen in Fig. 10.1. This represents an extreme version of the reentrance: in the equivalent-neighbor limit, the system is always ordered (at any finite temperature) in the pure Ising case, but the introduction of vacancies can destroy this order at low temperature.

10.4 Results: Critical and Tricritical Temperatures

The critical temperatures in the no-zeroes limit, $\Delta/J \to -\infty$, and the tricritical temperatures, as a function of the interaction-range exponent a, are given in Fig. 10.2. There are several important features:

- Finite-temperature ferromagnetic phase transition occurs for $0.74 < a < 2$, matching the range found in Chapter 9 for the pure Ising model.

- The second-order phase transition temperature monotonically decreases between these two limits.

- At $a = 2$, the phase transition temperature discontinuously drops to zero, and for $a > 2$ there is no ordered phase above zero temperature, in agreement with rigorous results (Ruelle, 1969; Griffiths, 1972; Aizenman et al., 1988).

- On approaching $a = 0.74$ from above, the phase transition temperature and the tricritical temperature both diverge to infinity, implying ferromagnetic order at all non-infinite temperatures.

- The first-order transition takes over the entire phase boundary as this limit of $a \to 0.74^{+}$ is approached.

Thus, the equivalent-neighbor-interactions regime is entered before ($a > 0$) the neighbors become equivalent, namely before the interactions become equal for all separations. To the left of the dashed line in Fig. 10.2 is the equivalent-neighbor regime, occurring here as an approximate result at $a = 0.74$, whereas the exact onset is at $a = 1$, consistent with the two-cell cluster approximation scheme also implemented in Chapter 9.

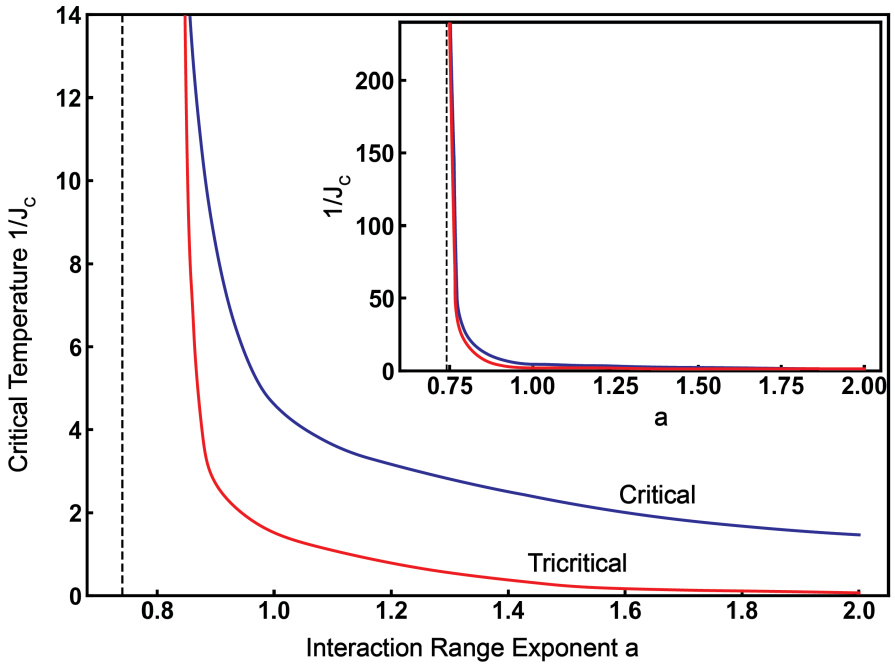


Figure 10.2: Critical temperatures in the no-zeroes limit $\Delta/J \to -\infty$ (upper curve) and tricritical temperatures (lower curve) as a function of interaction-range exponent a. A finite-temperature ferromagnetic transition occurs for $0.74 < a < 2$. At $a = 2$ the transition temperature drops to zero and for $a > 2$ there is no ordered phase above zero temperature, consistent with rigorous results. As $a \to 0.74^{+}$, both curves diverge and the first-order portion takes over the entire phase boundary.

The evolution of the tricritical point with range exponent a reveals how long-range interactions modify phase diagram topology. As a decreases (longer-range interactions), both critical and tricritical temperatures increase, and the first-order portion of the phase boundary grows relative to the second-order portion. In the equivalent-neighbor limit, the entire phase boundary becomes first order.

10.5 Discussion: Competition Between Ordering and Dilution

This chapter demonstrates how interaction range affects a system that already exhibits multicritical behavior in its short-range version. The long-range interactions do not merely enable order in $d = 1$—they qualitatively transform the phase diagram topology, producing giant reentrance and shifting the balance between first- and second-order transitions. The Blume–Capel model exhibits richer behavior than the pure Ising model because the vacancy state provides an additional degree of freedom that competes with magnetic ordering.

The giant reentrance differs from the reentrance phenomena in previous chapters:

- Chapter 2 (interface density reentrance): domain growth $\rightarrow$ merger $\rightarrow$ interface elimination; subtle changes in local densities.
- Chapter 9 (F–SG reentrance): competition between ferromagnetic order and spin-glass frustration; moderate reentrance.
- Chapter 10 (D–F–D reentrance): vacancy dilution at low temperature; global return to disorder; giant magnitude.

The giant reentrance is most dramatic because it involves complete destruction of an ordered phase by a competing mechanism (vacancy proliferation) that becomes dominant at low temperature.

As $a \rightarrow 0.74$, the system approaches the equivalent-neighbor (mean-field) limit. In this limit, the critical and tricritical temperatures diverge, the first-order portion of the phase boundary grows, and eventually the entire phase boundary becomes first order. The long-range RG calculation reproduces this mean-field-like behavior as a decreases.

The giant reentrance phenomenon could be observable in systems with long-range interactions and variable local moment:

- Dipolar Ising magnets in quasi-1D geometries,
- Cold-atom platforms with power-law interactions (e.g., Rydberg atoms, polar molecules) (Defenu et al., 2023),

- Spin chains coupled to environments (e.g., phonons) that can quench local moments (Chen et al., 2019).

10.6 Conclusion

We have solved the $d = 1$ Blume–Capel model with long-range power-law interactions. A series of finite-temperature tricritical phase diagrams is found as a function of the power-law exponent. Giant reentrance—disorder to order to disorder as temperature decreases—occurs due to competition between long-range magnetic interactions and vacancy proliferation.

Chapters 9 and 10 together complete the demonstration of interaction range as a complexity modulator. Chapter 9 showed that long-range interactions enable ferromagnetic order in $d = 1$, destroy antiferromagnetic order through pervasive frustration, and create spin-glass phases with piecewise chaotic interaction functions. The current chapter showed that long-range interactions produce giant reentrance in the Blume–Capel model, shift the balance between first- and second-order transitions, and drive the system toward mean-field behavior as the range increases. Together, these chapters establish interaction range as a relevant parameter that changes universality classes, enables or destroys order depending on context, produces qualitatively new phenomena (giant reentrance, piecewise chaos) not present in short-range systems, and provides a continuous interpolation between local and mean-field physics.

11. METASTABLE POTTS DROPLETS

11.1 Introduction: Nonequilibrium Properties from an Equilibrium Calculation

11.1.1 Metastability in physical systems

The preceding chapters of this thesis have developed and applied position-space renormalization-group methods to uncover increasingly complex equilibrium phase structures: multicritical topologies, spin-glass ordering, nematic phases, and algebraically ordered states. A natural question is whether the same framework can reach beyond equilibrium thermodynamics. In this chapter, we show that it can. By adapting the finite-system renormalization-group density calculation through a simple change of boundary conditions, metastable droplet properties and hysteresis loops are obtained from what remains fundamentally an equilibrium calculation. This extends the methodological scope of the renormalization-group approach developed throughout this thesis to nonequilibrium phenomena.

Recently equilibrium renormalization-group calculations have been simply extended to the calculation of the properties of metastable droplets of the nonequilibrium phase surviving inside the equilibrium thermodynamic phase (Eren and Berker, 2020). This method was illustrated with the Ising model in $d = 3$ spatial dimensions. The limiting droplet sizes have been determined as a function of temperature and magnetic field. The critical magnetic fields, above which no metastable droplet can exist, have been calculated as a function of temperature. The method consists in making a finite-system renormalization-group calculation of the magnetization (Berker and Ostlund, 1979) and matching the boundary conditions of the outermost layer of the droplet. If this reverse magnetization sustains inside the droplet, the droplet exists, and otherwise not, for the given droplet size.

In this chapter, we extend this work to q-state Potts models for arbitrary q in $d = 3$. We determine the threshold droplet sizes as a function of the number of states q and find changes even at high values of q, similarly to the equilibrium thermodynamic properties

of the Potts models (Artun and Berker, 2020). The method also naturally yields the calculation of hysteresis loops, which yields a large variety as a function of q, domain size, and temperature.

11.1.2 Finite-system renormalization group with fixed boundaries

This chapter represents a methodological extension of the renormalization-group techniques developed throughout this thesis, demonstrating that the same framework used for equilibrium phase structure can be adapted to address non-equilibrium phenomena. While Chapters 2–10 focused on equilibrium thermodynamics—phases, phase transitions, critical exponents, and the topology of RG flows—this chapter shows that finite-system RG calculations with fixed boundary conditions can determine:

1. Metastable droplet existence limits: the critical size L_C below which a droplet of the metastable phase can persist,

2. Hysteresis loops: path-dependent magnetization curves observed when scanning across first-order transitions,

3. Dependence on microscopic parameters: how L_C and hysteresis shapes vary with q, T, and H.

This extension is significant because metastability is ubiquitous in real systems, hysteresis is a defining nonequilibrium signature of first-order transitions, and demonstrating nonequilibrium reach increases the utility of RG methods.

The Potts models studied here were introduced in Chapter 2, where we calculated complete thermodynamic densities and discovered interface density reentrance. The present chapter uses the same transfer-matrix formalism and density recursion relations, but applies them to finite systems with fixed boundary conditions rather than infinite systems approaching thermodynamic sinks.

Metastable states are crucial in many physical contexts: supercooled water (Poole et al., 1992; Gallo and Stanley, 2017), supersaturated solutions (Debenedetti, 1996; Kashchiev, 2000), surface adsorption (Butler et al., 1979; Migone et al., 1983), magnetic domains (Seul and Andelman, 1995; Sethna et al., 2001), and glasses (Debenedetti, 1996). Our method provides a systematic way to determine when such metastable configurations can

exist as a function of system parameters.

11.2 Model and Method

11.2.1 The q-state Potts model in magnetic field

The Potts models are defined by the Hamiltonian

$$-\beta\mathscr{H} = \sum_{\langle ij\rangle}\left\{J\left[\delta(s_i,s_j)-\frac{1}{q}\right]+H\left[\delta(s_i,1)+\delta(s_j,1)\right]\right\}, \tag{11.1}$$

where $\beta = 1/k_BT$, at site i the spin $s_i = 1,2,\ldots,q$ can be in q different states, the delta function $\delta(s_i,s_j) = 1$ (0) for $s_i = s_j$ ($s_i \neq s_j$), and $\langle ij\rangle$ denotes summation over all nearest-neighbor pairs of sites. We have used the traceless form of interaction in the first term of Eq. (11.1).

The magnetic field H in Eq. (11.1) is defined so as to favor one of the Potts states (state 1). For $H > 0$, the equilibrium phase has positive magnetization

$$M = \frac{\langle\delta(s_i,1)\rangle - \frac{1}{q}}{1-\frac{1}{q}} > 0, \tag{11.2}$$

while the metastable phase has $M < 0$ (predominantly in states $2,3,\ldots,q$).

11.2.2 Renormalization-group formulation

Under renormalization-group transformation, the Hamiltonian is conveniently expressed as

$$-\beta\mathscr{H} = \sum_{\langle ij\rangle}\left[E(s_i,s_j)+G\right]. \tag{11.3}$$

The last term is an additive constant unavoidably generated by the RG transformation and essential for the calculation of thermodynamic densities. With no loss of generality, after each RG step, G is fixed so that the largest interaction energy satisfies $E_{\max} = 0$ (and all other $E < 0$). This formulation allows global RG trajectories (needed for densities at the trajectory onset) without numerical overflow.

11.2.3 Transfer-matrix implementation

As the RG transformation, we use the Migdal–Kadanoff approximation (Migdal, 1975; Kadanoff, 1976) with length-rescaling factor $b = 2$, which is also the exact transformation for a $d = 3$ hierarchical lattice (Berker and Ostlund, 1979; Griffiths and Kaufman, 1982; Kaufman and Griffiths, 1984). This transformation consists of bond moving followed by decimation and is simply expressed using the transfer matrix $T(s_i, s_j) = e^{E(s_i,s_j)}$.

Bond moving consists of taking the power of each element:

$$\tilde{T}(s_i, s_j) = \left[T(s_i, s_j)\right]^{b^{d-1}}. \tag{11.4}$$

Decimation consists of matrix multiplication:

$$\mathbf{T}' = \tilde{\mathbf{T}} \cdot \tilde{\mathbf{T}} e^{\tilde{G}}, \tag{11.5}$$

where $\tilde{G}$ is chosen so that the largest renormalized energy is zero, $E'_{\max} = 0$. The recursion for the additive constant is $G' = b^d G + \tilde{G}$.

11.2.4 Density recursion with fixed boundary conditions

The densities are calculated by the density recursion relation

$$\mathbf{M} = b^{-d} \mathbf{M}' \cdot \mathbf{R}, \tag{11.6}$$

where $\mathbf{M} = [1, \langle \delta(s_i, m) \delta(s_j, n) \rangle]$ are the densities conjugate to the energies $\mathbf{K} = [G, E(m,n)]$. Here m, n span the Potts states $(1, \ldots, q)$ and $n = m$ is not included in $\mathbf{K}$, since these correspond to leading energies and are set to zero by the choice of $\tilde{G}$ (fixing $E'_{\max} = 0$). The recursion matrix is $\mathbf{R} = \partial \mathbf{K}' / \partial \mathbf{K}$.

11.2.5 Criterion for droplet existence

The key difference from the equilibrium calculation is that we use multiply self-imbedded density recursion,

$$\mathbf{M}^{(0)} = b^{-nd} \mathbf{M}^{(n)} \cdot \mathbf{R}^{(n)} \cdots \mathbf{R}^{(1)}, \tag{11.7}$$

where $\mathbf{M}^{(m)}$ are the densities at energies $\mathbf{K}^{(m)}$ reached after the mth RG iteration. The densities $\mathbf{M}^{(0)}$ are computed by imposing a *droplet boundary condition* on $\mathbf{M}^{(n)}$, where the droplet linear size is $L = b^n$.

We perform metastable droplet calculations for $H > 0$ in Eq. (11.1), so that the magnetization (11.2) is positive (negative) in the equilibrium (metastable) phase. The metastable droplet boundary condition is

$$\langle \delta(s_i, m \neq 1)\delta(s_j, m)\rangle = 1, \tag{11.8}$$

i.e., the outermost layer is pinned in one of the unfavored Potts states.

The calculation proceeds as follows:

1. Start with a droplet of size $L = b^n$ with boundary spins fixed in the metastable phase (state $m \neq 1$).

2. Apply n RG iterations, tracking how the interior magnetization evolves.

3. If $M < 0$ at the end, the metastable droplet sustains; if $M > 0$, it does not.

4. The critical size L_C is the largest L for which $M < 0$.

This procedure determines whether a droplet of given size can maintain its metastable character against the external field favoring the equilibrium phase.

11.3 Results: Metastable Droplets

11.3.1 Magnetization versus droplet size

The calculated metastable droplet magnetizations M as a function of droplet size L are given in Fig. 11.1, for temperature $T/T_C = J_C/J = 0.25$, where $1/J_C$ is the equilibrium critical temperature obtained (Berker and Ostlund, 1979; Artun and Berker, 2020) for each q from the solution of

$$x = \frac{x^8 + q - 1}{2x^4 + q - 2}, \qquad x = e^{J_C}. \tag{11.9}$$

The droplet exists when its magnetization is negative. In each panel for each q, the lines are for magnetic fields $H = 0.1, 0.5, 1, 2, 3, 4.5$ from right to left. The magnetization discontinuity occurs at the maximal droplet size L_C for each (q, H). Increasing H favors the equilibrium state and suppresses the metastable droplet.

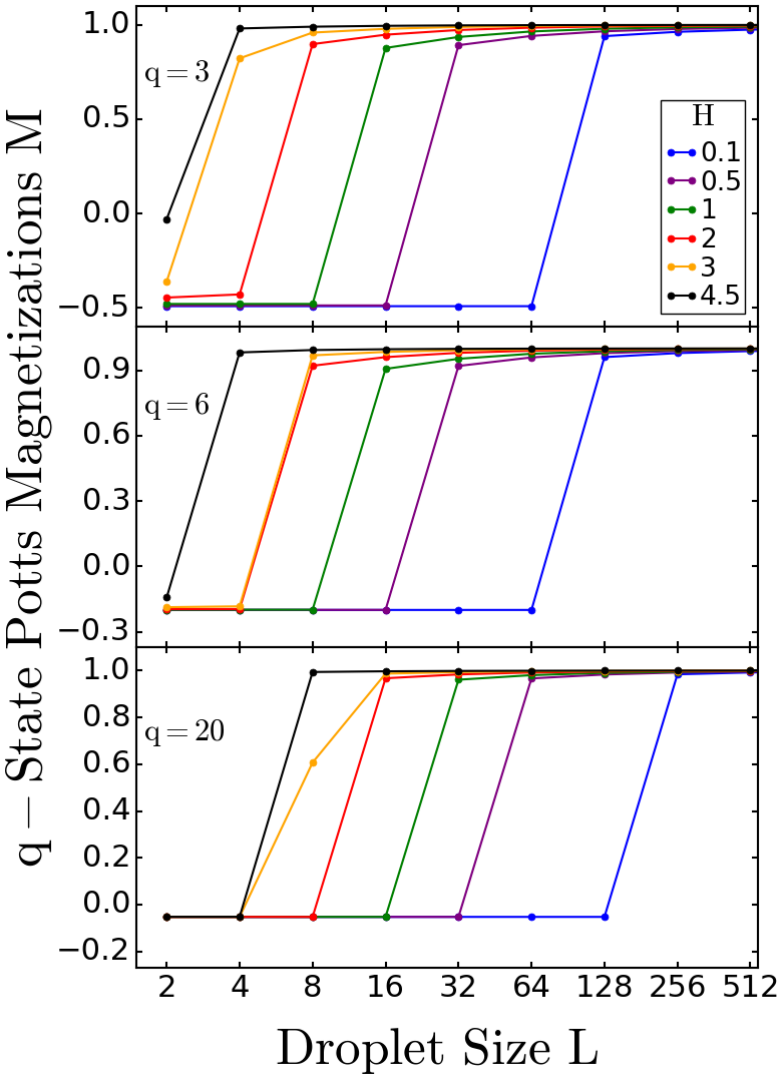


Figure 11.1: Metastable droplet magnetizations $M = [\langle \delta(s_i, 1) \rangle - 1/q]/(1 - 1/q)$ as a function of droplet size, at temperature $T/T_C = J_C/J = 0.25$. The droplet exists when the magnetization is negative. In each panel for each number q of Potts states, the lines are for magnetic fields $H = 0.1, 0.5, 1, 2, 3, 4.5$ from right to left. The maximal droplet size is the average of the lengths at each end of the rise from negative to positive calculated magnetization.

11.3.2 Critical droplet size versus number of states

The calculated maximal droplet sizes as a function of the number q of Potts states, for different magnetic fields at $T/T_C = 0.25$, are given in Fig. 11.2. A wide range of droplet sizes is obtained under different conditions.

The multistepped curves show changes even at unusually high values of q (hundreds), mirroring equilibrium Potts behavior where the transition temperature does not saturate with q, unlike in similar clock models (Artun and Berker, 2020). This non-saturation connects to the full permutational symmetry of the Potts model: every state is equidistant from every other state, so increasing q continues to modify entropy and interfacial competition even at large q.

11.3.3 Power-law scaling

Maximal droplet sizes as a function of magnetic field at $T/T_C = 0.25$ are given in Fig. 11.3. As in Fig. 11.2, the maximal droplet size occurs at large q. A crossover in power-law behavior is seen:

$$\begin{aligned} L_C &\sim H^{-0.99} \quad \text{(low } H\text{)}, \\ L_C &\sim H^{-0.33} \quad \text{(very low } H\text{)}. \end{aligned} \tag{11.10}$$

The existence of a maximal droplet size L_C follows from competing contributions:

1. Surface energy scaling as L^{d-1},

2. Bulk field energy scaling as HL^d,

3. Balance yielding the estimate
$$L_C \sim \sigma/H, \tag{11.11}$$
consistent with the observed near-H^{-1} regime.

The deviation at very low H indicates crossover to a regime where proximity to the coexistence line ($H = 0$) and critical fluctuations modify the naive balance.

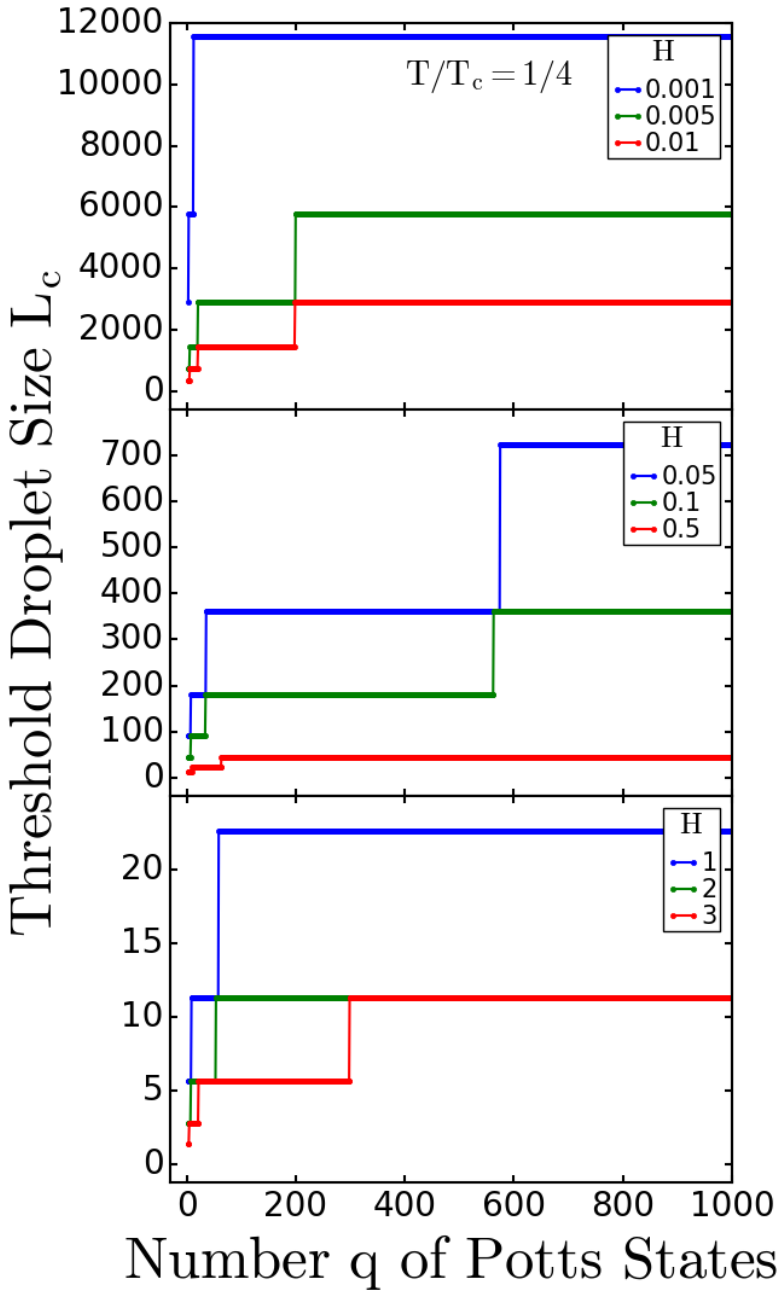


Figure 11.2: Maximal droplet sizes as a function of the number q of Potts states, for different magnetic fields, at temperature $T/T_C = J_C/J = 0.25$. The multistepped curves are, from top to bottom in each panel, for $H = 0.001, 0.005, 0.01$ (top panel), $0.05, 0.1, 0.5$ (middle panel), $1, 2, 3$ (bottom panel). Note from vertical axis values the wide range of droplet sizes under different conditions. A trend is seen in the droplet size values, but not in the step occurrences.

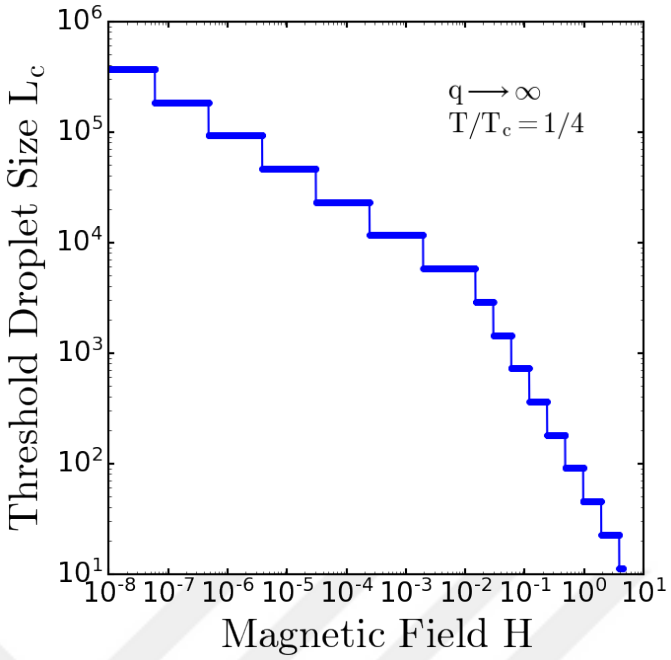


Figure 11.3: Maximal droplet sizes as a function of magnetic field, at temperature $T/T_C = J_C/J = 0.25$. As seen in Fig. 11.2, the maximal droplet size occurs at large q. A crossover in power-law behavior is clearly seen, from $L_C \sim H^{-0.99}$ at low H to $L_C \sim H^{-0.33}$ at very low H.

11.4 Results: Hysteresis Loops

11.4.1 Method

Hysteresis loops occur when scanning across a first-order phase transition: the system retains memory through pinned spins at microdomain boundaries, impurities, or slow dynamics. Our method naturally applies.

In performing the finite-domain density calculation, we keep the boundary condition pinned at the $q = 1$ phase when scanning *down* in magnetic field and at a $q \neq 1$ phase when scanning *up* in magnetic field. Thus, in all results, the upper (lower) branch of the hysteresis loop is obtained for scanning down (up) in H.

11.4.2 Temperature dependence

Hysteresis loops for different temperatures, for $q = 3$, are shown in Fig. 11.4. From outer to inner, the loops correspond to $T/T_C = 0.25, 0.50, 0.75$. As $T \to T_C$, the loops narrow,

reflecting weakening of the first-order character. The two branches acquire curvature starting from the nonleading side relative to the scan direction, reflecting boundary-condition asymmetry.

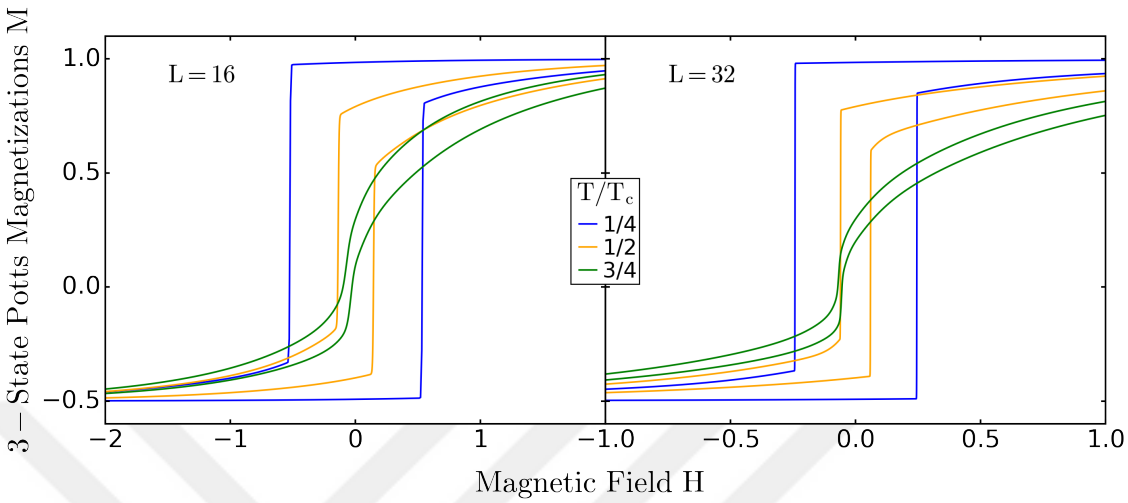


Figure 11.4: Hysteresis loops for different temperatures, for $q = 3$, and for two different sizes $L = 16$ on the left, $L = 32$ on the right. For both panels, from outer to inner, the loops are for $T/T_C = J_C/J = 0.25, 0.50, 0.75$. As the temperature approaches T_C, the hysteresis loops get narrower and the two branches composing the loop acquire curvature starting from the nonleading side with respect to scanning direction.

11.4.3 Size dependence

Hysteresis loops for different sizes, for $q = 3$ and $T/T_C = 0.50$, are given in Fig. 11.5. As L increases, loops narrow and develop vertical edges; at infinite size, the equilibrium discontinuity is recovered and the hysteresis collapses to the coexistence field. This demonstrates hysteresis as a finite-size effect: finite domains retain memory because reversal requires overcoming a barrier.

11.4.4 Dependence on number of states

Hysteresis loops for different q, at $T/T_C = 0.25$ and $L = 32$, are shown in Fig. 11.6. From outer to inner, the loops correspond to $q = 20, 10, 6, 5, 4, 3$. As q decreases, loops narrow, consistent with decreasing latent heat (weaker first-order transition) at smaller q. Curvature again appears on the nonleading side.

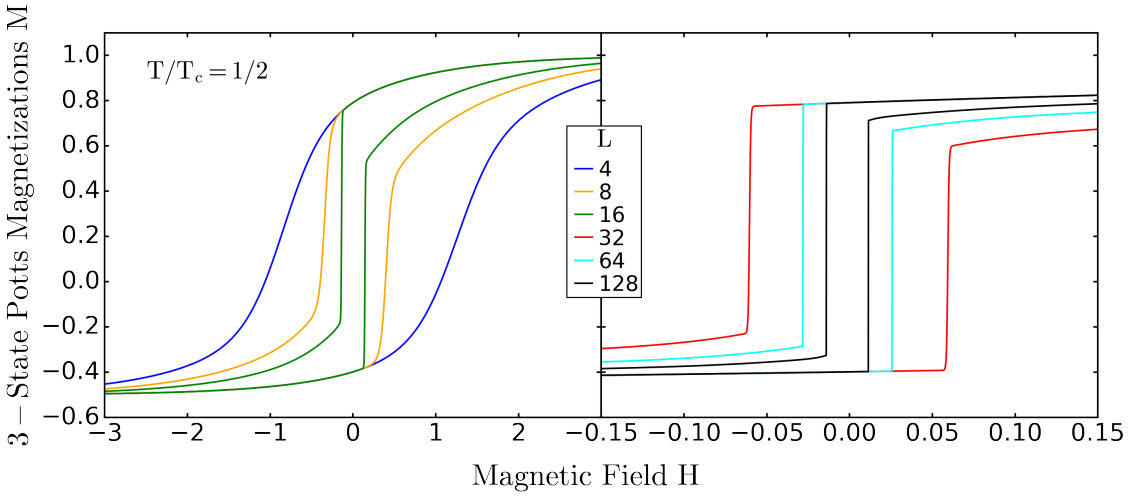


Figure 11.5: Hysteresis loops for different sizes, for $q = 3$ and temperature $T/T_C = J_C/J = 0.50$. From outer to inner, the loops are for sizes $L = 4, 8, 16$ (left) and $32, 64, 128$ (right). As the system size increases, the hysteresis loops get narrower and acquire vertical edges.

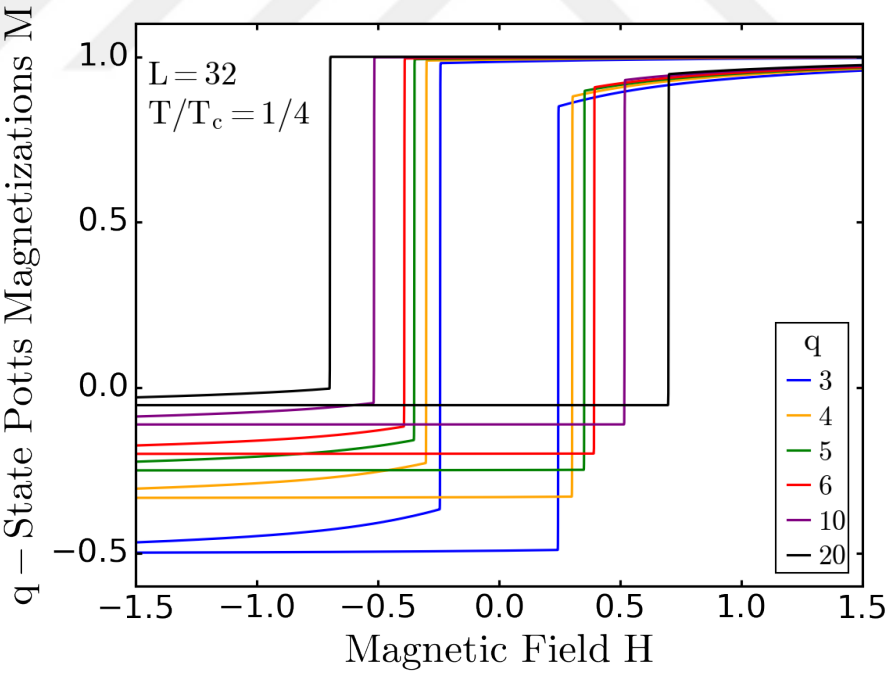


Figure 11.6: Hysteresis loops for different number of states q, for temperature $T/T_C = 0.25$ and $L = 32$. From outer to inner, the loops are for $q = 20, 10, 6, 5, 4, 3$. As the number of states decreases, the hysteresis loops get narrower and acquire curvature at the nonleading side with respect to scanning direction of each branch.

11.4.5 Asymmetry in hysteresis branches

A robust feature is the unequal curvature of the two branches. This asymmetry arises from the distinct boundary conditions used in the two scans:

- Scanning down from $H > 0$: boundary fixed in state 1 (equilibrium-favored).
- Scanning up from $H < 0$: boundary fixed in states $\neq 1$ (metastable sector).

The approach to coexistence therefore differs depending on whether the domain starts in the single-state ordered configuration or the entropically larger unfavored manifold.

11.5 Discussion: Extension to Metastable Criticality

This chapter shows that the RG methodology developed throughout this thesis extends beyond equilibrium thermodynamics. Finite-system RG with fixed boundary conditions yields information on metastable configurations that infinite-system RG flow-to-sink calculations cannot capture.

11.5.1 Potential applications

Critical phenomena and phase transitions in metastable phases have been discussed for important systems. Our approach can be adapted to:

- Surface-adsorbed systems (Butler et al., 1979; Migone et al., 1983), where metastable structures persist for experimental timescales. The Potts model is directly relevant in adsorption contexts (Berker et al., 1978; Ostlund and Berker, 1979; Kardar and Berker, 1982).
- Water (Poole et al., 1992; Gallo and Stanley, 2017), where supercooled metastable regions may host criticality (e.g., hypothesized liquid–liquid critical behavior).
- Magnetic materials, where reversed domains and hysteresis are directly described by droplet stability.

11.5.2 Comparison with equilibrium results

Extending from metastable Ising droplets (Eren and Berker, 2020) to metastable Potts droplets yields a wide range of droplet sizes across (q,H) and a rich variety of hysteresis loops versus (q,L,T). For fixed q, increasing temperature produces curvature and narrowing, starting from the nonleading side. For fixed T, increasing q produces qualitatively similar entropic effects on loop shapes. This parallels earlier observations in antiferromagnetic Potts models that increasing T and increasing q can have similar entropic consequences (Berker and Kadanoff, 1980a,b).

11.5.3 Limitations and future directions

The present treatment is static: it determines existence and stability limits, not time evolution. A temporal theory would require dynamical extensions: droplet decay pathways, relaxation times, and nucleation rates. These lie beyond equilibrium RG and motivate future dynamic RG or complementary approaches.

11.6 Conclusion

Metastable phase droplet properties can be calculated using finite-system renormalization-group theory for a variety of systems. Because metastable criticality and transitions have been discussed for important physical contexts such as surface adsorption (Butler et al., 1979; Migone et al., 1983) and water (Poole et al., 1992; Gallo and Stanley, 2017), this method provides a systematic route to quantitative predictions. Extending the approach to q-state Potts models increases the range of potential experimental applicability and reveals strong q-dependence persisting to unusually large q.

This chapter thus demonstrates that the position-space renormalization-group framework employed throughout this thesis is not confined to equilibrium phase diagrams and critical phenomena, but extends naturally to nonequilibrium properties through the adaptation of boundary conditions in the finite-system calculation. The methodological unity across equilibrium and metastable contexts reinforces the versatility of the approach.

12. CONCLUSION: SYNTHESIS AND PERSPECTIVE

12.1 Summary of Methods and Results

12.1.1 The renormalization group as unifying method

This thesis has applied renormalization-group (RG) theory to ten distinct spin systems, demonstrating the method's power as a unifying approach to phase transitions and emergent complexity. The motivating insight is that macroscopic phenomena arise from microscopic rules through the systematic elimination of short-distance degrees of freedom. The RG transformation formalizes this elimination, and the topology of the resulting flows in coupling-constant space encodes the phase structure of the system.

Two complementary RG formulations have been employed throughout:

Transfer-matrix methods (Chapters 2–8, 11): These methods express the partition function as a product of local Boltzmann weights. Under decimation, these weights compose by matrix multiplication; under bond moving, they compose by element-wise products. This approach is exact on hierarchical lattices and provides a controlled approximation for Euclidean lattices via the Migdal–Kadanoff procedure (Migdal, 1975; Kadanoff, 1976; Berker and Ostlund, 1979; Griffiths and Kaufman, 1982; Kaufman and Griffiths, 1984).

Partition-function conservation methods (Chapters 9–10): Long-range interactions require tracking renormalized couplings J'_r at multiple separation distances r. The cell-spin construction of Niemeyer and van Leeuwen defines block spins through majority rules, and recursion relations follow from requiring that the partition function remain unchanged under coarse-graining (Niemeyer and van Leeuwen, 1974; van Leeuwen, 1975; Berker and Wortis, 1976).

The hierarchical lattices studied here are not physical materials but mathematical structures on which RG is exact. Their value lies in providing unambiguous answers: there

is no approximation error to confuse interpretation. Qualitative features—existence of phases, types of transitions, presence of chaos—are robust and provide guidance for more realistic systems. Quantitative features—critical temperatures and exponent values—should not be directly compared to experiments on cubic lattices.

12.1.2 Principal results by chapter

Chapter 2: Baseline thermodynamics and reentrance. Complete thermodynamic calculations for q-state Potts and clock models established the technical apparatus—density recursion relations, symmetry reduction, and eigenvector analysis at sinks—that underpinned subsequent chapters. The discovery of interface density reentrance demonstrated that even simple systems can show non-trivial emergent behavior under RG.

Chapters 3–6: Quenched disorder and frustration. These chapters investigated spin-glass phases and their internal chaotic structure. Chapter 3 showed that Ising spin-glass chaos, characterized by Lyapunov exponent $\lambda = 1.93$, is independent of spin magnitude s from $1/2$ to ∞, with a similarly universal runaway exponent $y_R = 0.24$. Chapter 4 demonstrated that cubic-spin spin glasses with $n \geq 3$ components exhibit an emergent nematic phase. Chapter 5 showed that external magnetic fields applied to cubic-spin spin glasses yield phase proliferation (17 thermodynamic phases), including field-induced spin-glass phases with novel topologies. Chapter 6 established that fractal surfaces can sustain intrinsic surface chaos with Lyapunov exponents distinct from bulk behavior.

Chapters 7–8: Competing symmetries and algebraic order. Chapter 7 showed that merging Potts and clock interactions produces five ordered phases with rich multicritical structure; odd-q systems exhibit algebraic antiferromagnetic order due to ground-state degeneracy (Berker and Kadanoff, 1980a,b; Saleur, 1991). Chapter 8 demonstrated that the XY-Ashkin–Teller model exhibits four algebraically ordered phases characterized by fixed lines of potential surfaces (not fixed points), producing continuously varying critical exponents across entire phases (Berezinskii, 1970; Kosterlitz and Thouless, 1973; Halperin and Nelson, 1978; Nelson and Halperin, 1979).

Chapters 9–10: Interaction range as a modulator. Chapter 9 showed that power-law interactions Jr^{-a} enable ferromagnetic order in $d = 1$ for $a < 2$, destroy antiferromagnetic order through pervasive frustration, and yield spin-glass phases with piecewise chaotic interaction functions (Thouless, 1969; Ruelle, 1969; Griffiths, 1972; Aizenman and Newman, 1986; Aizenman et al., 1988). Chapter 10 demonstrated giant reentrance in the

Table 12.1: Chaos characteristics in spin-glass systems.

System	Lyapunov exponent λ	Runaway exponent y_R
Spin-s Ising ($s = 1/2$ to ∞)	1.93	0.24
Cubic-spin ($n = 1$)	0.40	0.24
Cubic-spin ($n = 3$)	0.44	0.24
Field-induced (planar-diagonal)	0.40	0.24
Sole surface ($d_S = 2.63$)	0.43	0.13
Driven surface ($d_S = 2.63$)	0.28	0.24
Bulk	0.88	0.25

Table 12.2: Phase counts across representative systems.

System	Ordered phases	Total phases
Potts/Clock baseline	1	2
Spin-s spin glass	3	4
Cubic-spin ($n \geq 3$)	4	5
Cubic-spin with field	16	17
Merged Potts–Clock	5	6
XY–Ashkin–Teller	4 (all algebraic)	5

long-range Blume–Capel model: the system passes through disorder $\rightarrow$ order $\rightarrow$ disorder as temperature decreases (Blume, 1966; Capel, 1966; Blume et al., 1971).

Chapter 11: Methodological extension to metastability. Finite-system RG with fixed boundary conditions was used to determine metastable droplet existence limits and hysteresis-loop shapes for q-state Potts models, extending equilibrium RG tools to nonequilibrium observables (Eren and Berker, 2020; Berker and Ostlund, 1979).

12.1.3 Quantitative achievements

Beyond qualitative phase identification, the thesis produced quantitative results on chaos measures (Table 12.1), phase counts (Table 12.2), and range-dependent critical behavior (Table 12.3).

Table 12.3: Notable critical-temperature behaviors and asymptotic trends.

System	Notable feature
Long-range Ising ($a \to 0.74^{+}$)	$T_c \to \infty$
Long-range Ising ($a \to 2^{-}$)	First-order transition onset
Long-range Ising ($a > 2$)	No finite-T order
Long-range Blume–Capel	Giant reentrance for $a > 0.74$
Potts ($q \to \infty$)	$T_c \sim 1/\ln q \to 0$
Clock ($q \to \infty$)	T_c saturates to XY value

12.2 Physical Interpretation of Key Findings

12.2.1 The meaning of universal chaos

The Lyapunov exponent $\lambda = 1.93$ characterizing Ising spin-glass chaos is identical for all spin magnitudes $s = 1/2, 1, 3/2, \ldots, \infty$. This universality is striking: the microscopic state space changes dramatically while the emergent chaotic behavior is quantitatively unchanged.

The Lyapunov exponent measures the rate at which nearby trajectories in coupling space diverge under repeated coarse-graining. Its universality suggests that this rate is determined less by microscopic state multiplicity than by the *geometry of frustration*—the pattern of incompatibilities among interaction constraints on the underlying graph. In the hierarchical constructions studied here, this frustration geometry is unchanged across spin magnitude, and the universality of λ reflects that topological invariance.

The runaway exponent $y_R = 0.24$ also appears broadly universal across multiple spin-glass realizations. Its smallness compared to the conventional ordered-phase value $y_R = d - 1 = 2$ indicates "unsaturated" order: the spin-glass phase does not form compact domains analogous to a ferromagnet. Microscopically, this corresponds to rough, fractal-like interfaces contributing extensive interfacial entropy, consistent with a glassy phase characterized by many competing large-scale arrangements.

12.2.2 Why nematic order requires $n \geq 3$

The emergence of nematic order in cubic-spin spin glasses for $n \geq 3$ components can be understood by symmetry and order-parameter structure.

For $n = 1$ (Ising), the only possible ordering is directional. Frustration prevents coherent directional order and yields a spin-glass phase. For $n = 2$, spins can select among two axes but there is no distinct intermediate between selecting a direction and complete disorder. For $n \geq 3$, the system can select an *axis* without selecting a *direction* along that axis: spins may predominantly lie along $\pm\hat{x}$ with random sign, yielding nematic order.

The appropriate nematic order parameter is a traceless symmetric tensor,

$$Q_{\alpha\beta} = \left\langle s_\alpha s_\beta - \frac{\delta_{\alpha\beta}}{n} \right\rangle, \tag{12.1}$$

which, for $n \geq 3$, contains sufficient independent structure to encode axis selection distinct from directional order. In the parameter window where frustration prevents directional ordering but does not preclude axis selection, nematic order becomes the stable compromise.

12.2.3 Giant reentrance as competing instabilities

The giant reentrance in the long-range Blume–Capel model (disorder $\rightarrow$ order $\rightarrow$ disorder with decreasing temperature) can be interpreted as competition between two instabilities.

At high temperature, thermal fluctuations dominate and the system is disordered. At intermediate temperature, the long-range ferromagnetic coupling establishes order (a mechanism unavailable to short-range $d = 1$ Ising systems). At low temperature, the vacancy chemical potential becomes dominant: if vacancies are favored, the system dilutes into $s = 0$ states that cannot magnetically order. The final disordered phase is thus a *dilution-driven* disorder rather than a thermal disorder.

The "giant" character reflects the fact that long-range interactions can produce robust intermediate-temperature order, which is then abruptly undermined by vacancy proliferation as temperature decreases further.

12.2.4 Fixed lines and the nature of algebraic order

The XY–Ashkin–Teller model exhibits algebraically ordered phases characterized by RG flow to fixed lines (continuous manifolds) rather than isolated fixed points. This changes

the meaning of "order" in the phase.

At a conventional ordered fixed point, the RG sink encodes a state with a finite characteristic scale in the renormalized description (and order parameters saturate). At a disordered fixed point, correlations decay exponentially. On a fixed line, the correlation length is effectively infinite throughout the phase and correlations decay as power laws. Different initial conditions flow to different points along the fixed line, yielding continuously varying critical exponents across the phase. Thus, the *entire phase is critical* in the sense of having no intrinsic length scale.

A related signature is the emergence of factorization (in Fourier-space representations) *at* the fixed line, despite the lack of factorization along the approach to it: the attractor exhibits symmetries not manifest in the transient RG flow.

12.3 Complexity and Scale: What Has Been Learned

12.3.1 Emergence through coarse-graining

Several general principles recur across the systems studied:

Coarse-graining does not always simplify. In a ferromagnet, repeated coarse-graining drives the system toward perfect alignment. In systems with competing interactions or symmetries, coarse-graining can reveal (or generate) complexity. Spin-glass phases are the clearest example: chaotic RG trajectories are emergent asymptotic structures of the transformation.

Microscopic degeneracy shapes macroscopic topology. The even-q versus odd-q distinction in merged Potts–clock systems illustrates how discrete microscopic properties (ground-state degeneracy) can control whether algebraic phases occur and how phase boundaries terminate.

Competition propagates across scales. When a Hamiltonian contains incompatible tendencies—ferromagnetic versus antiferromagnetic bonds, Potts versus clock couplings, direct versus composite ordering—the competition is not necessarily resolved at small scales but can amplify under coarse-graining, producing multiple phases and rich multicritical structure.

12.3.2 The topology of flows as organizing principle

Across the thesis, RG flow topology provides a natural classification:

- Fixed-point sinks correspond to conventional phases (ordered or disordered), with unstable fixed points controlling criticality via eigenvalues and eigenvectors.

- Fixed-line sinks correspond to algebraically ordered phases with continuously varying exponents across the phase.

- Strange attractors correspond to spin-glass phases, with Lyapunov and runaway exponents quantifying internal chaotic structure.

- Multiple attractors (of any type) correspond to multiple thermodynamic phases, with basin boundaries forming phase transitions.

This is not proposed as an exhaustive taxonomy of all RG behaviors, but as an organizing framework that naturally accommodates the ten systems studied here.

12.3.3 Limitations and open questions

Several limitations and unresolved questions frame the scope of the present work:

- Hierarchical lattices are mathematical constructs. Exact results hold on these graphs; qualitative transfer to Euclidean lattices is often reliable, but quantitative comparisons require caution.

- The treatment is classical; extending the Migdal-Kadanoff procedure to quantum systems with non-commuting operators is not straightforward, as the decimation step cannot be carried out exactly beyond the renormalization-group cell. Genuine dynamical phenomena such as aging, relaxation, and time-dependent response also lie beyond the scope of the present method.

- The generators–modulators framework is organizational. It provides language for synthesis but is not a predictive engine: new Hamiltonians still require explicit calculation.

- Some "why" questions remain open. For example, the specific numerical value $\lambda = 1.93$ plausibly encodes deep structural information about frustration on these graphs, but a direct explanatory derivation remains unknown within the present framework.

12.4 The Future of Renormalization-Group Studies

12.4.1 Methodological frontiers

Several methodological directions appear promising:

Functional renormalization group (FRG). FRG tracks flowing functions (effective potentials, vertices) rather than finitely many couplings. For the systems studied here, FRG could provide systematic improvements beyond Migdal–Kadanoff while retaining analytic structure.

Tensor network methods. Transfer-matrix formulations naturally connect to tensor network representations of partition functions. Algorithms based on MPS/PEPS/MERA provide systematic contraction and coarse-graining schemes that can extend to large state spaces, and for hierarchical lattices can yield exact contractions in broader settings.

Numerical RG at scale. Modern computational resources allow tracking larger coupling spaces and longer-range interaction sets. The multi-distance flows in Chapters 9–10 are an example; further scaling may enable higher-dimensional long-range studies and more complex local state spaces.

Conformal constraints and RG. In $d = 2$ and near criticality in higher dimensions, conformal symmetry can strongly constrain RG fixed structures. Fixed lines and algebraic phases offer a natural interface for exploring such constraints.

12.4.2 Connections to quantum many-body physics

Classical statistical mechanics has deep ties to quantum many-body physics:

- Quantum–classical mapping: d-dimensional quantum systems at $T = 0$ map to $(d+1)$-dimensional classical systems at finite temperature, connecting quantum

criticality to classical RG structure.

- Many-body localization (MBL): Disordered quantum systems can fail to thermalize and retain memory of initial conditions, offering a quantum analog to ergodicity breaking in spin glasses.

- Quantum chaos and scrambling: Growth rates of out-of-time-ordered correlators parallel Lyapunov-style diagnostics; whether the universal chaos measures found here have quantum analogs is an open direction.

- Topological phases: Topological order represents complexity beyond symmetry breaking and was not addressed in this thesis; extending the perspective to topological phases is a natural next step.

12.4.3 Complex systems beyond spin models

The perspective of complexity emerging through scale transformation applies beyond magnetic models:

- Networks and graphs: Many real networks are hierarchical; RG-like coarse-graining on graphs may reveal attractor structures analogous to those seen here.

- Biological systems: Multi-scale organization and separation of scales suggest potential RG analogs, though identifying true universality remains speculative.

- Turbulence: Cascade processes are paradigmatic scale-dependent phenomena; conceptual parallels with chaotic RG flows are suggestive.

- Economic and financial systems: Heavy tails and long-range correlations invite statistical physics methods, though universality claims remain debated.

12.4.4 Computational and machine learning approaches

The interface between RG and machine learning is rapidly developing:

- RG as feature extraction: Coarse-graining resembles representation learning by dis-

carding irrelevant microstructure while preserving macroscopic predictors.

- Neural network RG: Data-driven learning of coarse-graining maps can reproduce known flows and may discover new ones in complex coupling spaces.

- Inverse design: Combining ML and RG may enable systematic exploration of Hamiltonian space to realize target macroscopic behavior.

- Chaos characterization: ML tools for dynamical systems could offer efficient alternatives for extracting Lyapunov exponents and attractor properties from long RG trajectories.

12.5 Concluding Remarks

This thesis pursued a simple question: how does macroscopic complexity arise from microscopic simplicity? Across ten distinct model systems, the renormalization-group transformation—systematic elimination of short-distance degrees of freedom—served as the central analytic and computational instrument for answering that question in concrete settings.

The work produced specific quantitative findings: universal chaos measures, emergent phases (including nematic order), phase proliferation under fields, giant reentrance driven by dilution, fixed lines with continuously varying criticality, and nonequilibrium observables (metastable droplet limits and hysteresis loops) accessible through finite-system RG. These results demonstrate that exact RG on hierarchical lattices remains a productive route to sharp statements about phase structure and emergent complexity.

More broadly, the calculations clarify how competition amplifies under coarse-graining and how different RG attractors—fixed points, fixed lines, and strange attractors—organize distinct kinds of macroscopic behavior. Perhaps the most unexpected outcome is the universality of spin-glass chaos characteristics across dramatically different microscopic realizations. These universal numbers plausibly encode fundamental structural properties of frustration that remain to be fully understood.

The "generators and modulators" language used throughout has been an effective synthesis device, but it is not a predictive theory: it organizes known outcomes rather than producing them without calculation. A deeper theory would explain why frustration yields

the particular Lyapunov exponents observed, why symmetry competition produces the observed multicritical structures, and why scale invariance manifests as it does across discrete and continuous spin systems.

What is clear from these ten case studies is that RG flow topology provides a powerful window into emergence: which phases exist, how they connect, and what types of order are possible. The thesis has mapped ten such territories in detail. If these maps help guide future explorations—toward improved RG methods, quantum extensions, or applications beyond spin models—then the work will have served its purpose.

BIBLIOGRAPHY

Aizenman, M. and Newman, C. (1986). Discontinuity of the Percolation Density in One-Dimensional $1/[X-Y]^2$ Percolation Models. *Communications in Mathematical Physics*, 107, p. 611.

Aizenman, M. and Wehr, J. (1989). Rounding of First-Order Phase Transitions in Systems with Quenched Disorder. *Physical Review Letters*, 62, p. 2503.

Aizenman, M. and Wehr, J. (1990). Rounding of First-Order Phase Transitions in Systems with Quenched Disorder [Erratum]. *Physical Review Letters*, 64, p. 1311.

Aizenman, M., Chase, J., Chase, L. and Newman, C. (1988). Discontinuity of the Magnetization in One-Dimensional $1/|x-y|^2$ Ising and Potts Models. *Journal of Statistical Physics*, 50, p. 1.

Amoruso, C., Marinari, E., Martin, O.C. and Pagnani, A. (2003). Scalings of Domain Wall Energies in Two Dimensional Ising Spin Glasses. *Physical Review Letters*, 91, p. 087201.

Andelman, D. and Berker, A.N. (1981). q-state Potts models in d dimensions: Migdal-Kadanoff approximation. *Journal of Physics A: Mathematical and General*, 14, p. L91.

Andelman, D. and Berker, A.N. (1984). Scale-invariant quenched disorder and its stability criterion at random critical points. *Physical Review B*, 29, p. 2630.

Angelini, M.C. and Biroli, G. (2017). Real space Migdal-Kadanoff renormalisation of glassy systems: Recent results and a critical assessment. *Journal of Statistical Physics*, 167, p. 476.

Aral, N. and Berker, A.N. (2009). Chaotic spin correlations in frustrated Ising hierarchical lattices. *Physical Review B*, 79, p. 014434.

Artun, E.C. and Berker, A.N. (2020). Complete density calculations of q-state Potts and clock models: Reentrance of interface densities under symmetry breaking. *Physical Review E*, 102, p. 062135.

Artun, E.C., Keçoğlu, I., Türkoğlu, A. and Berker, A.N. (2023). Multifractal spin-glass chaos projection and interrelation of multicultural music and brain signals. *Chaos, Solitons and Fractals*, 167, p. 113005.

Artun, E.C., Sarman, D. and Berker, A.N. (2024). Nematic phase of the n-component cubic-spin spin glass in $d = 3$: Liquid-crystal phase in a dirty magnet. *Physica A*, 640, p. 129709.

Ashkin, J. and Teller, E. (1943). Statistics of two-dimensional lattices with four components. *Physical Review*, 64, p. 178.

Atalay, B. and Berker, A.N. (2018). Lower lower-critical spin-glass dimension from quenched mixed-spatial-dimensional spin glasses. *Physical Review E*, 98, p. 042125.

Baity-Jesi, M., Calore, E., Cruz, A., Fernandez, L.A., Gil-Narvion, J.M., Pemartin, I.G.-A., Gordillo-Guerrero, A., Iñiguez, D., Maiorano, A., Marinari, E., Martin-Mayor, V., Moreno-Gordo, J., Muñoz-Sudupe, A., Navarro, D., Paga, I., Parisi, G., Perez-Gaviro, S., Ricci-Tersenghi, F., Ruiz-Lorenzo, J.J., Schifano, S.F. et al. (2021). Temperature chaos is present in off-equilibrium spin-glass dynamics. *Communications Physics*, 4, p. 74.

Baxter, R.J. (1973). Potts model at the critical temperature. *Journal of Physics C: Solid State Physics*, 6, p. L445.

Bazavov, A., Berg, B.A. and Dubey, S. (2008). Phase transition properties of 3D Potts models. *Nuclear Physics B*, 802, p. 421.

Berezinskii, V.L. (1970). Destruction of long range order in one-dimensional and two-dimensional systems having a continuous symmetry group. I. Classical systems. *Zhurnal Eksperimental'noi i Teoreticheskoi Fiziki*, 59, p. 907 [*Soviet Physics JETP*, 32, p. 493 (1971)].

Berker, A.N. (1975). Critical interactions for the triangular spin-s Ising model by a spin-restructuring transformation. *Physical Review B*, 12, p. 2752.

Berker, A.N. (2010). Spin-glass attractor on tridimensional hierarchical lattices in the presence of an external magnetic field. *Physical Review E*, 81, p. 043101.

Berker, A.N. and Wortis, M. (1976). Blume-Emery-Griffiths-Potts model in two dimensions: Phase diagram and critical properties from a position-space renormalization group. *Physical Review B*, 14, p. 4946.

Berker, A.N. and Nelson, D.R. (1979). Superfluidity and phase separation in helium films. *Physical Review B*, 19, pp. 2488–2503.

Berker, A.N., Ostlund, S. and Putnam, F.A. (1978). Renormalization-group treatment of a Potts lattice gas for krypton adsorbed onto graphite. *Physical Review B*, 17, p. 3650.

Berker, A.N. and Ostlund, S. (1979). Renormalisation-group calculations of finite systems: Order parameter and specific heat for epitaxial ordering. *Journal of Physics C: Solid State Physics*, 12, p. 4961.

Berker, A.N. and Kadanoff, L.P. (1980). Ground-state entropy and algebraic order at low temperatures. *Journal of Physics A: Mathematical and General*, 13, p. L259.

Berker, A.N. and Kadanoff, L.P. (1980). Corrigendum. *Journal of Physics A: Mathematical and General*, 13, p. 3786.

Berker, A.N. and Andelman, D. (1982). First order and second order phase transitions in Potts models: Competing mechanisms. *Journal of Applied Physics*, 53, p. 7923.

Berker, A.N. and McKay, S.R. (1984). Hierarchical models and chaotic spin glasses. *Journal of Statistical Physics*, 36, p. 787.

Berker, A.N., Ostlund, S. and Putnam, F.A. (1978). Renormalization-group treatment of a Potts lattice gas for krypton adsorbed onto graphite. *Physical Review B*, 17, pp. 3650–3665.

Billoire, A., Fernandez, L.A., Maiorano, A., Marinari, E., Martin-Mayor, V., Moreno-Gordo, J., Parisi, G., Ricci-Tersenghi, F. and Ruiz-Lorenzo, J.J. (2018). Dynamic variational study of chaos: Spin glasses in three dimensions. *Journal of Statistical Mechanics: Theory and Experiment*, (2018) 033302.

Blume, M. (1966). Theory of the First-Order Magnetic Phase Change in UO_2. *Physical Review*, 141, p. 517.

Blume, M., Emery, V.J. and Griffiths, R.B. (1971). Ising Model for the λ Transition and Phase Separation in He^3-He^4 Mixtures. *Physical Review A*, 4, p. 1071.

Boettcher, S. (2005). Stiffness of the Edwards-Anderson Model in All Dimensions. *Physical Review Letters*, 95, p. 197205.

Boettcher, S. and Li, S. (2018). Analysis of coined quantum walks with renormalization. *Physical Review A*, 97, p. 012309.

Bouchaud, J.-P., Krzakala, F. and Martin, O.C. (2003). Energy exponents and corrections to scaling in Ising spin glasses. *Physical Review B*, 68, p. 224404.

Butera, P. and Comi, M. (2002). Critical universality and hyperscaling revisited for Ising models of general spin using extended high-temperature series. *Physical Review B*, 65, p. 144431.

Butera, P. and Comi, M. (2002). An on-line library of extended high-temperature expansions of basic observables for the spin-*S* Ising models on two- and three-dimensional lattices. *Journal of Statistical Physics*, 109, p. 311.

Butera, P. and Comi, M. (2004). Updated tests of scaling and universality for spin-spin correlations in the two- and three-dimensional spin-*S* Ising models using high-temperature expansions. *Physical Review B*, 69, p. 174416.

Butera, P., Comi, M. and Guttmann, A.J. (2003). Critical parameters and universal am-

plitude ratios of two-dimensional spin-S Ising models using high- and low-temperature expansions. *Physical Review B*, 67, p. 054402.

Butler, D.M., Litzinger, J.A., Stewart, G.A. and Griffiths, R.B. (1979). Heat Capacity of Krypton Physisorbed on Graphite. *Physical Review Letters*, 42, p. 1289.

Caflisch, R.G., Berker, A.N. and Kardar, M. (1985). Reentrant melting of krypton adsorbed on graphite and the helical Potts-lattice-gas model. *Physical Review B*, 31, pp. 4527–4537.

Camp, W.J. and Vandyke, J.P. (1975). High-temperature series for susceptibility of spin-s Ising model: Analysis of confluent singularities. *Physical Review B*, 11, p. 2579.

Camp, W.J., Saul, D.M., Vandyke, J.P. and Wortis, M. (1976). Series analysis of corrections to scaling for spin-pair correlations of spin-s Ising model: Confluent singularities, universality, and hyperscaling. *Physical Review B*, 14, p. 3990.

Capel, H.W. (1966). On the Possibility of First-order Phase Transitions in Ising Systems of Triplet Ions with Zero-Field Splitting. *Physica*, 32, p. 966.

Chen, X., Carrete, J., Sullivan, S., van Roekeghem, A., Li, Z., Li, X., Zhou, J., Mingo, N. and Shi, L. (2019). Coupling of spinons with defects and phonons in the spin chain compound CaCuO. *Physical Review Letters*, 122, p. 185901.

Çağlar, T. and Berker, A.N. (2016). Chiral Potts Spin Glass in $d = 2$ and 3 Dimensions. *Physical Review E*, 94, p. 032121.

Çağlar, T. and Berker, A.N. (2017). Devil's staircase continuum in the chiral clock spin glass with competing ferromagnetic-antiferromagnetic and left-right chiral interactions. *Physical Review E*, 95, p. 042125.

Çağlar, T. and Berker, A.N. (2017). Phase transitions between different spin-glass phases and between different chaoses in quenched random chiral systems. *Physical Review E*, 96, p. 032103.

Chang, S.-C., Roeder, R.K.W. and Shrock, R. (2020). q-Plane zeros of the Potts partition function on diamond hierarchical graphs. *Journal of Mathematical Physics*, 61, p. 073301.

Chio, I. and Roeder, R.K.W. (2021). Chromatic zeros on hierarchical lattices and equidistribution on parameter space. *Annales de l'Institut Henri Poincaré D*, 8, p. 491.

Cladis, P.E. (1975). New Liquid-Crystal Phase Diagram. *Physical Review Letters*, 35, pp. 48–51.

Clark, J. and Lochridge, C. (2023). Weak-disorder limit for directed polymers on critical hierarchical graphs with vertex disorder. *Stochastic Processes and their Applications*, 158, p. 75.

Collet, P. and Eckmann, J.-P. (1980). *Iterated Maps on the Interval as Dynamical Systems*. Boston: Birkhäuser.

Debenedetti, P.G. (1996). *Metastable Liquids: Concepts and Principles*. Princeton: Princeton University Press.

Defenu, N., Donner, T., Macrì, T., Pagano, G., Ruffo, S. and Trombettoni, A. (2023). Long-range interacting quantum systems. *Reviews of Modern Physics*, 95, p. 035002.

Dehghani, A., Hendi, S.H. and Mann, R.B. (2020). Range of novel black hole phase transitions via massive gravity: Triple points and N-fold reentrant phase transitions. *Physical Review D*, 101, p. 084026.

Demirtaş, M., Tuncer, A. and Berker, A.N. (2015). Lower-critical spin-glass dimension from 23 sequenced hierarchical models. *Physical Review E*, 92, p. 022136.

Derevyagin, M., Dunne, G.V., Mograby, G. and Teplyaev, A. (2020). Perfect quantum state transfer on diamond fractal graphs. *Quantum Information Processing*, 19, p. 328.

Devre, H.Y. and Berker, A.N. (2022). First-order to second-order phase transition changeover and latent heats of q-state Potts models in $d = 2,3$ from a simple Migdal-Kadanoff adaptation. *Physical Review E*, 105, p. 054124.

Ditzian, R.V., Banavar, J.R., Grest, G.S. and Kadanoff, L.P. (1980). Phase diagram for the Ashkin-Teller model in three dimensions. *Physical Review B*, 22, p. 2542.

Domb, C. and Sykes, M.F. (1962). Effect of change of spin on the critical properties of the Ising and Heisenberg models. *Physical Review*, 128, p. 168.

Domb, C. and Green, M.S. (eds.) (1974). *Phase Transitions and Critical Phenomena: Series Expansions for Lattice Models*, Vol. 3. London and New York: Academic Press.

Dyson, F. J. (1969). Existence of a phase-transition in a one-dimensional Ising ferromagnet. *Communications in Mathematical Physics*, 12, p. 91.

Edwards, S.F. and Anderson, P.W. (1975). Theory of spin glasses. *Journal of Physics F: Metal Physics*, 5, p. 965.

Eldan, R. (2020). The Sherrington-Kirkpatrick spin glass exhibits chaos. *Journal of Statistical Physics*, 181, p. 1266.

Erbaş, A., Tuncer, A., Yücesoy, B. and Berker, A.N. (2005). Phase diagrams and crossover in spatially anisotropic $d = 3$ Ising, XY magnetic, and percolation systems: Exact renormalization-group solutions of hierarchical models. *Physical Review E*, 72, p. 026129.

Eren, E. and Berker, A.N. (2020). Metastable reverse-phase droplets within ordered phases: Renormalization-group calculation of field and temperature dependence of limiting size. *Physical Review E*, 101, p. 042127.

Falicov, A. and Berker, A.N. (1995). Finite-temperature phase diagram of the *t-J* model: Renormalization-group theory. *Physical Review B*, 51, p. 12458.

Fernandez, L.A., Marinari, E., Martin-Mayor, V., Parisi, G. and Yllanes, D. (2016). Temperature chaos is a non-local effect. *Journal of Statistical Mechanics: Theory and Experiment*, (2016) 123301.

Fisher, M.E. and Berker, A.N. (1982). Scaling for First-Order Phase Transitions in Thermodynamic and Finite Systems. *Physical Review B*, 26, p. 2507.

Flory, P.J. (1986). *Principles of Polymer Chemistry*. Ithaca, NY: Cornell University Press.

Franz, S., Parisi, G. and Virasoro, M.A. (1994). Interfaces and lower critical dimension in a spin-glass model. *Journal de Physique I*, 4, p. 1657.

Frassino, A.M., Kubižňák, D., Mann, R.B. and Simovic, F. (2014). Multiple reentrant phase transitions and triple points in Lovelock thermodynamics. *Journal of High Energy Physics*, 2014, p. 80.

Gallo, P. and Stanley, H.E. (2017). Supercooled water reveals its secrets. *Science*, 358, p. 1543.

Griffiths, R.B. (1972). Rigorous Results and Theorems. In: Domb, C. and Green, M.S. (eds.) *Phase Transitions and Critical Phenomena*, Vol. 1. New York: Academic.

Griffiths, R.B. and Kaufman, M. (1982). Spin systems on hierarchical lattices. Introduction and thermodynamic limit. *Physical Review B*, 26, pp. 5022–5032.

Grinstein, G., Berker, A.N., Chalupa, J. and Wortis, M. (1976). Exact Renormalization Group with Griffiths Singularities and Spin-Glass Behavior: The Random Ising Chain. *Physical Review Letters*, 36, p. 1508.

Güven, C., Berker, A.N., Hinczewski, M. and Nishimori, H. (2008). Reentrant and forward phase diagrams of the anisotropic three-dimensional Ising spin glass. *Physical Review E*, 77, p. 061110.

Halperin, B.I. and Nelson, D.R. (1978). Theory of two-dimensional melting. *Physical Review Letters*, 41, p. 121.

Hartford, E.J. and McKay, S.R. (1991). Ising spin-glass critical and multicritical fixed distributions from a renormalization-group calculation with quenched randomness. *Journal of Applied Physics*, 70, p. 6068.

Hilborn, R.C. (2003). *Chaos and Nonlinear Dynamics*. 2nd ed. New York: Oxford University Press.

Hinczewski, M. and Berker, A.N. (2005). Multicritical Point Relations in Three Dual Pairs of Hierarchical-Lattice Ising Spin-Glasses. *Physical Review B*, 72, p. 144402.

Hinczewski, M. and Berker, A.N. (2006). $d = 3$ anisotropic and $d = 2$ tJ models: phase diagrams, thermodynamic properties, and chemical potential shift. *The European Physical Journal B*, 51, p. 461.

Hinczewski, M. and Berker, A.N. (2008). Finite-temperature phase diagram of nonmagnetic impurities in high-temperature superconductors using a $d = 3$ t-J model with quenched disorder. *Physical Review B*, 78, p. 064507.

Hoston, W. and Berker, A.N. (1991). Multicritical Phase Diagrams of the Blume-Emery-Griffiths Model with Repulsive Biquadratic Coupling. *Physical Review Letters*, 67, p. 1027.

Hui, K. and Berker, A.N. (1989). Random-Field Mechanism in Random-Bond Multicritical Systems. *Physical Review Letters*, 62, p. 2507.

Hui, K. and Berker, A.N. (1989). Random-Field Mechanism in Random-Bond Multicritical Systems. *Physical Review Letters*, 63, p. 2433(E).

Ilker, E. and Berker, A.N. (2013). High q-state clock spin glasses in three dimensions and the Lyapunov exponents of chaotic phases and chaotic phase boundaries. *Physical Review E*, 87, p. 032124.

Ilker, E. and Berker, A.N. (2014). Overfrustrated and underfrustrated spin glasses in $d = 3$ and 2: Evolution of phase diagrams and chaos including spin-glass order in $d = 2$. *Physical Review E*, 89, p. 042139.

Ilker, E. and Berker, A.N. (2014). Odd q-state clock spin-glass models in three dimensions, asymmetric phase diagrams, and multiple algebraically ordered phases. *Physical Review E*, 90, p. 062112.

Indekeu, J.O., Berker, A.N., Chiang, C. and Garland, C.W. (1987). Reentrant transition enthalpies of liquid crystals: The frustrated spin-gas model and experiments. *Physical Review A*, 35, pp. 1371–1375.

Jensen, I., Guttmann, A.J. and Enting, I.G. (1996). Low-temperature series expansions for the square lattice Ising model with spin $S > 1$. *Journal of Physics A: Mathematical and General*, 29, p. 3805.

Jiang, K., Qiao, J. and Lan, Y. (2021). Chaotic renormalization flow in the Potts model induced by long-range competition. *Physical Review E*, 103, p. 062117.

José, J.V., Kadanoff, L.P., Kirkpatrick, S. and Nelson, D.R. (1977). Renormalization, vortices, and symmetry-breaking perturbations in two-dimensional planar model. *Physical Review B*, 16, p. 1217.

Kadanoff, L.P. (1966). Scaling laws for Ising models near T_c. *Physics*, 2, pp. 263–272.

Kadanoff, L.P. (1976). Notes on Migdal's recursion formulas. *Annals of Physics*, 100,

pp. 359–394.

Kaplan, C.N. and Berker, A.N. (2008). Quantum-Mechanically Induced Asymmetry in the Phase Diagrams of Spin-Glass Systems. *Physical Review Letters*, 100, p. 027204.

Kardar, M. and Berker, A.N. (1982). Commensurate-Incommensurate Phase Diagrams for Overlayers from a Helical Potts Model. *Physical Review Letters*, 48, p. 1552.

Kashchiev, D. (2000). *Nucleation: Basic Theory with Applications*. Oxford: Butterworth-Heinemann.

Kaufman, M. (2018). Entropy Driven Phase Transition in Polymer Gels: Mean Field Theory. *Entropy*, 20, p. 501.

Kaufman, M., Berger, T., Gujrati, P.D. and Bowman, D. (1990). Polymerization on the diamond hierarchical lattice: The Migdal-Kadanoff renormalization-group scheme. *Physical Review A*, 41, pp. 4371-–4378.

Kaufman, M. and Griffiths, R.B. (1984). Spin systems on hierarchical lattices. II. Some examples of soluble models. *Physical Review B*, 30, pp. 244–249.

Keçoğlu, I. and Berker, A.N. (2023). Global Ashkin–Teller Phase Diagrams in Two and Three Dimensions: Multicritical Bifurcation versus Double Tricriticality-Endpoint. *Physica A*, 630, p. 129248.

Kosterlitz, J.M. and Thouless, D.J. (1973). Ordering, metastability and phase transitions in two-dimensional systems. *Journal of Physics C: Solid State Physics*, 6, p. 1181.

Kotorowicz, M. and Kozitsky, Y. (2022). Phase transitions in the Ising model on a hierarchical random graph based on the triangle. *Journal of Physics A: Mathematical and Theoretical*, 55, p. 405002.

Kraichnan, R.H. (1961). Dynamics of Nonlinear Stochastic Systems. *Journal of Mathematical Physics*, 2, pp. 124–148.

Lloyd, P. and Oglesby, J. (1976). Analytic approximations for disordered systems. *Journal of Physics C: Solid State Physics*, 9, p. 4383.

Ma, F., Su, J., Hao, Y., Yao, B. and Yan, G. (2018). A class of vertex–edge-growth small-world network models having scale-free, self-similar and hierarchical characters. *Physica A: Statistical Mechanics and its Applications*, 492, pp. 1194–1205.

Maiorano, A. and Parisi, G. (2018). Support for the value 5/2 for the spin glass lower critical dimension at zero magnetic field. *Proceedings of the National Academy of Sciences USA*, 115, p. 5129.

Mattis, D.C. (1976). Solvable spin systems with random interactions. *Physics Letters A*, 56, p. 421.

McKay, S.R. and Berker, A.N. (1984). Chaotic spin glasses: An upper critical dimension. *Journal of Applied Physics*, 55, p. 1646.

McKay, S.R., Berker, A.N. and Kirkpatrick, S. (1982). Spin-Glass Behavior in Frustrated Ising Models with Chaotic Renormalization-Group Trajectories. *Physical Review Letters*, 48, p. 767.

McKay, S.R., Berker, A.N. and Kirkpatrick, S. (1982). Amorphously packed, frustrated hierarchical models: Chaotic rescaling and spin-glass behavior. *Journal of Applied Physics*, 53, p. 7974.

Migdal, A.A. (1975). Phase transitions in gauge and spin lattice systems. *Zhurnal Eksperimental'noi i Teoreticheskoi Fiziki*, 69, p. 1457 [*Soviet Physics JETP*, 42, p. 743 (1976)].

Migone, A.D., Chan, M.H.W., Niskanen, N.J. and Griffiths, R.B. (1983). Incipient triple point for N_2 adsorbed on graphite. *Journal of Physics C*, 16, p. 1115.

Monthus, C. (2020). Real-space renormalization for disordered systems at the level of large deviations. *Journal of Statistical Mechanics: Theory and Experiment*, 2020, p. 013301.

Morgenstern, I. and Binder, K. (1979). Evidence Against Spin-Glass Order in the Two-Dimensional Random-Bond Ising Model. *Physical Review Letters*, 43, p. 1615.

Myshlyavtsev, A.V., Myshlyavtseva, M.D. and Akimenko, S.S. (2020). Classical lattice models with single-node interactions on hierarchical lattices: The two-layer Ising model. *Physica A*, 558, p. 124919.

Nelson, D.R. and Halperin, B.I. (1979). Dislocation-mediated melting in two dimensions. *Physical Review B*, 19, p. 2457.

Nelson, D.R., Kosterlitz, J.M. and Fisher, E. (1974). Renormalization-Group Analysis of Bicritical and Tetracritical Points. *Physical Review Letters*, 33, p. 813.

Netz, R.R. and Berker, A.N. (1992). Smectic-C order, in-plane domains, and nematic reentrance in a microscopic model of liquid crystals. *Physical Review Letters*, 68, pp. 333–336.

Niemeyer, T. and van Leeuwen, J.M.J. (1974). *Physica (Utrecht)*, 71, p. 17.

Nienhuis, B., Berker, A.N., Riedel, E.K. and Schick, M. (1979). First- and Second-Order Phase Transitions in Potts Models: Renormalization-Group Solution. *Physical Review Letters*, 43, pp. 737–740.

Onsager, L. (1944). Crystal statistics. I. A two-dimensional model with an order-disorder transition. *Physical Review*, 65, p. 117.

Ostlund, S. and Berker, A.N. (1979). Multicritical Phase Diagram of Gases Adsorbed on Graphite: Temperature Variation and Finite Size Effects. *Physical Review Letters*, 42,

p. 843.

Pektaş, Y.E., Artun, E.C. and Berker, A.N. (2023). Driven and non-driven surface chaos in spin-glass sponges. *Chaos, Solitons and Fractals*, 176, p. 114159.

Polackova, M. and Gendiar, A. (2023). Anisotropic deformation of the 6-state clock model: Tricritical-point classification. *Physica A*, 624, p. 128907.

Poole, P.H., Sciortino, F., Essmann, U. and Stanley, H.E. (1992). Phase behaviour of metastable water. *Nature (London)*, 360, p. 324.

Rocha-Neto, M.J.G., Camelo-Neto, G., Nogueira Jr., E. and Coutinho, S. (2018). The Blume–Capel model on hierarchical lattices: Exact local properties. *Physica A: Statistical Mechanics and its Applications*, 494, pp. 559–573.

Rojas, O., de Souza, S.M. and Moura-Melo, W.A. (2007). On the series expansion of the general spin-*S* Ising chain. *Physica A*, 373, p. 324.

Ruelle, D. (1969). *Statistical Mechanics Rigorous Results*. New York: Benjamin.

Ruiz, P. A. (2018). Explicit Formulas for Heat Kernels on Diamond Fractals *Communications in Mathematical Physics*, 364, pp. 1305-1326.

Seul, M. and Andelman, D. (1995). Domain shapes and patterns: The phenomenology of modulated phases. *Science*, 267, pp. 476–483.

Sethna, J.P., Dahmen, K.A. and Myers, C.R. (2001). Crackling noise. *Nature*, 410, pp. 242–250.

Saleur, H. (1991). The antiferromagnetic Potts model in two dimensions: Berker-Kadanoff phase, antiferromagnetic transition, and the role of Beraha numbers. *Nuclear Physics B*, 360, p. 219.

Sardar, S. and Chakraborty, K.G. (1997). Analysis of coherent anomalies, scaling exponent and confluent singularities for spin-*S* Ising model on cubic nets. *Physica A*, 238, p. 317.

Sarıyer, O.S. (2019). Two-dimensional quantum-spin-1/2 XXZ magnet in zero magnetic field: Global thermodynamics from renormalisation group theory. *Philosophical Magazine*, 99, pp. 1787–1824.

Sarmento, E.F. and Kaneyoshi, T. (1989). Phase transition of transverse Ising model in a random field. *Physical Review B*, 39, p. 9555.

Schick, M. and Shih, W.-H. (1986). Spin-1 model of a microemulsion. *Physical Review B*, 34, pp. 1797–1801.

Sivardière, J., Berker, A.N. and Wortis, M. (1973). Uniaxial and biaxial ordering in magnetic crystals: Molecular-field theory. *Physical Review B*, 7, p. 343.

Talapov, A.L. and Blöte, H.W.J. (1996). The magnetization of the 3D Ising model. *Journal of Physics A: Mathematical and General*, 29, p. 5727.

Thouless, D.J. (1969). Long-Range Order in One-Dimensional Ising Systems. *Physical Review*, 187, p. 732.

Toulouse, G. (1977). Theory of Frustration Effect in Spin Glasses: I. *Communications on Physics*, 2, p. 115.

Tunca, E. and Berker, A.N. (2023). Nematic ordering in the Heisenberg spin-glass system in $d = 3$ dimensions. *Physical Review E*, 107, p. 014116.

van Leeuwen, J.M.J. (1975). Singularities in the Critical Surface and Universality for Ising-Like Spin Systems. *Physical Review Letters*, 34, p. 1056.

Vandyke, J.P. and Camp, W.J. (1974). High-temperature series for susceptibility of spin-S Ising model. *Physical Review B*, 9, p. 3121.

Vause, C.A. and Walker, J.S. (1982). Effects of orientational degrees of freedom in closed-loop solubility phase diagrams. *Physics Letters A*, 90, pp. 419–424.

Wang, W., Machta, J. and Katzgraber, H.G. (2016). Bond chaos in spin glasses revealed through thermal boundary conditions. *Physical Review B*, 93, p. 224414.

Wang, W., Wallin, M. and Lidmar, J. (2018). Chaotic temperature and bond dependence of four-dimensional Gaussian spin glasses with partial thermal boundary conditions. *Physical Review E*, 98, p. 062122.

Wilson, K.G. (1971). Renormalization group and critical phenomena. I. Renormalization group and the Kadanoff scaling picture. *Physical Review B*, 4, p. 3174.

Wilson, K.G. (1971). Renormalization group and critical phenomena. II. Phase-space cell analysis of critical behavior. *Physical Review B*, 4, p. 3184.

Wu, F.Y. (1982). The Potts Model. *Reviews of Modern Physics*, 54, p. 235.

Yokota, T. (2002). On the ground state of Ising models with arbitrary spin quantum number. *Physics Letters A*, 298, p. 236.

Yüksel, Y., Akıncı, Ü. and Vatansever, E. (2022). Metamagnetic anomalies in the kinetic Blume–Capel model with arbitrary spin. *Physica A: Statistical Mechanics and its Applications*, 603, p. 127760.

Zeynioğlu, D.I. and Berker, A.N. (2025). 6-Point Tripled Ashkin-Teller Global Phase Diagrams in Two and Three Dimensions. *Physica A*, 680, p. 131049.

Zhang, P.-P., Gao, Z.-Y., Xu, Y.-L., Wang, C.-Y. and Kong, X.-M. (2022). Phase diagrams, quantum correlations and critical phenomena of antiferromagnetic Heisenberg model on diamond-type hierarchical lattices. *Quantum Science and Technology*, 7, p. 025024.

Zhu, Z., Ochoa, A.J., Schnabel, S., Hamze, F. and Katzgraber, H.G. (2016). Best-case performance of quantum annealers on native spin-glass benchmarks: How chaos can affect success probabilities. *Physical Review A*, 93, p. 012317.

CURRICULUM VITAE

Personal Information

Name and Surname: Güneş Erbil Can Artun

Academic Background

Bachelor's Degree

University: Yeditepe University
Department: Physics Department
Graduation Year: 2011

Master's Degree

University: Yeditepe University
Program: Physics
Graduation Year: 2015

University: Yeditepe University
Program: Philosophy
Graduation Year: 2018

Doctoral Degree

University: Kadir Has University
Program: Computational Sciences and Engineering
Graduation Year: 2026

Work Experience

2025–Present	Researcher	TÜBİTAK National Metrology Institute
2022–2026	Researcher	TÜBİTAK Research Institute for Fundamental Sciences
2016–2017	Specialist	Yeditepe University Calibration Laboratory
2010–2010	Visiting Research Fellow	Harvard University

Publications

Hacınlıyan, A., Skarlatos, Y., Şahin, G., Avcı, İ., Öztürk, T. and Artun, E.C. (2013). Signals of chaos in the transient current through As_2S_3(Ag) and As_2Se_3(Al) thin films. *Chaotic Modeling and Simulation*, 4, pp. 591–599.

Açıkalın, Ş.N. and Artun, E.C. (2019). The concept of self-organized criticality: The case study of the Arab uprising. In: *Chaos, Complexity and Leadership 2017*. Springer, pp. 73–85.

Artun, E.C. and Berker, A.N. (2020). Complete density calculations of q-state Potts and clock models: Reentrance of interface densities under symmetry breaking. *Physical Review E*, 102, p. 062135.

Artun, E.C. and Berker, A.N. (2021). Metastable Potts droplets. *Physical Review E*, 103, p. 032102.

Artun, E.C. and Berker, A.N. (2021). Spin-s spin-glass phases in the $d = 3$ Ising model. *Physical Review E*, 104, p. 044131.

Artun, E.C., Keçoğlu, I., Türkoğlu, A. and Berker, A.N. (2023). Multifractal spin-glass chaos projection and interrelation of multicultural music and brain signals. *Chaos, Solitons and Fractals*, 167, p. 113005.

Artun, E.C. and Berker, A.N. (2023). Merged Potts-clock model: Algebraic and conventional multistructured multicritical orderings in two and three dimensions. *Physical*

Review E, 108, p. 024116.

Pektaş, Y.E., Artun, E.C. and Berker, A.N. (2023). Driven and non-driven surface chaos in spin-glass sponges. *Chaos, Solitons and Fractals*, 176, p. 114159.

Artun, E.C., Sarman, D. and Berker, A.N. (2024). Nematic phase of the n-component cubic-spin spin glass in $d = 3$: Liquid-crystal phase in a dirty magnet. *Physica A*, 640, p. 129709.

Artun, E.C., Sarman, D. and Berker, A.N. (2024). Axial, planar-diagonal, body-diagonal fields on the cubic-spin spin glass in $d = 3$: A plethora of ordered phases under finite fields. *Physical Review E*, 110, p. 034123.

Artun, E.C. and Berker, A.N. (2025). Multiplicity of algebraic order from fixed lines of potential surfaces: XY-Ashkin-Teller in spatial dimension $d = 2$. *Physical Review E*, 112, p. 024126.

Artun, E.C. and Berker, A.N. (2026). Blume-Capel model in $d = 1$ with long-range interactions: Giant reentrance in the finite-temperature tricritical phase diagrams. *Physica A*, 688, p. 131387.

Artun, E.C. and Berker, A.N. (2025). Ferromagnetic and spin-glass finite-temperature order but no antiferromagnetic order in the $d = 1$ Ising model with long-range power-law interactions. [In review]

Publications and Presentations Derived from the Thesis

Journal Articles

Artun, E.C. and Berker, A.N. (2020). Complete density calculations of q-state Potts and clock models: Reentrance of interface densities under symmetry breaking. *Physical Review E*, 102, p. 062135.

Artun, E.C. and Berker, A.N. (2021). Metastable Potts droplets. *Physical Review E*, 103, p. 032102.

Artun, E.C. and Berker, A.N. (2021). Spin-s spin-glass phases in the $d = 3$ Ising model. *Physical Review E*, 104, p. 044131.

Artun, E.C. and Berker, A.N. (2023). Merged Potts-clock model: Algebraic and conventional multistructured multicritical orderings in two and three dimensions. *Physical Review E*, 108, p. 024116.

Pektaş, Y.E., Artun, E.C. and Berker, A.N. (2023). Driven and non-driven surface chaos in spin-glass sponges. *Chaos, Solitons and Fractals*, 176, p. 114159.

Artun, E.C., Sarman, D. and Berker, A.N. (2024). Nematic phase of the n-component cubic-spin spin glass in $d = 3$: Liquid-crystal phase in a dirty magnet. *Physica A*, 640, p. 129709.

Artun, E.C., Sarman, D. and Berker, A.N. (2024). Axial, planar-diagonal, body-diagonal fields on the cubic-spin spin glass in $d = 3$: A plethora of ordered phases under finite fields. *Physical Review E*, 110, p. 034123.

Artun, E.C. and Berker, A.N. (2025). Multiplicity of algebraic order from fixed lines of potential surfaces: XY-Ashkin-Teller in spatial dimension $d = 2$. *Physical Review E*, 112, p. 024126.

Artun, E.C. and Berker, A.N. (2026). Blume-Capel model in $d = 1$ with long-range interactions: Giant reentrance in the finite-temperature tricritical phase diagrams. *Physica A*, 688, p. 131387.

Artun, E.C. and Berker, A.N. (2026). Ferromagnetic and spin-glass finite-temperature order but no antiferromagnetic order in the $d = 1$ Ising model with long-range power-law interactions. [In review]

Conference Presentations

Artun, E.C. (2023). Liquid crystal phase in spin glasses. *28th Condensed Matter Physics Meeting*, Bilkent University, Ankara, Türkiye.

Tunca, E., Artun, E.C., Sarman, D., Türkoğlu, A. and Berker, A.N. (2023). Soap inside the dirty magnet: Nematic phase of the $d = 3$ spin glass of Heisenberg spins and

cubic spins. *26th National Liquid Phase Symposium*, Piri Reis University, İstanbul, Türkiye.

Artun, E.C., Pektaş, Y.E. and Berker, A.N. (2024). Spin-glass sponges: Spin glasses with fractal surfaces. *11th International Scientific Conference on Physics and Control*, Kadir Has University, İstanbul, Türkiye.

Artun, E.C., Sarman, D. and Berker, A.N. (2024). Spin-glass phase transition in finite field. *40th International Physics Congress of the Turkish Physical Society*, Muğla, Türkiye.